Numerical Simulation of Wave Energy Dissipation in Turbulent Boundary Layers

by
Stephanie Moneris

A Thesis Submitted to the Faculty of

The College of Engineering

in Partial Fulfillment of the Requirements for the Degree of

Master of Science

Florida Atlantic University

Boca Raton, Florida

August, 2000

ugewqol

Numerical Simulation of Wave Energy Dissipation in Turbulent Boundary Layers

by
Stephanie Moneris

This thesis was prepared under the direction of the candidate's thesis advisor, Dr. Slinn, Department of Ocean Engineering, and has been approved by the members of her supervisory committee. It was submitted to the faculty of The College of Engineering and was accepted in partial fulfillment of the requirements for the degree of Master of Science.

SUPERVISORY COMMITTEE:

Thesis Advisor

Chairman, Department of Ocean Engineering

Dean, College of Engineering

Vice Provost

Date

Acknowledgments

I wish to thank Dr. D. Slinn, my advisor, for his friendliness, his assistance and patience in the realization of this work and preparation of this thesis. I would also like to thank the members of my commitee, Dr. P. Ananthakrishnan and Dr. D. Dhanak for their advice.

Sincères remerciements à l'Ecole des Mines d'Alès, ainsi qu'à ma famille et amis, de France et des Etats-Unis, pour m'avoir soutenu tout au long de mes études.

Abstract

Author: Stephanie Moneris

Title: Numerical simulation of wave energy dissipation in turbulent boundary layers

Institution: Florida Atlantic University

Thesis Advisor: Dr. D. Slinn

Degree: Master of Science

Year: 2000

Shoaling surface waves create turbulent shear flows at the sea-bed and thereby contribute to wave energy dissipation in the bottom boundary layer. Turbulent boundary layers are examined using a high-resolution time-dependent three-dimensional numerical model. Simulations estimate the wave energy dissipation in the boundary layer. Results indicate that turbulence levels are coupled to the wave cycle; accelerating flow organizes the boundary layer structure, decelerating flow destabilizes it and flow reversal induces the strongest turbulent bursts. Details of the flow are functions of the Reynolds number, wave frequency, wave complexity, presence of a mean current, and the flow history of the preceding wave period. Mean flow properties are compared between the three-dimensional model and one-dimensional eddy-viscosity based models. Generally, features of the boundary layer are satisfactorily approximated by the eddy-viscosity models, with accuracy depending on the wave amplitude, period, phase, and other forcing conditions.

Table of Contents

List of Figures

List of Tables

Chapter 1

Introduction

Many aspects of the flow of air or water in the vicinity of boundaries have been studied theoretically and experimentally during the 20^{th} century. In the beginning of the century, Prandtl [1] showed that the flow about a solid body can be divided into two regions, a very thin layer in the neighborhood of the body, called the boundary layer, where friction plays an essential part, and the exterior region outside this layer, where friction may be neglected. This concept made it possible to clarify many complex phenomena which occur in flows.

At first, the boundary layer theory was mainly developed for the case of laminar flow, but was later extended to include turbulent boundary layers, which are more common in practical applications. The problem of laminar flow has been solved for many cases. Turbulent boundary layers, however, are not well understood because of their extreme complexity and are hard to compute since they contain a wide range of spatial and temporal scales. The process of transition from laminar to turbulent flow was first investigated at the end of the 19^{th} century by Reynolds [2]. His work was based on the observations indicating that turbulence occurs as a consequence of instabilities that developed in the laminar boundary layer.

Turbulent benthic boundary layers are one of the most complex and important phenomena in oceanic fluid dynamics. For example, the high turbulence levels and

shear stresses produced by surface waves are believed to play an important role in determining the resuspension and transport of sediment. Moreover, shoaling surface waves create, in the boundary layer, turbulent shear flows at the seabed and thereby contribute significantly to wave energy dissipation. Mei [3] has shown that the wave bottom boundary layer makes the dominant contribution to wave energy dissipation rates in regions where active surface wave breaking does not occur. Knowledge of the bottom boundary layer is thus key to understanding the influence of the wave field on the sea floor, learning about the instabilities and the transitions to turbulence and quantifying the surface wave energy dissipation rates in this region.

The long-term objective of this study is to improve the understanding of turbulent benthic boundary layers in littoral waters. The primary goals are to make estimates of wave energy dissipation rates that occur in the boundary layer for different wave field conditions, that is for different wave amplitudes and wave frequencies, different shapes of wave (sine wave, skewed wave, complex wave, wave packet or steady flow), and various combined wave-current flows. The tool to investigate these processes is the high-resolution three-dimensional time-dependent numerical model developed by Slinn and Riley [4]. An attempt to gain improved understanding of the turbulent boundary layer has been done, including mechanisms of transition between laminar and turbulent flow regimes, and the influence of the presence of a mean flow. Improvements of the numerical computations of the three-dimensional model have also been implemented by increasing the order of accuracy of spatial derivatives.

In the past, three-dimensional boundary layer models were too computationally expensive to solve and reasonable approximations with experimental measurements could be obtained with one-dimensional models. One-dimensional models based on the turbulent eddy-viscosity concept have been tested here, based on the work done by Grant and Madsen [5] and Trowbridge and Madsen [6]. Analytic solutions for

laminar oscillatory boundary layer flows have also been analyzed, in order to better understand the behavior of initial transients in boundary layers and to analyze phases in which the flow is laminar. The tool of three-dimensional boundary-layer modeling is used to estimate the performance of these one-dimensional models for idealized flow conditions of a wave bottom boundary layer over a smooth plate with simplified wave oscillations.

This work involves theoretical analysis, numerical computations, and comparisons betweens numerical models and field and laboratory results. The thesis is organized as follows; first, a literature review is given in Chapter 2. This part reviews work done on the wave bottom boundary layer, such as the transition from laminar to turbulent flow, and various experiments and mathematical models developed to simulate the wave boundary layer and the wave-current motions. The characteristics of the boundary layer and the presentation of the governing equations of motion for the boundary layer flow are described in Chapter 3. The three-dimensional model of the wave bottom boundary layer, developed by Slinn and Riley [4], is reviewed in Chapter 4. A one-dimensional turbulent eddy-viscosity based model is introduced in Chapter 5. Results obtained with the three-dimensional model with different wave forcing conditions are compared to the eddy viscosity models in Chapter 6. The conclusions are presented in Chapter 7.

Chapter 2

Literature Review

Prandtl [1] introduced the boundary layer theory to resolve, for finite Reynolds number ($Re = \frac{U\delta}{\nu}$), the inaccuracy of the "irrotational" or "potential" flow solutions derived by neglecting viscosity (i.e., $Re \sim \infty$) near a solid surface. He postulated the existence, between irrotational flows and the stationary solid surface, of a thin layer of fluid in which the velocity increased from zero at the wall to the theoretical value of the potential flow at the edge of the layer. In such a "boundary layer", where the velocity gradient is high, viscous effects on the flow are important.

2.1 The Wave Bottom Boundary Layer

The wave bottom boundary layer has been studied extensively, using laboratory, and field experiments, numerical computations, and theoretical analysis.

One of the first problems in which the Navier-Stokes equations were solved was the oscillating plate problem. Stokes [7] determined the motion of the fluid over a flat plate plate oscillating in its own plane with a velocity $U_\infty(t) = U_m \sin \omega t$. Considering the x-momentum equation for a single velocity component $u(z,t)$ given by

$$\frac{\partial u}{\partial t} - \nu \frac{\partial^2 u}{\partial z^2} = 0, \tag{2.1}$$

where ν is the kinematic viscosity and z the vertical direction, positive upwards,

Stokes found a solution of the form

$$u(z,t) = U_m \sin(\omega t - \sqrt{\frac{\omega}{2\nu}} z) \exp(-\sqrt{\frac{\omega}{2\nu}} z). \tag{2.2}$$

Others have shown that the problem of an oscillatory stream over a stationary boundary is mathematically similar. The laminar flow solution satisfies the relation given by Batchelor [8]

$$\tau_0 = \frac{U_m^2 \cos(\omega t - \frac{\pi}{4})}{\sqrt{\frac{U_m A_m}{\nu}}}, \tag{2.3}$$

where U_m is the maximum free stream velocity amplitude, A_m the free stream particle amplitude or excursion length, such that $A_m = U_m/\omega$, and ω the wave frequency. Section 5.2 considers the related case of an oscillatory stream over a flat plate.

2.1.1 Laminar Boundary Layer

Jonsson [9] characterized the wave bottom boundary layer by two Reynolds numbers

$$Re_\delta = \frac{U_m \delta}{\nu} \qquad \text{(Boundary layer thickness Reynolds number)}, \tag{2.4}$$

$$RE_{A_m} = \frac{U_m A_m}{\nu} \qquad \text{(Amplitude Reynolds number)}, \tag{2.5}$$

where δ is the boundary layer thickness.

In the case of laminar flow, Jonsson [9] found a relation between the boundary layer thickness, δ, and the amplitude Reynolds number, RE_{A_m},

$$\frac{\delta}{A_m} = \frac{\pi}{\sqrt{2RE_{A_m}}}, \tag{2.6}$$

and between the boundary layer thickness and the maximum bottom shear stress during the wave period given by $\tau_{wmax} = \mu \frac{\partial u}{\partial z}\Big|_w = \frac{\nu}{\rho} \frac{\partial u}{\partial z}\Big|_w$,

$$\frac{\tau_{wmax}}{\rho} = \frac{\pi}{\sqrt{2}} \frac{\nu U_m}{\delta}, \tag{2.7}$$

where ρ is the fluid density and μ the dynamic viscosity. The wave boundary-layer thickness is thus inversely proportional to u^*_{wmax}/ω, in which u^*_{wmax} is the maximum shear velocity for the wave boundary-layer flow, given by

$$u^*_{wmax} = \sqrt{\frac{\tau_{wmax}}{\rho}}. \tag{2.8}$$

Jonsson [9] also defined the wave friction factor, f_w, in relation to the maximum bed shear stress, τ_{wmax}, by

$$\tau_{wmax} = \frac{1}{2}\rho f_w (A_m \omega)^2. \tag{2.9}$$

In laminar flow, the wave friction factor is given as a function of the amplitude Reynolds number, RE_{A_m}

$$f_w = \frac{2}{\sqrt{RE_{A_m}}}. \tag{2.10}$$

In the case of laminar flow, Jonsson [9] compared his results to Iwagaki *et* al. [10] experiments who directly measured the shear stress exerted on a smooth horizontal bottom by progressive shallow-water waves and found, that $f_w \sim 2/\sqrt{RE_{A_m}}$.

2.1.2 Transition from Laminar to Turbulent Flow

The wave boundary layer can be either laminar or turbulent. Several studies have been done to determine the ranges of laminar, transitioning, and turbulent flows.

Jensen *et* al. [11] examined turbulent oscillatory boundary-layer flows over smooth and rough bottoms for high Reynolds-number flows. Hino *et* al. [12] focused on experiments that lie inside the transitional flow regime. The free-stream velocity was forced to be purely oscillatory. Mean and turbulence measurements were carried out up to an amplitude Reynolds number of $RE_{A_m} = 6\text{x}10^5$ over a mirror-shine smooth bed. Friction coefficients as function of the amplitude Reynolds number, RE_{A_m}, were

determined as a function of the wave phase, ωt, to be

$$c_\omega = \frac{2\tau_w U_m^2}{\rho \cos(\omega t - \frac{\pi}{4})} \tag{2.11}$$

and are plotted in Figure 2.1.

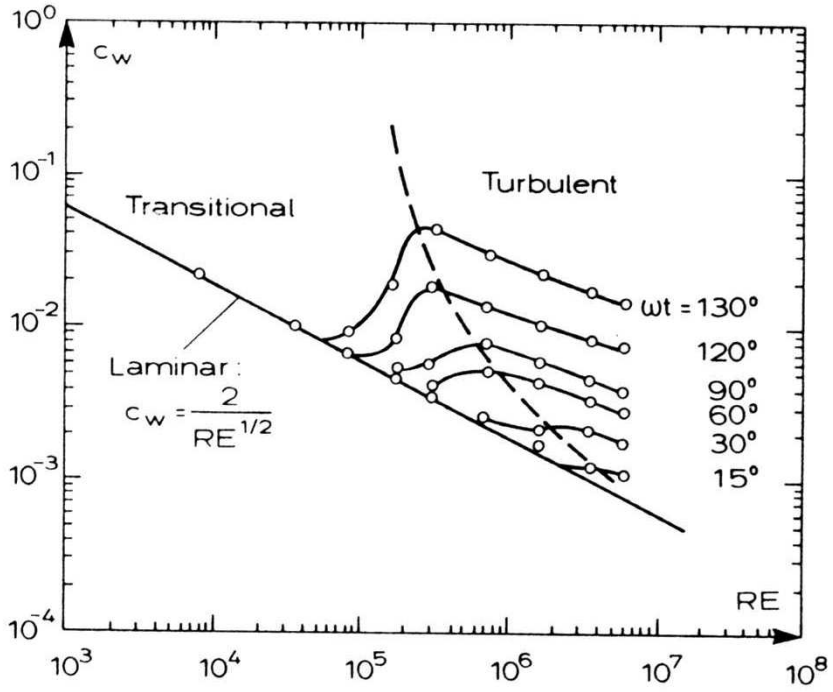

Figure 2.1: Normalized friction coefficient, c_ω, versus amplitude Reynolds number, $RE = RE_{A_m}$ at different phase values, ωt.

The friction coefficient is normalized with the cosine factor so that the laminar flow values collapse onto a common line. Figure 2.1 shows that every individual phase experiences three distinct flow states, the laminar, the transitional, and the turbulent, as the amplitude Reynolds number is increased. Moreover, the transition does not occur abruptly. For example, for $\omega t = 60°$, the transitional-flow state occurs over a range of amplitude Reynolds number from 1.5x10^5 to 1x10^6, and the flow becomes fully turbulent for RE_{A_m} >10^6. As ωt decreases, it is seen that the amplitude Reynolds-number

range, over which the turbulent flow occurs, shifts to higher Reynolds-number values. The critical value of the amplitude Reynolds number, $RE_{A_m cr}$, corresponding to the first appearance of turbulence is $RE_{A_m cr} \approx 10^5$, which is in fairly good agreement with the experimental data reported elsewhere in the literature (e.g., Spalart and Baldwin [13]). Even at higher frequency Reynolds number, however, the flow is not fully turbulent during the entire wave period. The bed shear-stress behavior as a function of time diverges as the Reynolds number increases.

In a laminar flow, the friction coefficient, c_ω, should be a constant and located on the curve $c_\omega = \frac{2}{\sqrt{RE_{A_m}}}$. From Figure 2.1, it can be observed that the flow is laminar for Reynolds numbers less than 5x10^4, but even at very high Reynolds numbers, the flow can be partly laminar at the phases where the outer flow velocity is small.

Kamphuis [14] determined the shear stress present at the bed for a number of fixed rougheness and smooth beds in an oscillating water tunnel. He measured the value of the friction factor and found that it is well described by the theoretical laminar friction factor for Reynolds number up to $RE_{A_m} = 3\text{x}10^5$, i.e., $f_w = 2/\sqrt{A_m^2\omega/\nu}$. In the transitional range, $3\text{x}10^5 < RE_{A_m} < 6\text{x}10^5$, the friction factor increases and then in the fully-developed smooth-wall turbulent regime, the friction factor decreases. Kamphuis [14] compared his results with the laboratory works of Kajiura [15] who determined the transition regime as $6.25\text{x}10^4 < RE_{A_m} < 4.23\text{x}10^5$ and found satisfactory agreement.

Jonsson [9] found that the laminar-smooth turbulent transition regime occurs between $RE_{A_m} = 10^4$ and $RE_{A_m} = 3\text{x}10^5$ and used in his paper $RE_{A_m} = 10^5$ as a transition value. He found that smooth-turbulence transition regime, in the case of open channel flow, fell in the range $250 < Re_\delta = \frac{U_m \delta}{\nu} < 500$ which corresponded to $1.26\text{x}10^4 < RE_{A_m} < 3.00\text{x}10^4$. In the case of wave bottom boundary layers, the flows were turbulent for $RE_{A_m} > 10^5$ or for $Re_\omega > 10^5$ where Re_ω is defined as the

frequency Reynolds number

$$Re_\omega = \frac{A_m^2 \omega}{\nu}, \tag{2.12}$$

which is equivalent to the amplitude Reynolds number, RE_{A_m}. This value of the frequency Reynolds number, $Re_\omega = 10^5$, will be used as the typical critical Reynolds number in the discussion below.

Fredsoe [16] also found that for values greater than about $RE_{A_m} = 5\text{x}10^5$, transition to turbulent flow occurs over smooth boundaries.

Several experimental investigations have been done on the variation in friction factor, $f_\omega = 2\tau_{wmax}/\rho U_m^2$, as a function of the Reynolds number. Results obtained by Kamphuis [14], Sleath [17], Jensen *et* al. [11] and Hino *et* al. [12] are presented in Figure 2.2.

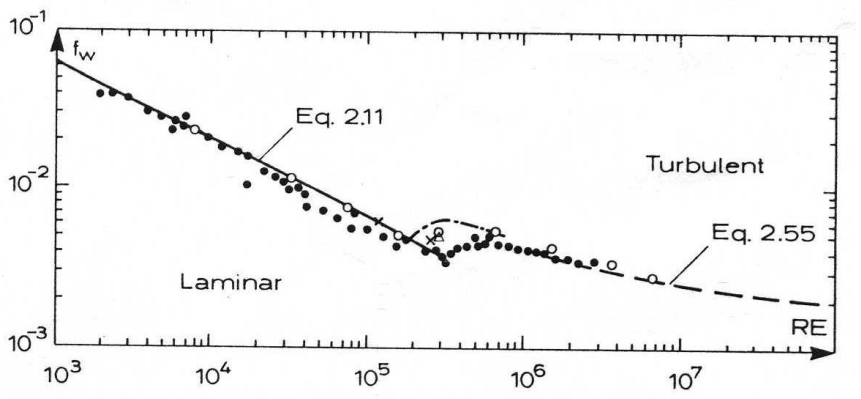

Figure 2.2: Experimental investigations on the variation in friction factor with the amplitude Reynolds number in flow over a smooth bed (•: Kamphuis [14], x: Sleath [17], ○: Jensen *et* al. [11], △: Hino *et* al. [12]).

It can be noticed that the transition from laminar to turbulent flow takes place for the amplitude Reynolds number in the interval $2\text{x}10^5 < RE_{A_m} < 6\text{x}10^5$.

2.2 Models of the Wave Bottom Boundary Layer

Relatively, few experiments in the wave bottom boundary layer have been performed, however, numerous mathematical models have been developed.

One of the first attempts to describe the oscillating turbulent boundary layer by a mathematical model was done by Kajiura [15]. In his model, the boundary layer is divided into three sublayers, an inner, an overlap and an outer layer, each with its characteristic mean turbulent viscosity $\nu_\tau(z)$. The eddy viscosity in the thin inner layer is taken as a constant. In the overlap layer, it is assumed to vary linearly with the distance from the bed and finally in the outer layer, the viscosity is kept constant from a certain distance away from the bed. The division of the boundary layer into three sublayers requires the estimate of the thickness of the different layers and the matching of the analytical solution at the interfaces. Thus, Kajiura [15] obtained a rather laborious analytical-numerical solution.

It would have been physically more reasonable to assume a form of the viscosity in the outer layer that decreases with height. For instance, Lundgren [18] assumed a form for the viscosity that increases linearly with z for small z and decreases exponentially for greater z, that is

$$\nu = \kappa |u_b(t)| z \exp(-\frac{z}{z_m}), \tag{2.13}$$

where z_m is the specified height of the maximum viscosity, $|u_b(t)|$ the magnitude of the friction velocity, and κ the von Kármán constant($\kappa \approx 0.4$).

Brevik [19] simplified the analysis of Kajiura [15]. He developed a two-layer theory of the oscillatory turbulent boundary layer over a rough surface by neglecting the inner layer, where the viscosity was kept constant in Kajiura's model [15]. Thus, no matching procedure is necessary for the lower overlap region. In contrast, however, to Kajiura's solution, Brevik's solution for the fluid velocity has to be specified at a

fixed level close to the bottom. This approach is somewhat common in the theory of turbulent uni-directional flow over a rough surface. Brevik's results show the usefulness of the two-layer theory as compared to the more complicated three-layer model and support the idea of introducing a turbulent viscosity, which is independent of time, at least in the near-bed region.

Kajiura [15] and Brevik [19] have tested their analytical results against the experiments done by Jonsson [20] and Jonsson and Carlsen [21] and have obtained reasonable agreement. They did not take into account, however, the possibility that the eddy viscosity could also be a function of time. The thickness of the wave boundary layer was also taken as a time-independent quantity and the variation in bed shear stress was assumed to be an harmonic function of time.

Jonsson and Carlsen [21] have removed some of these shortcomings by using the time-integrated momentum equation and by considering the velocity distribution in the near-wall region to be logarithmic. Since the momentum equations are integrated over a wave period, their approach was not able to describe the variation of the bed shear stress.

Grant and Madsen [5] assumed a viscosity of the form $\nu_\tau = \kappa u^*_{max} z$ for the complete range of the boundary layer, where u^*_{max} is the maximum bed shear stress during the wave period. The continued growth of the turbulent viscosity seems dubious since turbulence decreases in the upper portion of the boundary layer. The resulting velocity distributions, however, obtained with the Grant and Madsen model are generally in good agreement with laboratory results.

Physically, the eddy viscosity should not increase through the entire boundary layer, as is assumed in the Grant and Madsen's model [5]. The reason their approach is so successful is that $\dfrac{\partial u}{\partial z}$ tends to zero faster than the turbulent viscosity increases in the upper region of the boundary layer. Still, others have attempted

more realistic eddy-viscosity models employing either exponentially decaying (Long [22], Sanford [23]) or constant eddy viscosity (Kajiura [15], Brevik [19]) in the outer part of the boundary layer, that show good agreement with the velocity profile for different phases.

Although more recent models have been developed and some of other models, e.g., Brevik [19], have shown to produce results in slightly better agreement with existing laboratory measurements than the Grant and Madsen model [5], the differences between results based on the various models are small, and the Grant and Madsen model is generally accepted as a standard and a simpler model to implement than more complex one-dimensional models.

The model developed by Grant and Madsen [5] will be adopted in this work to estimate the wave bottom boundary layer with a one-dimensional model.

Grant and Madsen [5] discussed the physical justification of the eddy viscosity model, and derived an analytical solution for the velocity profile in terms of Kelvin functions for $\nu_\tau(z) = \kappa u^*_{max} z$. A theoretical study similar to the Grant and Madsen model [5] is reported by Lavelle and Mofjeld [24]. Lavelle and Mofjeld [24] produce a partly numerical solution and a detailed comparison with laboratory data is given to support the model. The semi-analytic model of Lavelle and Mojeld [24] is defined such that the flow and the time-variable viscosity are interdependent. Their eddy viscosity is given by

$$\nu_\tau(z) = \kappa|u_b(t)|z, \qquad z_0 \le z \le \delta, \tag{2.14}$$

$$\nu_\tau(z) = \kappa|u_b(t)|\delta, \qquad \delta \le z, \tag{2.15}$$

where the magnitude of the modified friction velocity $|u_b(t)|$ is

$$|u_b(t)| = [u^{*2}(t) + \varepsilon^2 u^{*2}(t + \frac{\pi}{4})]^{1/4}, \qquad \varepsilon \simeq 0.2. \tag{2.16}$$

This model shows that neglecting time variations in viscosity results in underestimates of maximum bottom stress and distortion of the flow profile near times at flow reversal.

Trowbridge and Madsen [6] present an analysis of oscillatory boundary layer flows induced by linear surfaces waves near a rough bottom. The flow is produced by a train of plane, progressive, monochromatic surface waves traveling across a sea of constant depth with a fixed rough bottom. The Reynolds-averaged horizontal velocity just outside the near-bottom boundary layer is given by the expression

$$U_\infty(x,t) = A_m\omega\cos\theta \qquad (\theta = \omega t - kx), \tag{2.17}$$

where $k = 2\pi/\lambda$ is the wavenumber and λ the wave length. As $U_\infty(x,t)$ is symmetric in time, i.e., $U_\infty(x,t) = -U_\infty(x, t \pm \pi/\omega)$, the velocity and the stress inside the boundary layer must have the same property, and only contain odd harmonics of the fundamental frequency. These quantities can be expressed in the following general form

$$U(x,z,t) = \Re[\Sigma_{n=0}^{\infty} U^{(2n+1)}(z) e^{it(2n+1)\theta}], \tag{2.18}$$

$$\tau_{zx}(x,z,t) = \Re[\Sigma_{n=0}^{\infty} \tau^{(2n+1)}(z) e^{it(2n+1)\theta}], \tag{2.19}$$

where $U^{(2n+1)}$ and $\tau^{(2n+1)}$ are some complex functions of z and $\Re$ represents the real part. The turbulent eddy viscosity relates the Reynolds shear stress to the ensemble-averaged velocity gradient such that

$$\tau_{zx} = \rho\nu_\tau \frac{\partial U}{\partial z}, \tag{2.20}$$

Thus the comparison of these last three equations shows that the eddy viscosity contains only even harmonics of the fundamental frequency and can be expressed as

$$\nu_\tau(x,z,t) = \Re[\Sigma_{n=0}^{\infty} \nu^{(2n)}(z) e^{it2n\theta}], \tag{2.21}$$

where $\nu^{(2n)}$ is complex.

Most existing analytical models of turbulent benthic boundary layers are based on a time-invariant eddy viscosity, however, in reality, the eddy viscosity varies with time. Trowbridge and Madsen [6] assume the viscosity to be the product of a vertical length scale and the first two Fourier components of a time-varying shear velocity based on the instantaneous value of the bed shear stress

$$\nu_\tau(x,z,t) = \nu^{(0)}\Re[1 + a^{(2)}e^{i2\theta}], \tag{2.22}$$

$$\nu^{(0)} = \kappa\overline{u}_f \begin{cases} ,z & 0 \le z \le \delta_1 \\ \delta_1 & \delta_1 \le z \end{cases} \tag{2.23}$$

δ_1 being equal to $l/6$, where l is a length characterizing the boundary layer thickness. The real constant $\overline{u}_f = \left|\frac{\tau}{\rho}\right|^{1/2}$ is the shear velocity that characterizes the average turbulence intensity over the wave period and the complex constant $a^{(2)} = \overline{2e^{-i2\theta}\left|\frac{\tau}{\rho}\right|^{1/2}}$ represents the amplitude of the temporal variation of the viscosity, where an overbar denotes a time average over one wave period. Using this model, an approximate analytical solution of the equation of motion can be obtained and comparisons with laboratory measurements indicate that the turbulent eddy viscosity varies with time and that the theoretical approach used is physically sound.

Results from Trowbridge and Madsen [6] will also be compared to the three-dimensional model in this work.

Trowbridge and Madsen [6] assumed that the time-varying part of the viscosity has the same vertical structure as the steady part. In reality, the time-varying component is believed to decay more rapidly with distance above the bed than does the steady part. One could model this effect by assuming that temporal variation of the eddy viscosity is confined to be in the inner part of the boundary layer ($0 < z < l/6$). This exercise was carried out by Trowbridge [25] with no qualitative difference between the results obtained, allowing the time variation to extend to δ.

2.3 Wave-Current Boundary Layer Models

Accurate knowledge of the combined wave-current motion is vital for wave forecasting and sediment transport, the sediment being usually suspended into the water column by the waves and transported by the current. Introducing steady mean currents on the wave motion adds to the difficulty of estimating shear and dissipation in the boundary layer. In the case of wave-current flows, the turbulence is not restricted to the thin wave boundary layer, but can extend to the whole water depth. The interaction of the two kinds of turbulence is highly nonlinear.

The flow depth in the combined wave-current motion can be divided into roughly three zones, according to Lundgren [18]. In the upper zone, the turbulence is purely associated with the mean current and the turbulent characteristics are independent of the waves. In the transition zone, the turbulent motions produced by the wave boundary layer are of the same order of magnitude as those supported by instabilities of the mean current. Finally, the lower zone is dominated by wave-produced turbulence. The vertical extent of each zone depends on the relative strengths of waves and current; if the current becomes very strong compared to the waves, the wave zone may vanish. The change in the turbulent structure due to the presence of waves implies that the vertical distribution of the mean current profile will also be different.

Lundgren [18] utilized the measurements of the eddy viscosity in the pure wave boundary layer from Jonsson [20] to determine a theory for the combined wave-current motion using the eddy-viscosity concept. The eddy viscosity was taken as the mean viscosity over one wave period. Lundgren's model is a time-averaged model which does not take into account the variations with time of the boundary layer.

A simplified model based on Lundgren's ideas was later developed by Fredsoe [16]. Fredsoe [16] considered both the case of a pure oscillating wave boundary layer,

assuming the velocity profile near the wall to be logarithmic and the combined wave-current motion. The mean current velocity profile in the combined wave-current flow is calculated using the depth-integrated momentum equation in the direction perpendicular to the mean current. The velocity distribution is assumed to be logarithmic inside as well as outside the wave boundary layer, but with different slopes. Using this approach, the flow can be determined across the whole range from the pure wave motion to the pure current motion.

Grant and Madsen [26] have developed, using the eddy viscosity concept, a more detailed model for combined wave-current flow than that of Lundgren [18]. In this approach, the eddy viscosity and the boundary layer thickness are assumed to be constant in time and all variations with time are assumed to be sinusoidal. The addition of a wave on the steady current above the wave boundary layer results in an increase in the apparent roughness experienced by the current. The eddy viscosity model proposed by Grant and Madsen [26] focuses on the case of a steady current interacting with monochromatic, uni-directional waves over a rough bottom, with roughness elements small in comparison to the thickness of the wave boundary layer. Turbulent closure is accomplished by employing a time invariant turbulent eddy-viscosity model, which varies linearly with distance from the bed as $\nu_\tau(z) = \kappa u^*_{max} z$. In the vicinity of the bed, the velocity profile under a steady uni-directional flow shows little sensitivity to the choice of either a linear or parabolic distribution of the viscosity, thus the simpler linearly form is used in this model. In the model, the x- and y-axes are oriented in the cross-shore and along-shore directions, respectively and the z-axis is vertical, positive upward. The direction of wave propagation is along the x_1-axis, which is inclined at an angle of incidence θ to the x-axis. The velocity components in the x- and y-directions are u and v, respectively and the wave-induced velocity in the x_1- direction is denoted u_1. The mean flow is assumed to be in the

along-shore direction. A closed form solution is possible in terms of Kelvin functions for the wave-induced velocity of the form

$$u_1(z,t) = \Re\left[\widehat{u_\infty}\left(1 - \frac{ker(2\sqrt{\xi} + ikei(2\sqrt{\xi})}{ker(2\sqrt{\xi_0} + ikei(2\sqrt{\xi_0})}\exp(i\omega t)\right)\right], \tag{2.24}$$

where $\widehat{u_\infty}$ is the free-stream complex velocity just outside the boundary layer, $\xi = \frac{(z-\triangle)}{l}$ the non-dimensional vertical boundary layer coordinate, $\triangle$ being the displacement height of the bottom, z_0 the bottom roughness parameter and l a length scale equal to $\kappa u^*/\omega$, $\xi_0 = z_0/l$, and ker and kei are zeroth-order Kelvin functions. In the case of pure oscillatory wave, the predictions of the velocity magnitude give good agreements with experimental results of Jonsson and Carlsen [21] however the phase of the velocity is not so well predicted.

Smith [27] has taken a similar approach, however, his model treats only the co-directional flow cases and assumes that the problem of interest is the interaction of waves and currents in a current-dominated environment, whereas Grant and Madsen [26] approach the problem from the opposite end.

Bakker and Doorn [28] applied mixing length theory, assuming that the mixing length was proportional with the distance from the bed, and included in their model the time variation in the eddy viscosity. The assumption of a mixing length hypothesis, however, in a strongly unsteady flow is questionable. The work by Bakker and Doorn [28] is restricted to the two-dimensional (x-z) case, in which the current and the wave propagation are in the same direction, while Grant and Madsen [26] consider three-dimensional flow.

Myrhaug and Slaattelid [29] developed a theoretical model describing the motion in combined wave and current boundary layers near fixed rough sea-beds. A three-layer time invariant eddy viscosity model was employed. The inner layer is dominated by the waves and the eddy viscosity increases quadratically with distance from the

sea-bed and then is constant from a certain height. The combined flow demonstrates a clear reduction in the steady component of the velocity near the sea-bed compared with the no waves situation. Comparison with experimental data support the model results.

Christoffersen and Jonsson [30] used two simple two-layer linearly varying eddy-viscosity models. These models have the same viscosities in the current boundary layer but different viscosities in the wave boundary layer.

Most of the existing theoretical models, e.g., Grant and Madsen [26], Myrhaug and Slaattelid [29], and Christoffersen and Jonsson [30] suggest that the addition of a current to a wave boundary layer will increase the turbulence intensity and the eddy viscosity in the bottom boundary layer. Hence the wave boundary layer thickness should increase as $\sqrt{\nu/\omega}$. The experimental data, however, indicate that the effect is weaker than the models have predicted.

Laboratory experiments have been conducted in channels with smooth and rough beds by Kemp and Simons [31], for wave flow only, mean current only, and wave-current flow propagating in the same direction. They investigated the interaction between a turbulent current and surface gravity waves of different amplitudes. The mean velocity profile was found to follow the law of the wall for a current flow. Adding a current in the direction of the wave propagation makes the waves longer in trough and crests sharper. The maxima and minima of the periodic wave-induced velocity near the bed are also reduced. The main effects of introducing a wave are to reduce the mean velocity in the upper layers and increase it in the turbulent boundary layer near the bed. The uni-directional turbulent boundary layer is reduced in thickness by the superposition of waves and the maximum horizontal turbulence intensity for the combined wave-current flow is 20 % higher than for the current alone.

Van Doorn [32] measured the velocity profile for a pure current, a pure wave, and

a combined wave-current flow in an oscillating water tunnel. His experiments indicate that the structure of the oscillatory flow is unchanged by the addition of the current but that the addition of the waves changes the current profile considerably.

Measurements from Sleath [33], in the case of perpendicular combined wave-current flow showed little or no change to the wave boundary layer structure due to superimposed currents of moderate strengths.

Measurements from Kemp and Simons [31], Van Doorn [32], and Sleath [33] show that the influence of a mean current over a wave flow depend on the intensity of the mean current.

2.4 Direct Numerical Simulations of a Turbulent Boundary Layer

Spalart and Baldwin [13] were first to develop a three-dimensional Navier-Stokes solver for the direct numerical simulations of an oscillatory turbulent boundary layer. Their model used a spectral method in a semi-infinite domain, perpendicular to the boundary and two periodic directions horizontally. The spectral basis functions used in their model are well adapted to the flow and confirm results given by linear theory. The oscillating boundary layer flow displayed complex behavior, a function of the phase angle, ωt, and the Reynolds number, $Re_{\delta_s} = U_m \delta_s / \nu = U_m \sqrt{2/\nu\omega}$, where δ_s is the Stokes boundary layer thickness. A first transition from laminar to pre-turbulent regime occurs just below $Re_{\delta_s} = 600$. A turbulent state, during at least part of the cycle, is well-developed after a second transition for $600 < Re_{\delta_s} < 800$. In this regime, small disturbances of the flow decay in time and large disturbances destabilize the boundary layer.

Vittori and Verzicco [34] recently performed three-dimensional numerical simulations of the Stokes boundary layer over a wall with small imperfections to analyze

the process of transition from the laminar to turbulent flow. Their model used, a periodic domain in the streamwise and spanwise directions, with standard central second-order finite difference spatial approximations and a fractional-step method in time. Comparisons to analytical (Blondeaux [35]) and experimental (Jensen [11]) results gave good agreements. Imperfections of the wall were of fundamental importance in causing the growth of two-dimensional disturbances. As $Re_{\delta_s} > 550$, the flow is found to be intermittently turbulent. They observed that the accelerating part of the wave cycle is characterized by turbulence production and that the decelerating phase induced a dissipation of energy.

Akhavan *et* al. [36] investigated the stability of oscillatory two-dimensional channel flow to different small disturbances by direct numerical simulations of the Navier-Stokes equations using spectral techniques. They concluded that transition to turbulence in oscillatory Stokes layers can be explained by a secondary instability mechanism of two-dimensional finite-amplitude waves to a three-dimensional infinitesimal instability mechanism. They also found a transitional Reynolds number of the order of $Re_{\delta_s} = 500$.

2.5 Field observations of the wave bottom boundary layer

Foster *et* al. [37] present field measurements of the wave bottom boundary layer cross-shore velocity within the surf zone. Evidence for the velocity overshoot in the boundary layer is shown. The observations are compared with two linear eddy viscosity models based on that of Smith [27] and Foster *et* al [38]. Overestimates of the eddy viscosity and underestimates of the phase are found. These observations are among the first coherent looks at the wave bottom boundary layer in the nearshore region.

Sarpkaya [39] investigated experimentally the creation and development of low-speed streaks and coherent structures (e.g., arches, hairpins) on a long cylindrical body immersed in an oscillating flow. Stability of the flow is dependent on strong pressure gradients, inflections points in velocity profiles and shear stress reversal. The transitional and turbulent states, dependent of the Reynolds number, $Re_\delta = U_{max}\delta/\nu$, present vortical motions which burst themselves during periods of decelerating flows.

Gad-El-Hak *et* al. [40] experimentally investigated the stability of decelerating boundary-layer flows. The boundary layer becomes unstable to two-dimensional waves, which become three-dimensional, generating hairpin vortices and turbulent bursts. The boundary layer equations have also been solved numerically, the stability analysis being done using the Orr-Sommerfeld equation. Comparison of velocity profiles are consistent with the observations and measurements made.

Piomelli *et* al. [41] studied vortical structures in spatially developing turbulent boundary layers subjected to flow acceleration in two cases, low and strong accelerations. In the mild-acceleration case, an equilibrium of the boundary layer is obtained. The structure of turbulence is modified, longer streaks and fewer coherent vortices are observed. In strongly accelerating cases, the flow tends to approach the laminar profile. The turbulent kinetic energy increases less rapidly than the energy of the mean flow.

Chapter 3

The Boundary Layer Theory

3.1 The Boundary Layer

The region of fluid near a boundary (body, wall, mixing layers between two portions of flow moving at different speeds ...), the so-called boundary layer, is normally very thin, perhaps a few millimeters over a smooth, solid bed and a few centimeters over a flat bed of loose sand. This layer is affected by the velocity shear produced at the boundary; the viscosity μ, a fluid property, exerts an essential influence in this domain.

The existence of intermolecular attractions near the boundary causes the fluid to adhere to the boundary and this gives rise to a shear stress τ_w given by Newton's friction law

$$\tau_w = \mu \frac{\partial u}{\partial z}\Big|_w, \tag{3.1}$$

On the other hand, in the remaining region, no such large velocity gradients generally occur and the effect of viscosity is less important; the flow is potential, frictionless, and can be approximated by the inviscid-fluid theory.

The inner layers of a real fluid transmit normal and tangential stresses. Because of the presence of the tangential forces, there exists on the boundary no difference in relative tangential velocities, that is the velocity of the flow on the boundary is the

same as the velocity of the boundary; this phenomenon is called the no-slip condition. A sketch of a boundary layer flow over a flat plate is represented in Figure 3.1.

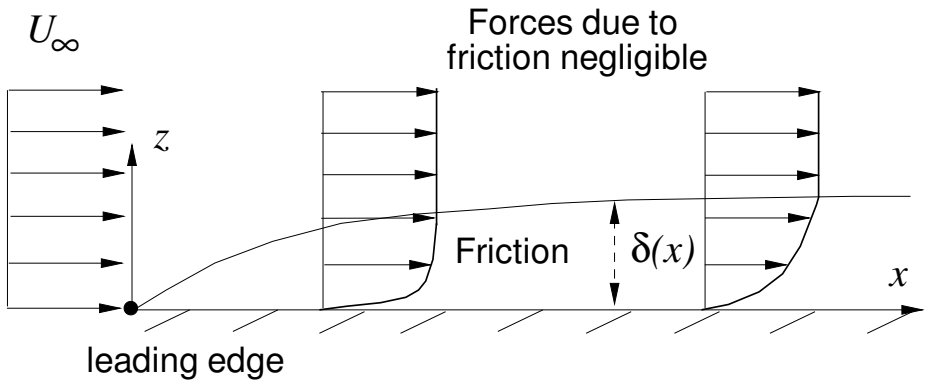

Figure 3.1: Boundary layer flow over a flat plate under a free stream velocity U_∞.

This figure represents both the boundary layer flow, where friction is important, and the outer flow, where viscosity effects are negligible. In the boundary layer, the velocity of the fluid increases gradually with the distance from the leading edge from zero (no slip-condition) to its full value which corresponds to the external frictionless flow, U_∞.

The characteristic length of the boundary layer is the boundary layer thickness, δ, which is generally defined as the distance from the wall where the velocity differs by 1 percent from the external velocity. In this example, the boundary layer thickness is a function of the distance from the leading edge in the downstream direction. For laminar flow, δ increases continuously in proportion to $\sqrt{x}$. Moreover, as it is also proportional to the square root of the viscosity ($\delta \propto \sqrt{\nu T}$, T flow period in the cases of oscillatory flow and time in the case of impulsively started flow), the boundary layer thickness increases with the viscosity or more generally decreases as the downstream Reynolds number $Re_x = U_\infty x/\nu$ increases.

Near the leading edge, the boundary layer is always described as laminar as the streamlines are nearly parallel to the surface. So long as the local Reynolds number is below a certain limit (depending on the type of flow or boundary) the motion within the boundary layer is stable. When a critical number is exceeded, the flow in the boundary layer becomes unstable, with vortex formations, apparition of bursts of turbulence in places of high local vorticity, and coalescence of turbulent spots occurs and a fully turbulent boundary layer can develop.

3.2 Governing Equations of the Boundary Layer

The equations of motion of a three-dimensional boundary layer flow are described by the Navier-Stokes equations.

The inviscid-flow theory fails near the boundary because the proper scale for viscous effects is not L (length of the wall in the direction of the flow, for example) but δ, the boundary layer thickness. Thus, the derivatives of the velocity across the boundary layer, i.e., $\dfrac{\partial u}{\partial z}$, would be underestimated by U_∞/L in the inviscid theory whereas this derivative would be of the order U_∞/δ.

Considering forced, dissipative, incompressible flow within the Boussinesq approximation (Phillips [42]), the dimensional conservation equations for mass and momentum in the boundary layer are, respectively,

$$\frac{\partial u}{\partial x}+\frac{\partial v}{\partial y}+\frac{\partial w}{\partial z}=0 \quad \text{Equation of continuity,} \tag{3.2}$$

$$\frac{\partial u}{\partial t}+u\frac{\partial u}{\partial x}+v\frac{\partial u}{\partial y}+w\frac{\partial u}{\partial z}=-\frac{1}{\rho}\frac{\partial p_t}{\partial x}+\nu\left(\frac{\partial^2 u}{\partial x^2}+\frac{\partial^2 u}{\partial y^2}+\frac{\partial^2 u}{\partial z^2}\right)+F_x \quad x\text{-momentum equation,} \tag{3.3}$$

$$\frac{\partial v}{\partial t}+u\frac{\partial v}{\partial x}+v\frac{\partial v}{\partial y}+w\frac{\partial v}{\partial z}=-\frac{1}{\rho}\frac{\partial p_t}{\partial y}+\nu\left(\frac{\partial^2 v}{\partial x^2}+\frac{\partial^2 v}{\partial y^2}+\frac{\partial^2 v}{\partial z^2}\right)+F_y \quad y\text{-momentum equation,} \tag{3.4}$$

$$\frac{\partial w}{\partial t} + u\frac{\partial w}{\partial x} + v\frac{\partial w}{\partial y} + w\frac{\partial w}{\partial z} = -\frac{1}{\rho}\frac{\partial p_t}{\partial z} - g + \nu(\frac{\partial^2 w}{\partial x^2} + \frac{\partial^2 w}{\partial y^2} + \frac{\partial^2 w}{\partial z^2}) + F_z$$

z-momentum equation, (3.5)

where the components of the fluid velocity (u, v, w), respectively along the x-, y-, and z-axis, and the total pressure p_t are the unknowns. The Cartesian coordinates (x, y, z) are respectively aligned across-shore, along-shore, and vertically, positive upwards, t is time, g is the gravitational acceleration, ρ the constant fluid density, ν the kinematic viscosity, and (F_x, F_y, F_z) the x-, y- and z-components, respectively, of a body force.

The pressure field can be written as $p_t = p_0 + p$, where p_0 is a reference state in hydrostatic balance with the background density field, e.g.,

$$p_0 = -\rho g z. \tag{3.6}$$

The governing equations may be nondimensionalized as follows

$$x^* = \frac{x}{L}, \qquad u^* = \frac{u}{U}, \qquad t^* = t\frac{U}{L}, \qquad p^* = \frac{p}{\rho U^2}, \qquad F_x^* = F_x\frac{L}{U^2}\cdots, \tag{3.7}$$

where U is the characteristic velocity, L a characteristic length scale and pressure p is nondimensionalized with the dynamic pressure. Dropping the *'s, and using the material derivative, $\frac{D}{Dt} = \frac{\partial}{\partial t} + u\frac{\partial}{\partial x} + v\frac{\partial}{\partial y} + w\frac{\partial}{\partial z}$, and substracting (3.6) from the z-momentum equation, the governing equations can be rewritten in nondimensional form

$$\frac{\partial u}{\partial x} + \frac{\partial v}{\partial y} + \frac{\partial w}{\partial z} = 0, \tag{3.8}$$

$$\frac{Du}{Dt} = -\frac{\partial p}{\partial x} + \frac{1}{Re}(\frac{\partial^2 u}{\partial x^2} + \frac{\partial^2 u}{\partial y^2} + \frac{\partial^2 u}{\partial z^2}) + F_x, \tag{3.9}$$

$$\frac{Dv}{Dt} = -\frac{\partial p}{\partial y} + \frac{1}{Re}(\frac{\partial^2 v}{\partial x^2} + \frac{\partial^2 v}{\partial y^2} + \frac{\partial^2 v}{\partial z^2}) + F_y, \tag{3.10}$$

$$\frac{Dw}{Dt} = -\frac{\partial p}{\partial z} + \frac{1}{Re}(\frac{\partial^2 w}{\partial x^2} + \frac{\partial^2 w}{\partial y^2} + \frac{\partial^2 w}{\partial z^2}) + F_z, \tag{3.11}$$

where Re is the nondimensional Reynolds number given by

$$Re = \frac{UL}{\nu}. \tag{3.12}$$

Chapter 4

The Three-Dimensional Wave Bottom Boundary Layer Model

4.1 The Numerical Model

A three-dimensional numerical model has been developed by Slinn and Riley [4] for Direct Numerical Simulations (low Reynolds number) and Large Eddy Simulations (large Reynolds number) of a turbulent boundary layer flow. The numerical model is based upon the full Navier-Stokes equations (3.2), (3.3), (3.4), and (3.5), with an external pressure gradient $F_x = \frac{\partial p_\infty}{\partial x}$ added to the x-momentum equation to force current external to the boundary layer.

Shoaling surface waves create turbulent shear flows in the boundary layer at the sea floor and thereby make significant contributions to wave energy dissipation rates, and fluid sediment interactions. The dissipation rate is given in a three-dimensional flow by

$$\begin{aligned} \varepsilon(x,y,z,t) &= \nu\Big[2\Big(\frac{\partial u}{\partial x}\Big)^2 + 2\Big(\frac{\partial v}{\partial y}\Big)^2 + 2\Big(\frac{\partial w}{\partial z}\Big)^2 + \Big(\frac{\partial v}{\partial x} + \frac{\partial u}{\partial y}\Big)^2 + \\ &\quad \Big(\frac{\partial w}{\partial y} + \frac{\partial v}{\partial z}\Big)^2 + \Big(\frac{\partial u}{\partial z} + \frac{\partial w}{\partial z}\Big)^2\Big] \end{aligned} \tag{4.1}$$

The three-dimensional model domain under a progressive wave, of length $\lambda \sim 100$

m and height $H = 2\eta \sim 2$ m, propagating at a velocity C_{ph} at a water depth $h \sim 5$ m, is drawn in Figure 4.1.

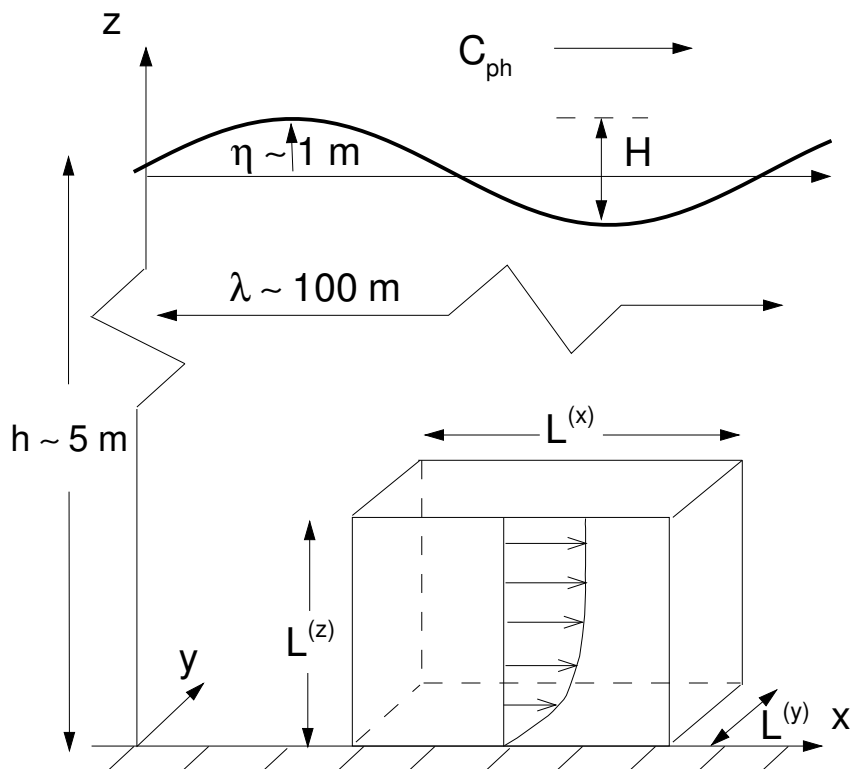

Figure 4.1: Horizontally periodic boundary layer domain (dimensions of the order of 10 cm^3) under a progressive wave of height H, length λ and depth h.

The wall at the bottom boundary is considered to be smooth. The dimensions are $L^{(x)}$, $L^{(y)}$, and $L^{(z)}$ along the x-, y- and z-axis, respectively. Experiments have been conducted using, for example, $L^{(x)} = 10$ cm, $L^{(y)} = 7.5$ cm, and $L^{(z)} = 5$ cm.

In order to simplify lateral boundary conditions, the model geometry is periodic in the alongshore x- and across-shore y-directions such that

$$(u, v, w, p)(x, y, z, t) = (u, v, w, p)(x + L^{(x)}, y, z, t) \tag{4.2}$$

$$(u, v, w, p)(x, y, z, t) = (u, v, w, p)(x, y + L^{(y)}, z, t) \tag{4.3}$$

The periodicity allows only certain discrete spatial modes to exist in the computed flow. If the dominant modes present, however, are small compared to the periodic dimensions, this approximation can be accepted. The dimension of the domain in the x-direction, $L^{(x)}$, is small compared to the wave length λ. A consequence of the periodic approximation in the x-direction is that boundary layer streaming (Batchelor [8]) is not allowed in the model.

Moreover, no slip (and no penetration) boundary conditions are specified at the bottom boundary ($z = 0$) with

$$(u, v, w)(x, y, 0, t) = 0, \tag{4.4}$$

The open boundary condition at the upper boundary is implemented using a Rayleigh damping sponge layer (Durran, et al. [43]) that corresponds to 10 percent of the total grid points in the vertical direction and absorbs disturbances propagating upwards from the boundary layer.

In this model, the simple harmonic oscillatory wave induced velocity above the seabed is given by

$$U_\infty(t) = U_m \sin(\omega t + \varphi) = A\omega \sin(\omega t + \varphi), \tag{4.5}$$

where φ is the phase of the velocity. This velocity is commonly included in the range 10-100 cm s^{-1} and the typical boundary layer thickness, δ_τ, is of the order of 0.5-10 cm. These values lead to typical boundary layer thickness Reynolds numbers between 500 and 100,000, where the boundary layer thickness Reynolds number is given by

$$Re_{\delta_\tau} = \frac{U_m \delta_\tau}{\nu}. \tag{4.6}$$

Because of the oscillatory behavior of the external flow, an inflectional instability is induced during phases of flow deceleration and flow reversal. The most important pa-

Cases	U_m, V_m (m s^{-1})	T (s)	δ_τ (cm)	Re $\frac{U_m L^{(z)}}{\nu}$	Re_ω $\frac{U_m^2 T}{2\pi\nu}$	Re_{δ_τ} $\frac{U_m \delta_\tau}{\nu}$	$Re_{\delta s}$ $U_m\sqrt{\frac{T}{\nu\pi}}$
1	0.80, 0.0	5	2	40,000	510,000	16,000	1,009
2	0.60, 0.0	5	1	30,000	290,000	6,000	757
3	0.40, 0.0	5	0	20,000	130,000	0	504
4	0.20, 0.0	5	0	10,000	32,000	0	252
5	0.80, 0.0	3	0.5	40,000	300,000	4,000	782
6	0.80, 0.0	8	2.5	40,000	815,000	20,000	1,277
7	0.80, 0.0	12.5	3	40,000	1,270,000	24,000	1,596
8	0.80, 0.0	∞	4.	40,000	∞	32,000	∞
9	0.80, 0.0	5	2.5	40,000	510,000	20,000	1,009
10	1.0, 0.0	11	1.2	50,000	1,750,000	12,000	1,009
11	0.80, 0.0	60	2	40,000	6,115,000	16,000	3,497
12	0.60, 0.15	5	0.6	31,000	307,000	3,700	782
13	0.60, 0.30	5	2.5	33,500	530,000	16,700	845
14	0.60, 0.60	5	4.5	42,000	575,000	37,800	1060

Table 4.1: Characteristics of the different experiments.

rameter, for determining transition to turbulence, is the frequency Reynolds number (Jonsson [9])

$$Re_\omega = Re_{Am} = \frac{A_m^2\omega}{\nu} = \frac{U_m A_m}{\nu} = \frac{U_m^2}{\omega\nu} = \frac{U_m^2 T}{2\pi\nu}, \tag{4.7}$$

where T is the wave period.

The Stokes's Reynolds number is also defined as

$$Re_{\delta_s} = \frac{U_m \delta_s}{\nu}, \tag{4.8}$$

where the Stokes's boundary layer thickness δ_s is given by

$$\delta_s = \sqrt{\frac{2\nu}{\omega}}. \tag{4.9}$$

The various Reynolds numbers are presented for the several numerical experiments in Table 4.1.

In natural conditions, the flow outside the boundary layer (tides, wind-generated waves) is a complicated function of time, however, we shall generally consider the tides and currents as quasi-steady flows and the waves as harmonic oscillations.

The time average, the horizontal average in the x- and y-directions and the volume average of a quantity $G(x, y, z, t)$ are respectively given in the model by

$$\overline{G} = \frac{1}{\triangle t} \int_{t_i}^{t_f} G(x, y, z, t) dt, \tag{4.10}$$

$$\langle G \rangle = \frac{1}{L^{(x)} L^{(y)}} \int_0^{L^{(y)}} \int_0^{L^{(x)}} G(x, y, z, t) dx dy, \tag{4.11}$$

$$\langle\langle G \rangle\rangle = \frac{1}{L^{(z)} L^{(y)} L^{(z)}} \int_0^{L^{(z)}} \int_0^{L^{(y)}} \int_0^{L^{(x)}} G(x, y, z, t) dx dy dz, \tag{4.12}$$

where $\triangle t = t_f - t_i$, and $L^{(x)}$, $L^{(y)}$, and $L^{(z)}$ are the dimensions of the domain, as shown in Figure 4.1. Moreover, variables, such as the velocity, may be divided into time-average and fluctuating parts such as

$$G(x, y, z, t) = \overline{G} + \tilde{G}(x, y, z, t) \tag{4.13}$$

where $\tilde{G}$ is the fluctuating part or horizontal averages and fluctuations

$$G(x, y, z, t) = \langle G \rangle + G'(x, y, z, t), \tag{4.14}$$

where G' is the fluctuation about the mean.

The model uses uniform grid spacing in the x- and y-directions and non-uniform or clustered grid spacing along the z-axis, for better resolution in the strong shear layer at the bottom boundary. The standard resolutions for the model are 65x65x130 grid points in low resolution, in the x-, y-, and z-directions, respectively, or up to 257x129x130 grid points for a better resolution. To optimize the computational efficiency of some experiments, simulations are begun at low resolution, and regridded

to higher resolution when the flow transitions to turbulence. This is accomplished by decreasing the step sizes in the horizontal directions, $\triangle x$ and $\triangle y$, by a factor of 2 and using Fourier interpolation to initialize the velocity field on the refined mesh. It is typical for a high resolution experiment to take approximately 1-2 months of CPU time on a Dec-Alpha 600au (circa 1999, $\sim \$20,000$) workstation.

4.2 Numerical Methods

4.2.1 The Numerical Model

The basic numerical model is described in detail in Slinn and Riley [4]. The model simulates forced, dissipative, incompressible flow. During simulations, the free-stream oscillation is forced continuously from inside the computational domain, utilizing the forcing term $F_x = \dfrac{\partial p_\infty}{\partial x}$ of the x-momentum equation.

Low level white noise is included as part of the initial conditions, and the wave forcing is generally started from rest at $t = 0$. The numerical scheme employs the pressure projection method, implemented with a variable time step third-order Adams-Bashforth scheme to achieve high temporal accuracy. The pressure field is determined by solving a Poisson equation using Fourier transforms in the lateral x- and y- directions and a fourth-order direct solution method in the vertical z-direction.

For the higher Reynolds number experiments, e.g., for $Re_{\delta_\tau} > 10,000$ the model incorporates additional artificial numerical dissipation at the smallest resolved length scales. This is performed by adding hyperviscosity terms to the momentum equations, e.g., $\mu\nabla^6\vec{u}$, with $\mu \ll 1$ and $\vec{u}$ the velocity field, to filter energy at poorly resolved scales. Since the boundary layer dynamics are microscale driven, modeling of small-scale dissipation, with length scales of approximately 1 mm, with a hyperviscosity does not dominate or invalidate the results obtained.

4.2.2 Compact Scheme

A variety of numerical schemes are used in the model. The model of Slinn and Riley [4] originally employed fourth-order compact scheme derivatives. In the present work, the accuracy of the spatial derivatives has been upgraded to sixth-order. The velocity derivatives are calculated using Hermitian compact or Padé series techniques, following the work of Hirsh [44], Adam [45], and Lele [46]. Additional details of the schemes are given in Appendix A.

The more restrictive numerical stability limits for the sixth-order scheme, which are the time step limits needed to maintain a numerically stable solution, have been determined, based on one-dimensional advective and diffusion equations. Considering a pure advective case on a periodic domain,

$$\frac{\partial f}{\partial t} + c\frac{\partial f}{\partial x} = 0, \tag{4.15}$$

the stability limit, given by Vichnevetsky [47], is in this case

$$\frac{c\triangle t}{\triangle x} \leq \frac{\sigma_i}{\omega'_m}, \tag{4.16}$$

where $\triangle x$ and $\triangle t$ are step sizes in the spatial direction and time, respectively, $[-i\sigma_i, i\sigma_i]$ is the segment of the imaginary axis in the stable region for the time advancement scheme and ω'_m the maximum value of the modified wavenumber for the first derivative approximation (Lele [46]). For the sixth-order compact scheme, σ_i is equal to π and ω'_m to 1.9894.

The case of pure diffusion on a periodic domain is also considered

$$\frac{\partial f}{\partial t} = \nu\frac{\partial^2 f}{\partial x^2}, \tag{4.17}$$

The stability limit, given by Vichnevetsky [47], is in this case

$$\frac{\nu\triangle t}{\triangle x^2} \leq \frac{\sigma_r}{\omega''_m}, \tag{4.18}$$

where $[0, i\sigma_r]$ is the segment of the real axis in the stable region for the time advancement scheme and ω''_m the maximum value of the modified wavenumber for the second derivative approximation. For the sixth-order compact scheme, the value σ_r is equal to 1 and $\omega''(k\triangle x)$ achieves its maximum value at π, i.e., ω''_m is equal to 6.857.

Finally, the stability criteria for the sixth-order scheme are of the form

$$\frac{c\triangle t}{\triangle x} \leq 1.5791 \qquad \text{and} \qquad \frac{\nu\triangle t}{\triangle x^2} \leq \frac{1}{6.857}, \tag{4.19}$$

instead of the less restrictive values of 1.7321 and 1/6, respectively, for the fourth-order compact scheme.

Chapter 5

Turbulent Eddy-Viscosity Based Models

In recent years, a large number of numerical methods have been developed for solving laminar boundary layer equations, using finite-difference procedures. However, the turbulent boundary layer remains more difficult to compute. In this work, a one-dimensional finite difference model using various turbulent eddy-viscosity models has been implemented to approximate the mean flow behavior in the wave bottom boundary layer.

5.1 One-Dimensional Boundary Layer Equation

A flow under a free stream velocity, U_∞, is considered over a flat plate aligned in the x-direction and perpendicular to the z-axis. The wall is smooth and continuous. Except in the immediate neighborhood of the surface, the velocity is of the order of U_∞. The one-dimensional x-momentum equation for the mean velocity may be derived for the wave bottom boundary layer as follows. For the boundary layer experiencing wave oscillation in the x-direction, the equation of motion is

$$\frac{\partial u}{\partial t} + u\frac{\partial u}{\partial x} + v\frac{\partial u}{\partial y} + w\frac{\partial u}{\partial z} = -\frac{1}{\rho}\frac{\partial p}{\partial x} + \nu\left(\frac{\partial^2 u}{\partial x^2} + \frac{\partial^2 u}{\partial y^2} + \frac{\partial^2 u}{\partial z^2}\right), \tag{5.1}$$

Velocity and pressure fields may be divided into horizontally averaged and fluc-

tuating parts in the usual manner, i.e., $u =< u > +u' = U + u'$, $w =< w > +w' = W + w'$, and $p =< p > +p' = P + p'$, with $V = W = 0$.

After substitution, horizontally averaging each term of (5.1), using the approximate relation

$$\frac{\partial p_\infty}{\partial x} = -\frac{\partial U_\infty}{\partial t}, \tag{5.2}$$

and applying the continuity of the fluctuations, the resulting mean x-momentum equation becomes

$$\frac{\partial U}{\partial t} + \frac{\partial}{\partial z} < u'w' >= \frac{\partial U_\infty}{\partial t} + \nu \frac{\partial^2 U}{\partial z^2}, \tag{5.3}$$

where $\dfrac{\partial}{\partial z} < u'w' >$ is the Reynolds stress.

The total stress is the sum of the laminar and turbulent stress, i.e.,

$$\tau = \tau_t + \tau_l =< u'w' > +\nu \frac{\partial U}{\partial z}, \tag{5.4}$$

and (5.3) may be written

$$\frac{\partial U}{\partial t} - \frac{\partial U_\infty}{\partial t} = \frac{\partial \tau}{\partial z}. \tag{5.5}$$

Using Prandtl's mixing length theory (Tennekes and Lumley [48]), it can be assumed that generally $\tau_t > \tau_l$ and $\tau_t = \nu_\tau \dfrac{\partial U}{\partial z}$ is an adequate approximation.

This yields the standard governing equation for the one-dimensional boundary layer

$$\frac{\partial U}{\partial t} - \frac{\partial U_\infty}{\partial t} = \frac{\partial}{\partial z}\left(\nu_\tau \frac{\partial U}{\partial z}\right). \tag{5.6}$$

Considerable efforts have been expended to estimate the optimum representation for $\nu_\tau(z, t)$.

In this domain, the boundary and initial conditions of the flow are defined as

$$U(z_0, t) = 0 \qquad \text{(no slip condition)}, \tag{5.7}$$

$$U(\infty, t) = U_\infty(t) \qquad \text{(upper boundary condition)}, \tag{5.8}$$

$$U(z, t_0) = U_0(z) \qquad \text{(initial condition)}, \tag{5.9}$$

where z_0 is the bed roughness, t_0 the initial time, and $U_0(z)$ the initial velocity. In this work, the bed is considered to be smooth, i.e., $z_0 = 0$, the initial time is set to $t_0 = 0$ and the flow generally starts from rest, i.e., $U_0(z) = 0$ m s^{-1}.

5.2 Laminar Solution

Although natural beds are never perfectly flat and natural flows tend to be turbulent, it is worthwhile studying the case of smooth laminar flow, because many of its features are present in natural flows and because its structure gives clues towards efficient methods of analyzing natural flows.

For a constant eddy viscosity, $\nu = 10^{-6}$ m^2 s^{-1}, the steady-state solution to (5.6) was derived by Stokes [7], for a free stream velocity of the form $U_\infty(t) = U_m \sin(\omega t)$. The solution is

$$U_s(z, t) = U_m \sin(\omega t) - U_m \sin(\omega t - \frac{z}{\delta_s}) \exp(-\frac{z}{\delta_s}), \tag{5.10}$$

in which $\delta_s = \sqrt{\frac{2\nu}{\omega}}$ is the thickness of the laminar boundary layer, called the Stokes length. In this solution, the first term represents the inviscid oscillation of the main flow, and the second term is the viscous effect.

If the flow starts from rest, i.e., $U_s(z, 0) = 0$, a transient solution is significant for the first wave period. This transient solution, $U_t(z, t)$, is given in Appendix B.

Steady-state, $U_s(z, t)$, and transient, $U_t(z, t) + U_s(z, t)$, velocities profiles are given for the case of a 8 second-period wave in a domain of vertical length 5 cm in Figure 5.1 to indicate the influence of the initial transients on the velocity profiles. The velocity profiles have been plotted from $z = 0$ to $z = 2$ cm, the velocities being approximately constant above this value.

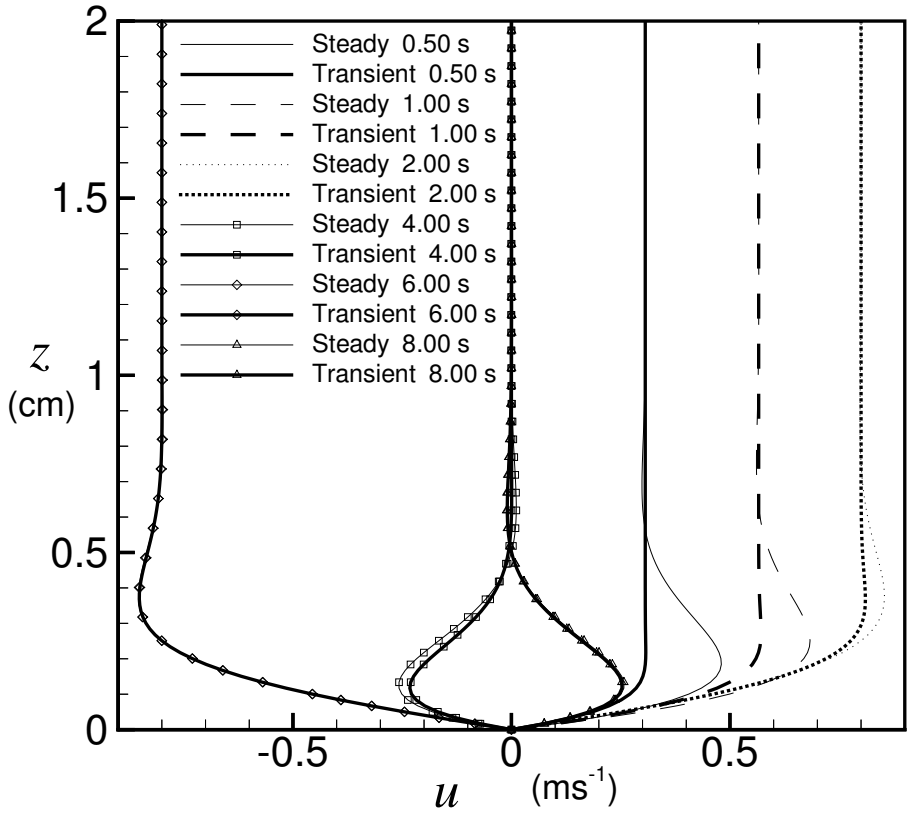

Figure 5.1: Long-time, *Steady* and combined steady-transient, *Transient*, laminar velocity profiles for a 8 second-period wave for different phases of the first wave period.

It can be noticed that the maximum amplitude of the oscillation is not at the top of the boundary layer but at an intermediate height near the wall, e.g., for $z < 0.5$ cm. This feature of the wave bottom boundary layer makes the standard definition of the boundary layer thickness, the height at which the velocity reaches 0.99 U_∞, difficult to apply. Hence, the boundary layer thickness in the three-dimensional simulations is defined using other criteria defined below. By differentiating the solution of the one-dimensional equation (5.10) with respect to time (Panton [49])

$$\frac{\partial U_s(z,t)}{\partial t} = U_m\omega\cos\omega t - U_m\omega\cos(\omega t - \frac{z}{\delta_s})\exp(-\frac{z}{\delta_s}) \tag{5.11}$$

where the first term is the pressure gradient, as shown by replacing (5.2) in (5.6), and

the second term represents the viscous effect, as shown in (5.6). The term $\cos(\omega t - \frac{z}{\delta_s})$ contains a phase lag of z/δ_s compared to the term $\cos \omega t$. At the wall, the phase lag is zero and the terms of the velocity derivatives cancel, the viscous force exactly counteracts the pressure force so that no motion occurs. Moving away from the wall, the oscillating viscous stresses decrease according to the exponential factor in (5.11). In the intermediate region, at small distance from the wall, because of the phase lag z/δ_s, $\cos(\omega t - \frac{z}{\delta_s})$ peaks at later times than $\cos \omega t$, so the fluid decelerates. However at certain distance from the wall, the lag is so great that both the pressure and viscous effects add together and an acceleration of the fluid induces higher velocities than those produced by the pressure force acting alone and produces an overshoot. This phenomenon of overshoot was originally observed by Richardson and Tyler [50].

It can be noticed that the transient part of the velocity vanishes exponentially in the z-direction. Moreover, for $t > 8.00$ s, the transient solution doesn't influence the velocity measurably. Thus, the transient part of the laminar solution vanishes after one wave period (Panton [51]).

5.3 Turbulent Eddy-Viscosity Based Models

The eddy viscosity concept, first introduced by Boussinesq more than a century ago, is a useful tool for obtaining simple turbulent flow models. The simplified equation of motion for mean flow velocity

$$\frac{\partial U}{\partial t} = \frac{\partial U_\infty}{\partial t} + \frac{\partial \tau}{\partial z}, \tag{5.12}$$

contains two unknowns, the mean velocity U and and the shear stress τ. It can be solved when the relation between these two components is known. The relationship for laminar flow is given by Newton's formula (3.1), however, for turbulent flows it is

not well described.

A number of investigators have proposed vertically varying eddy viscosity models in attempts to model the bottom boundary-layer dynamics as shown in the literature review in Chapter 2. They assumed that the turbulent eddy viscosity $\nu_\tau(z,t)$ could approximate the contributions from the Reynolds stress and the effects of turbulent diffusion of momentum, based on Prandtl's mixing length theory.

In the past, three-dimensional boundary layer models were too computationally expensive and reasonable agreement with laboratory experiments could be obtained with one-dimensional models. In this work, a one-dimensional model based on the turbulent eddy viscosity has thus been implemented. Two eddy-viscosity models have been studied, the Grant and Madsen time-independent model [5] and the Trowbridge and Madsen time-dependent model [6] such that

$$\nu_\tau(z) = \kappa z u^*_{max} \qquad \text{(Grant and Madsen [5])}, \tag{5.13}$$

$$\nu_\tau(z,t) = \kappa z u^* \qquad \text{(Trowbridge and Madsen [6])}, \tag{5.14}$$

where u* is the time-dependent shear velocity defined as $u^* = \sqrt{\frac{|\tau_w|}{\rho}}$, where $\tau_w = \mu \frac{\partial u}{\partial z}\Big|_{z=0}$, and u^*_{max} the maximum value of the shear velocity over the wave cycle.

The new tool of three-dimensional boundary-layer simulations will be used as if it were a laboratory experiment to estimate the performance of these one-dimensional models for the idealized flow conditions of the wave bottom boundary layer over a smooth plate with simplified wave oscillations. Details of the numerical implementation of the one-dimensional model are given in Appendix C.

Chapter 6

Results

Results and findings of numerical experiments conducted to study turbulent wave bottom boundary layers are discussed in the following sections.

6.1 Free-stream velocities

6.1.1 Experiments

The three-dimensional model has been used with different free-stream velocities described in Table 4.1. The first set of experiments (*Cases* 1-4) have utilized simple harmonic waves, shown in Figure 6.1 (a), with different wave amplitudes, U_m. Parameters are listed in Table 4.1, with $L^{(z)} = 5$ cm and $\nu = 10^{-6}$ m^2 s^{-1}. A second set of experiments (*Cases* 2, 5-8) has varied the wave frequency, $\omega = \frac{2\pi}{T}$, T being the wave period. This set also includes the case of a steady flow, i.e., an infinite-period wave (*Case* 8), Figure 6.1 (e). The third set of experiments (*Cases* 9-11) analyzes the transition at flow reversal, for different types of wave. These are represented in Figure 6.1, e.g., a skewed wave (*Case* 9), (b); a complex wave, sum of sine functions of different amplitudes and frequencies (*Case* 10), (c); and a wave packet, product of two sine functions of different frequencies (*Case* 11), (d). The fourth and final set of experiments (*Cases* 12-14) examines the impact of including a mean current, V_∞, in the y-direction added to a 0.60 m s^{-1} sinusoidal wave, with wave period $T = 5$ s,

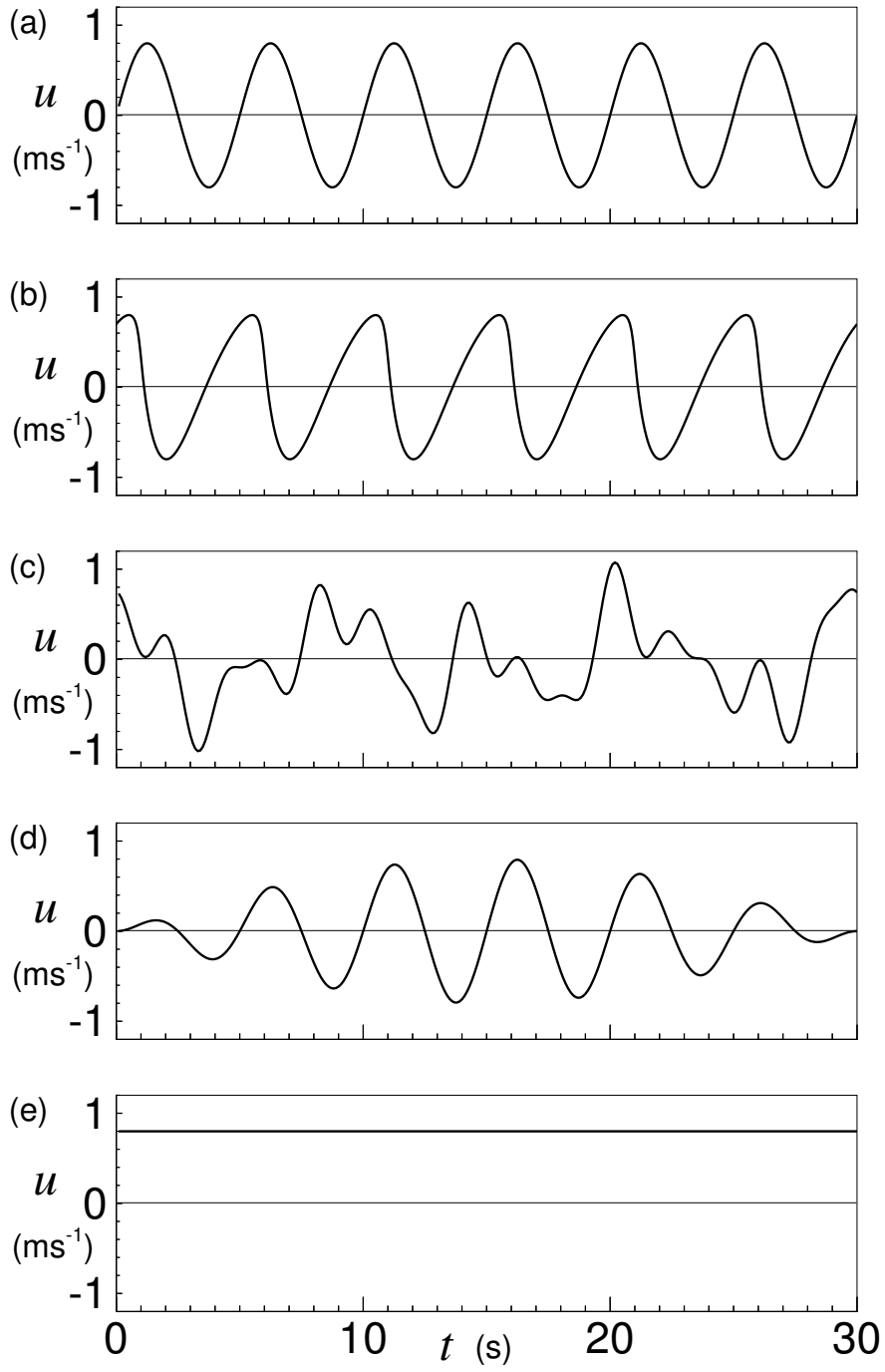

Figure 6.1: Forcing time series of free stream velocity, U_∞, for different experiments: (a) sine wave, (b) skewed wave, (c) complex wave, (d) wave packet, (e) steady flow.

propagating in the x-direction.

6.1.2 Physical Relevance

Surface wave field conditions that can produce the near-bed free-stream velocity fluctuations, U_∞, that are used in the numerical experiments are described.

Consider a periodic wave without current, with a period T and propagating in the x-direction, as shown in Figure 4.1, the dispersion relation (Dean and Dalrymple [52]) is given by

$$\omega^2 = gk \tanh(kh), \tag{6.1}$$

where g is gravity, h the water depth, ω the wave frequency and k the wavenumber, ω and k being defined as

$$\omega = \frac{2\pi}{T} \qquad \text{and} \qquad k = \frac{2\pi}{\lambda}, \tag{6.2}$$

where λ is the wavelength.

In the case of short or deep water waves, a simpler dispersion relation is obtained

$$\omega = \sqrt{gk} \qquad kh \gg 1 \qquad (\tanh(kh) \sim 1), \tag{6.3}$$

and in the case of long or shallow water waves

$$\omega = k\sqrt{gh} \qquad kh \ll 1 \qquad (\tanh(kh) \sim kh). \tag{6.4}$$

The horizontal velocity in the x-direction under the wave is given by

$$u(z) = \frac{gHk}{2\omega} \frac{\cosh k(h+z)}{\cosh(kh)} \cos(kx - \omega t), \tag{6.5}$$

where H is the wave height ($H = 2\eta$) and z is the vertical coordinate, positive upwards, defined such that $z = 0$ at the mean water depth h.

For specified conditions h, T, and u_b, where u_b is the horizontal velocity at the top of the boundary layer, that is at a distance $z = -(h - L^{(z)}) \sim -h$, the wavenumber k is determined by solving

$$u_b = \frac{gHk}{2\omega} \frac{\cosh(kL^{(z)})}{\cosh(kh)}. \tag{6.6}$$

Then the maximum velocity induced under the waves, that is for $z = 0$, is calculated with

$$u_m(z = 0) = \frac{gHk}{2\omega} = \frac{gHTk}{4\pi}. \tag{6.7}$$

The results obtained for each experiment are listed in Table 6.1. All of the experiments studied with the three-dimensional model can occur under moderate conditions in the ocean.

The wavelength, λ, and maximum wave velocity, u_m, as functions of the distance from the shore x, from $x = 200$ m to $x = 800$ m, for a water depth $h(x)$, with a 1% slope, and a boundary layer velocity $u_b = 0.8$ m s^{-1}, for different values of the wave period T are plotted in Figure 6.2.

The wave height $H = 2$ m is taken to be constant, Figure 6.2 (a). The wavelength, λ, Figure 6.2 (c), increases slowly as the water depth $h(x)$ increases. Moreover, the wavelength λ is larger when the wave period T increases which confirms the approximations in short or long water waves, i.e. $k \sim \omega$ or $\lambda \sim T$. The velocity under the waves, u_m, calculated from (6.7), decreases with x, i.e., the velocity above the boundary layer is smaller away from the shore. The wave induced current velocity is also larger as the period decreases, however, for $x < 200$ m, in shallow water for all periods, the velocity does not vary significantly as T increases.

parameters	h = 3m	h = 15 m	parameters	h = 3m	h = 15 m
T =	5 s	5 s	T =	3 s	
u_m =	0.80 m s^{-1}	0.80 m s^{-1}	u_b =	0.80 m s^{-1}	
λ =	24.93 m	38.46 m	λ =	12.68 m	
H =	1.06 m	7.33 m	H =	1.60 m	
u_m =	1.04 m s^{-1}	4.67 m s^{-1}	u_m =	1.86 m s^{-1}	
$\tanh(kh)$ =	0.64	0.99	$\tanh(kh)$ =	0.90	
T =	5 s	5 s	T =	8 s	8 s
u_b =	0.60 m s^{-1}	0.60 m s^{-1}	u_b =	0.80 m s^{-1}	0.80 m s^{-1}
λ =	24.93 m	38.46 m	λ =	42.03 m	81.79 m
H =	0.79 m	5.50 m	H =	0.94 m	2.90 m
u_m =	0.78 m s^{-1}	3.50 m s^{-1}	u_m =	0.88 m s^{-1}	1.39 m s^{-1}
$\tanh(kh)$ =	0.64	0.99	$\tanh(kh)$ =	0.42	0.82
T =	5 s	5 s	T =	12.5 s	12.5 s
u_b =	0.40 m s^{-1}	0.40 m s^{-1}	u_b =	0.80 m s^{-1}	0.80 m s^{-1}
λ =	24.93 m	38.46 m	λ =	66.94 m	141.83 m
H =	0.53 m	3.66 m	H =	0.91 m	2.27 m
u_m =	0.52 m s^{-1}	2.34 m s^{-1}	u_m =	0.83 m s^{-1}	0.98 m s^{-1}
$\tanh(kh)$ =	0.64	0.99	$\tanh(kh)$ =	0.27	0.58
T =	5 s	5 s			
u_b =	0.20 m s^{-1}	0.20 m s^{-1}			
λ =	24.93 m	38.46 m			
H =	0.26 m	1.83 m			
u_m =	0.26 m s^{-1}	1.17 m s^{-1}			
$\tanh(kh)$ =	0.64	0.99			

Table 6.1: Characteristics of the different wave flows.

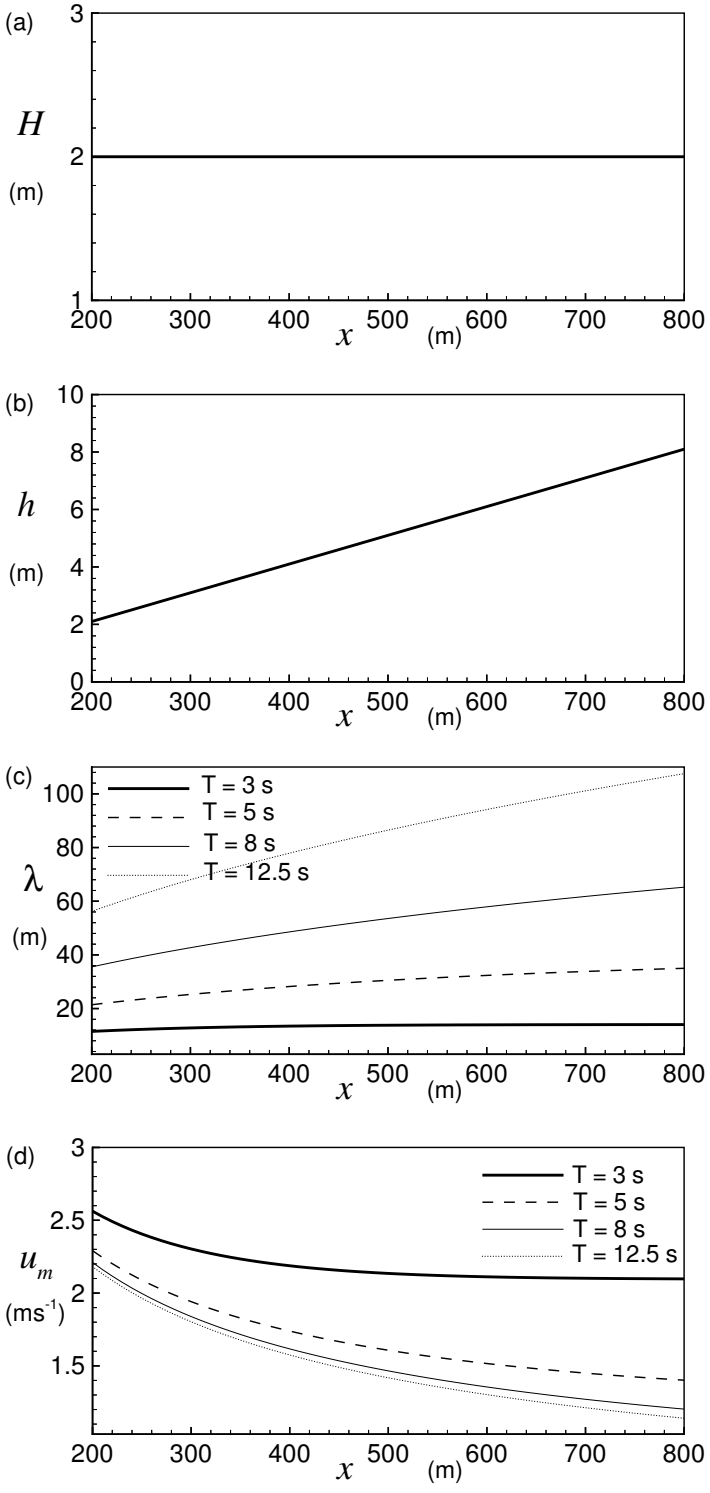

Figure 6.2: (a) Wave height, H; (b) water depth, h, with a 1% slope; (c) wave length, λ; and (d) maximum wave velocity, u_m, as a function of distance from the shore x.

6.2 Basic Flow Features

Although the water motion induced by natural waves is not simple harmonic, it is useful to study a monochromatic wave induced flow propagating in the x-direction (*Case* 1). The domain, shown in Figure 4.1, uses the following dimensions $L^{(x)} =$ 0.1 m, $L^{(y)} = 0.075$ m and $L^{(z)} = 0.05$ m and a grid resolution of 257x129x130 grid points in the x-, y- and z-directions, respectively. The flow is initialized with low-energy white noise and forced with a pressure gradient that produces a free-stream velocity with a 5-second period and a maximum amplitude of 0.80 m s^{-1}, i.e., $U_\infty(t) = 0.80\sin(\frac{2\pi}{5}t)$. The free stream velocity is plotted in Figure 6.1 (a).

6.2.1 Velocity Vectors

Side and top views of the velocity field during phases of flow deceleration and flow reversal are illustrated in Figures 6.3. For clarity, the figures do not show velocity vectors at all the grid points in each direction.

The near-wall flow is represented in Figure 6.3 (a). The flow is well-organized and approximately two-dimensional; the velocity is not strongly variable in the x-direction. The first grid point is less than 0.1 mm from the boundary and the strong shear layer at the bottom is resolved with approximately 15 grid points. Along-stream streaks of lower speed flow are seen in the top view of the velocity field in panel (b). These are often observed in laboratory experiments of boundary layers (Sarpkaya [39]) and are evident before turbulence develops in Figure 6.3 (b). It can be noted that clearly $\frac{\partial u}{\partial y} \neq 0$.

The velocity field structure shown in Figures 6.3 (c) and (d), during a turbulent event near flow reversal, is complex and disorganized. Note that the reference vector length representing velocities of 0.11 m s^{-1} is longer in the bottom panels than in

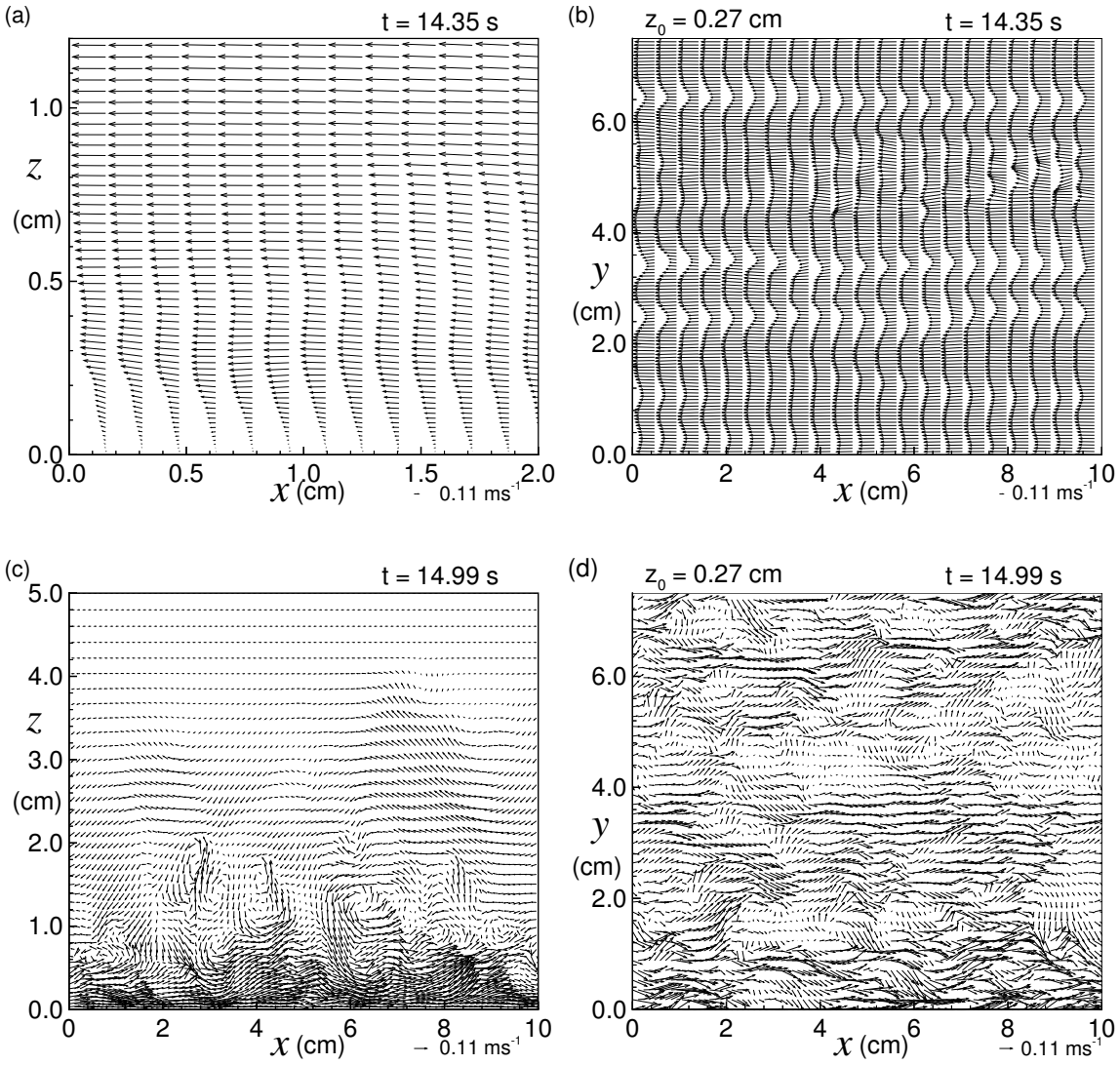

Figure 6.3: Two-dimensional cross sections of velocity vectors during flow deceleration at (a) and (b), $t = 14.35$ s, and during flow reversal at (c) and (d), $t = 14.99$ s, in side views (a) and (c), $y_0 = 3.75$ cm, and top views (b) and (d), $z_0 = 0.27$ cm.

the top panels. In Figure 6.3 (c), the velocity magnitude for $z > 4$ cm is almost zero and for $z < 1$ cm, about 0.1 m s^{-1}. The boundary layer thickness can be visually estimated to approximately $\delta_\tau = 4$ cm. The flow near the wall, illustrated in Figure 6.3 (d), is strongly three-dimensional. A rough estimate of the horizontal length scales of typical flow features is 1 cm.

6.2.2 Kinetic Energy Dissipation Rates

Kinetic energy dissipation rate contours, given by equation (4.1) in the boundary layer, are plotted for different phases of the wave period in Figure 6.4. The left panels show results on a vertical x-z plane located at $y_0 = 3.75$ cm and the right panels depict a horizontal x-y plane parallel to the wall at $z_0 = 0.30$ cm. The scale of these figures has been chosen in order to emphasize the structure of the eddies and not the intensity of the kinetic energy dissipation rate. The turbulence is episodic in nature, going through mixing phases approximately twice per wave period, which means, in this case, that every 2.5 seconds, the flow changes direction and that 1.25 seconds after flow reversal, the flow is at its maximum amplitude.

At $t = 12.44$ s, which corresponds closely to a phase of flow reversal, the turbulence achieves its maximum intensity, as shown in Figures 6.4 (a) and (b), and then decays as the flow accelerates in the opposite direction. At $t = 13.82$ s, the flow velocity is maximum and the turbulence is minimum, as plotted in Figures 6.4 (c) and (d). Figure 6.4 (c) doesn't show significant levels of turbulence and Figure 6.4 (d) illustrates some characteristic streaks in the alongstream direction in dissipation rate. Note that even though turbulence levels are decreased at this phase, the dissipation rates, near the bottom boundary and integrated over the domain, are now much stronger than at $t = 12.44$ s. Finally, at $t = 14.60$ s, before flow reversal, the flow is decelerating, destabilizing the boundary layer and developing patches of turbulence

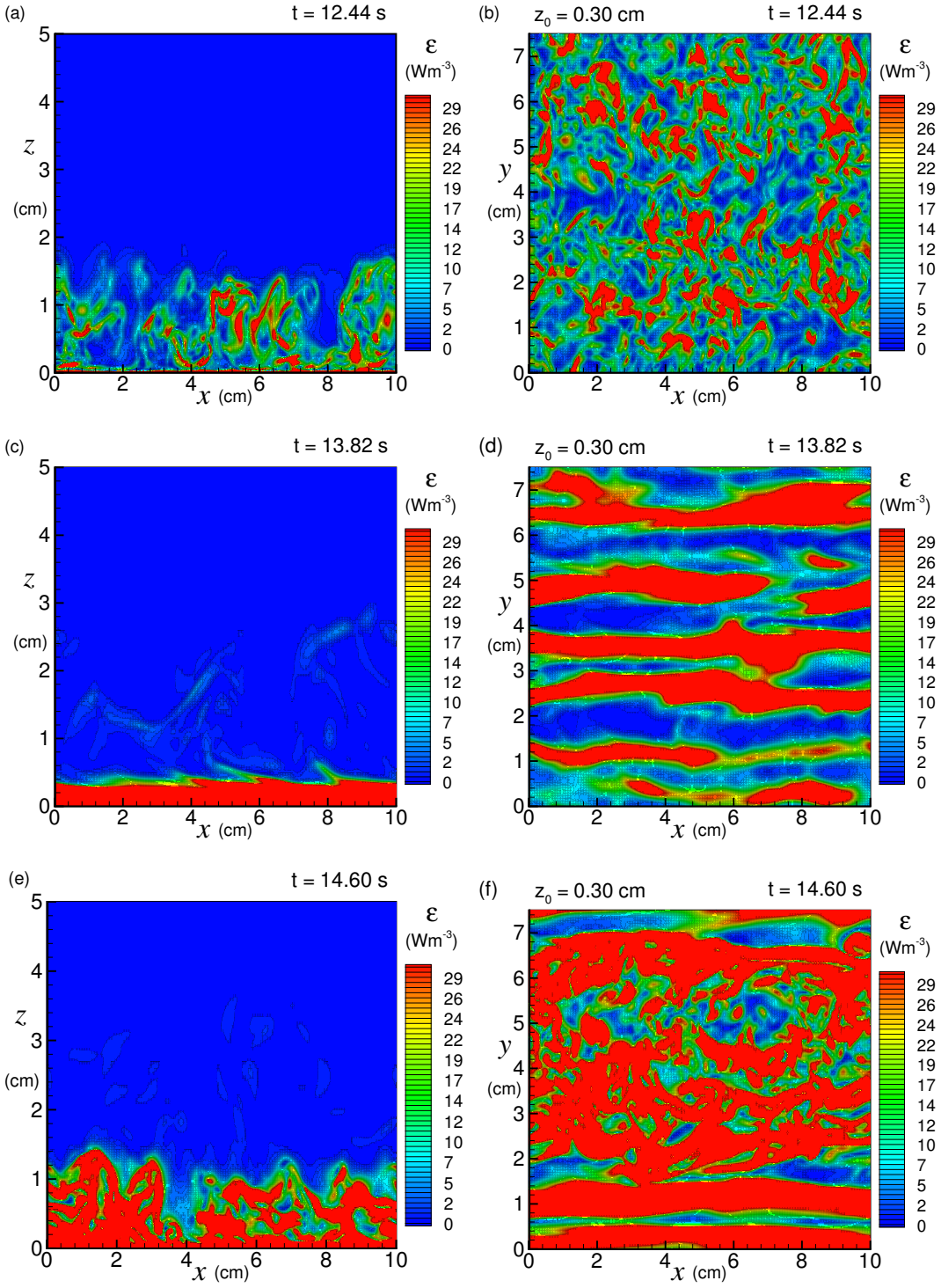

Figure 6.4: Kinetic energy dissipation rate contours in the boundary layer for Case 1 in the x-z plane at $y_0 = 3.75$ cm, side view panels (a), (c), and (e), and in the x-y plane at $z_0 = 0.30$ cm, top view panels (b), (d), and (f), at different phases of the wave cycle: (a) and (b), $t = 12.44$ s; (c) and (d), $t = 13.82$ s; (e) and (f), $t = 14.60$ s.

near the wall (Gad-El-Hak *et* al. [40]), as shown in Figures 6.4 (e) and (f). Streaks in the x-direction can still be observed in Figure 6.4 (f), with bursts of turbulence that originate near $y_0 = 4$ cm, spreading laterally and engulfing the surrounding fluid.

In this experiment, the x-z planes show variations in the boundary layer thickness, δ_τ, from approximately 0.5 cm during periods of laminar flow to 2 cm at flow reversal, as shown in Figures 6.4 (a) and (e), respectively.

It can be noted that dissipation rate contours are approximately equal to the vorticity magnitude squared $|\vec{\omega}|^2$ (Tennekes and Lumley [48]), where $\vec{\omega} = \nabla \mathrm{x} \vec{u}$ is the vorticity vector. Regions of high dissipation rate represent cores of small eddies or vortices. A visual qualitative estimate of the eddy diameters as a function of time can be made. The top-views, panels (b), (d) and (f), indicate typical eddy diameters and cross-stream coherent structure length scales in the range of 0.1-2.0 cm, depending of the wave phase.

6.2.3 Turbulent kinetic Energy

The horizontally averaged turbulent kinetic energy, as a function of height, z, and time, t, is shown in Figure 6.5 (a), where

$$\langle TKE(z,t) \rangle = \frac{1}{2} \left\langle u'^2 + v'^2 + w'^2 \right\rangle , \tag{6.8}$$

where (u', v', w') are the velocity fluctuations about the horizontally averaged flows, i.e., (4.14), components in the x-, y-, and z-directions, respectively. The turbulence is weaker during the first two wave periods of the experiment, as initial transients develop before achieving a quasi-steady behavior for $t > 10$ s. Initial transients in mean velocity profiles, growth rates of linear instabilities, and initial levels of background noise are important at early times. In general, as illustrated in Figure 6.5 (a), a quasi-steady flow response to periodic wave forcing is achieved after two or

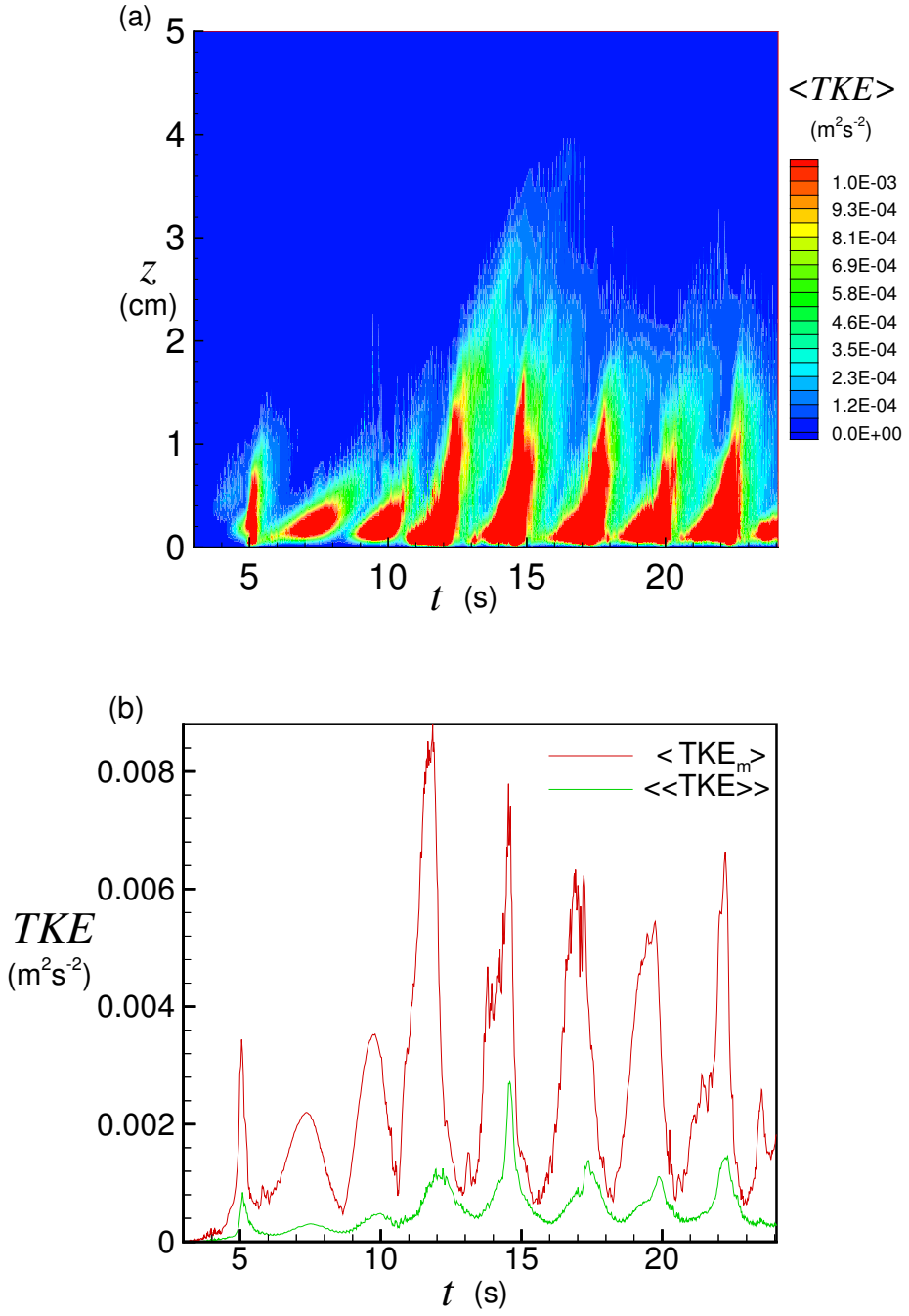

Figure 6.5: Horizontally averaged turbulent kinetic energy $\langle TKE(z,t)\rangle$ (a) for a 5 second period sine wave of maximum amplitude 0.80 m s^{-1} and volume averaged (b) $\langle\langle TKE(t)\rangle\rangle$ and local maximum horizontally averaged turbulent kinetic energy $\langle TKE_m(t)\rangle$.

three flow reversals. Then, turbulent bursts become episodic in nature, approximately twice per wave period (i.e., every 2.5 s). Turbulence initiates near the wall during phases of flow deceleration, achieves its maximum intensity and vertical excursion just after flow reversal and decays rapidly as the flow accelerates in the opposite direction (Piomelli *et* al. [41]). The decay of turbulence is seen to be more sudden than the onset of turbulence. Turbulence is strong for approximately half a wave cycle depending on the z-location. The turbulence originates very close to the boundary wall, at heights of approximately 0.1 cm, and significant turbulent kinetic energy extends to heights of approximately 2 cm, thus the turbulent boundary layer can be estimated at $\delta_\tau = 2$ cm. Contours level were selected to emphasize the time dependent structure of turbulent regions rather than the turbulence intensity.

The maximum horizontally averaged turbulent kinetic energy $\langle TKE_m \rangle$ and the volume averaged mean turbulent kinetic energy $\langle\langle TKE(t) \rangle\rangle$ as a function of time are shown in Figure 6.5 (b). The quantity $\langle\langle TKE(t) \rangle\rangle$ has been calculated over the domain $0 < z < 2$ cm, the estimate for the boundary layer thickness, δ_τ, the turbulent kinetic energy being small above this height. As shown in the figure, the mean turbulence achieves its maximum intensity just after flow reversal, with a maximal value of 0.0088 m^2 s^{-2} which occurs at a height of $z = 0.1$ cm.

For scaling purposes, estimates can be made assuming that the flow is isotropic, i.e.,

$$u' \sim v' \sim w'. \tag{6.9}$$

In this case, the turbulent kinetic energy is approximately

$$\langle\langle TKE(t) \rangle\rangle \sim \frac{3}{2} u'^2, \tag{6.10}$$

which suggests that for an horizontally averaged turbulent kinetic energy $\langle\langle TKE(t) \rangle\rangle = 0.003$ m^2 s^{-2}, the velocity fluctuations are of the order $u' = 0.04$ m s^{-1}. For the max-

imum local value of horizontally averaged turbulent kinetic energy $\langle TKE_m(t)\rangle = 0.0088$ m^2 s^{-2}, the velocity fluctuations would be approximately $u' = 0.07$ m s^{-1}. In this experiment, the maximum free-stream velocity is $U_m = 0.8$ m s^{-1} but peak levels of turbulence occur near phases before and after flow reversal when typical free-stream velocities, $U_\infty < 0.3$ m s^{-1}.

6.2.4 Kinetic Energy and Dissipation Rate Spectra

Volume averaged kinetic energy and dissipation rate spectra in the x- and y-directions at $t = 12.00$ s, i.e., at the time of maximum turbulence during the simulation, Figure 6.5 (b), are shown in Figure 6.6. This experiment was conducted with a grid resolution of 257x129x130 grid points. As the last points in the x- and y-directions are duplicate points because of periodicity, there are effectively 256x128x130 grid points which translate to 128 k_x wavenumbers in x and 64 k_y wavenumbers in y. The volume average total kinetic energy is given by

$$KE = \frac{1}{2}\langle\langle u^2 + v^2 + w^2\rangle\rangle, \tag{6.11}$$

and the x-, y-, and z-component volume average kinetic energies are labeled u^2 for $\frac{1}{2}\langle\langle u^2\rangle\rangle$, v^2 for $\frac{1}{2}\langle\langle v^2\rangle\rangle$, and w^2 for $\frac{1}{2}\langle\langle w^2\rangle\rangle$, respectively. The kinetic energy spectra and its three components u^2, v^2, and w^2, and straight lines representing $k^{-5/3}$ and k^{-3} are represented in Figure 6.6 (a) and (b) in the x- and y-directions, respectively.

These quantities are calculated using Fast Fourier Transforms of $u(x, y, z, t_0)$, $v(x, y, z, t_0)$ and $w(x, y, z, t_0)$ in the along-stream or cross-stream directions. Assuming Fourier component wave solutions for the variables u, v and w of the form $u(x) = \hat{u}(k_x)e^{ik_x x}$ in the x-direction or $u(y) = \hat{u}(k_y)e^{ik_y y}$ in the y-direction and periodicity in x with period $L^{(x)}$ and in y with period $L^{(y)}$, the fields can be expanded in truncated Fourier series with corresponding Fourier coefficients, for example in the streamwise

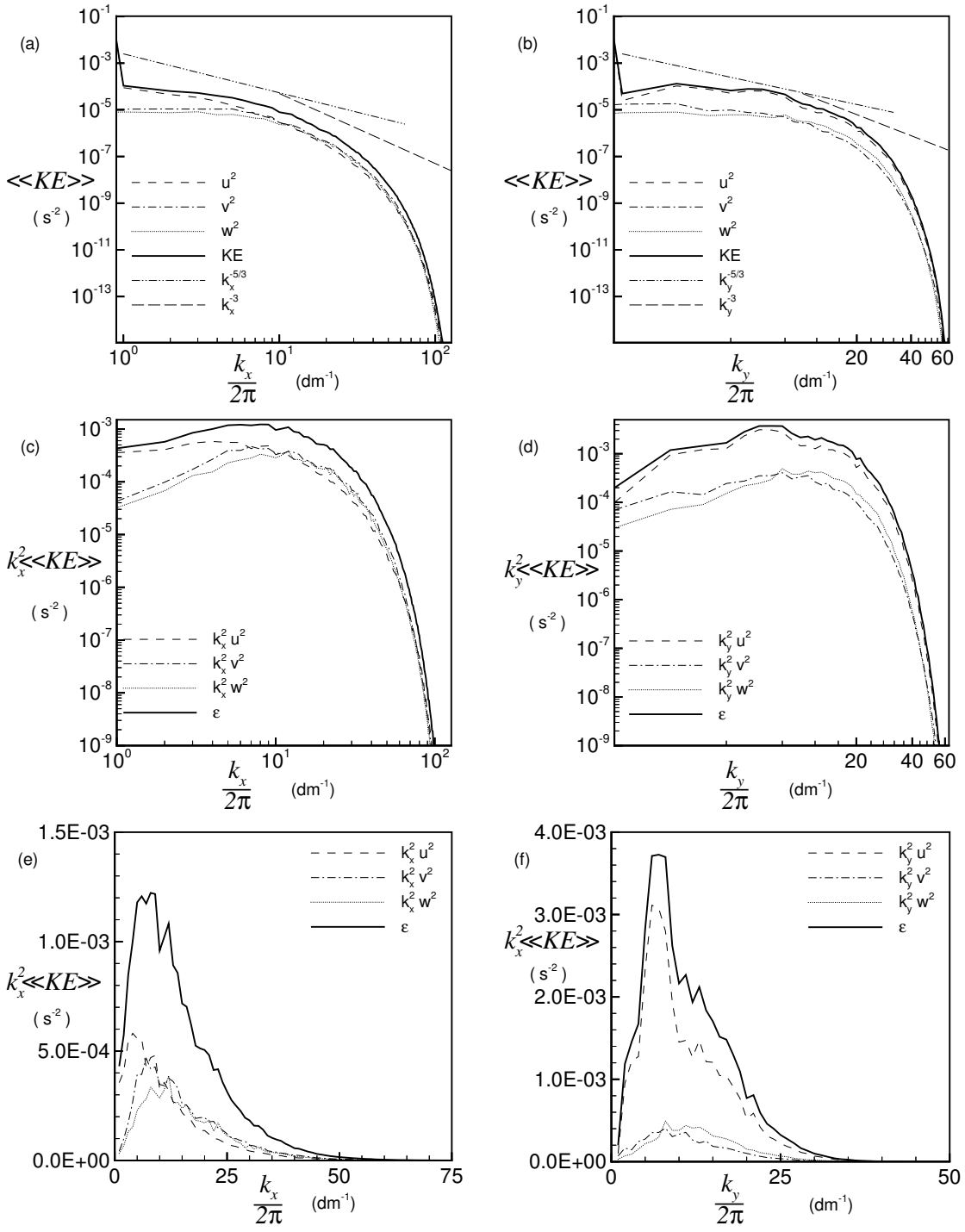

Figure 6.6: Volume averaged kinetic energy spectra decomposed in (a) the x-direction; (b) the y-direction; kinetic energy dissipation rate spectra in standard log-log form decomposed in (c) the x-direction and (d) the y-direction; and kinetic energy dissipation rate spectra in linear form decomposed in (e) the x-direction and (f) the y-direction for Case 1 at $t = 12.0$ s.

direction,

$$\hat{u}(k_x(n)) = \frac{1}{N}\sum_{i=0}^{N-1} u(x_i)e^{-ik_x(n)x_i}, \tag{6.12}$$

where $x_i = L^{(x)}i/N$, $i = 0, 1, \ldots, N\text{-}1$ and $k_x(n)$ are the wavenumbers given by $2\pi n/L^{(x)}$. The mode numbers n range from $n = 0, 1, \ldots, N\text{-}1$ where N is the total number of grid points in x, i.e., $nx\text{-}1$ (Canuto *et* al. [53]). Thus, the kinetic energy is defined as a function of the alongshore wavenumbers k_x with

$$KE(k_x) = \frac{1}{2}[\hat{u}(k_x(n))\hat{u}^*(k_x(n)) + \hat{v}(k_x(n))\hat{v}^*(k_x(n))\hat{w}(k_x(n))\hat{w}^*(k_x(n))], \tag{6.13}$$

where $\hat{u}^*$, $\hat{v}^*$, and $\hat{w}^*$ are the complex conjugates of $\hat{u}$, $\hat{v}$ and $\hat{w}$, respectively.

For $\frac{k_x}{2\pi} > 5$, the flow is approximately isotropic, i.e., $u^2 \sim v^2 \sim w^2$ as seen in Figures 6.6 (a) and (b), but for $\frac{k_x}{2\pi} < 5$, greater energy content is contained in u^2 than in v^2 or w^2. Energy levels in wavenumbers in the range $3 < \frac{k_x}{2\pi} < 20$ approximately follow the $k^{-5/3}$ slope curve, commonly associated with the inertial subrange of turbulence cascade. For higher wavenumbers, $\frac{k_x}{2\pi} > 20$, the energy content decreases rapidly. For $15 < \frac{k_x}{2\pi} < 40$, the kinetic energy curves approximately follow the k^{-3} slope, which is typical of the small scale dissipation range. The mean flow, which is represented by a wavenumber $0 + \epsilon$, ϵ being small, has significantly greater energy. Approximately, 7 orders of magnitude difference in energy content can be noticed between well-resolved scales, i.e., for $\frac{k_x}{2\pi} < 7$, and smallest resolved scales on computational mesh, e.g., $\frac{k_x}{2\pi} \sim \frac{2}{3}(128) = 86$. This difference indicates that the model is satisfactorily resolved during the turbulent bursts.

Similar results are obtained from the kinetic energy spectra decomposed in the y-direction shown in Figure 6.6 (b). At this time, the flow is not isotropic in the y-direction as u^2 is greater than v^2 or w^2. Energy contents in wavenumbers in the range $3 < \frac{k_y}{2\pi} < 12$ approximately follow the $k^{-5/3}$ slope curve, and for higher wavenumbers,

$\frac{k_y}{2\pi} > 30$, the energy content decreases rapidly. For $15 < \frac{k_y}{2\pi} < 25$, the kinetic energy curves approximate the k^{-3} slope.

Dissipation rates as a function of wavenumber can be estimated from $k_x^2 KE$ or $k_y^2 KE$ as shown, respectively, in log-log form in panels (c) and (d) or in a linear form in panels (e) and (f). Figure 6.6 (c) shows a peak in the dissipation rates decomposed in the x-direction near $\frac{k_x}{2\pi} = 10$ and a rapid decline for higher wavenumbers. The majority of dissipation occurs in the wave band $5 < \frac{k_x}{2\pi} < 20$. Wavenumbers in the range $\frac{k_x}{2\pi} > 30$ are in the far dissipation range. Figure 6.6 (e) illustrates more quantitatively the dissipation rate maxima in the range $5 < \frac{k_x}{2\pi} < 15$. For $\frac{k_x}{2\pi} > 30$, the subgrid-scale filter (Slinn and Riley [4]) has increased influence. The decomposition of the dissipation rate spectra in the y-direction in the log-log plot in Figure 6.6 (d) shows a peak in the dissipation rate and Figure 6.6 (f) gives more precisely the range of this maxima for $5 < \frac{k_x}{2\pi} < 12$.

6.2.5 Resolved and Subgrid Dissipation Rates

The volume averaged kinetic energy dissipation rates measured from the three-dimensional model at well resolved scales and from the subgrid scale filter are displayed in Figure 6.7. These are plotted to show the absolute value of the dissipation rates as a function of time; however these quantities should be negative, meaning a loss of kinetic energy from the flow. The dissipation rate is a strong function of time and maximum during phases of strong flow. Integrated over time, 93.6% of the kinetic energy dissipation occurs at well-resolved scales and 6.4% is through the subgrid scale filter. Comparison of these magnitudes shows that most of the dissipation has been satisfactorally resolved for this experiment. This experiment is one of the highest Reynolds number attempted in this study (Table 4.1) and thus represents a "worst

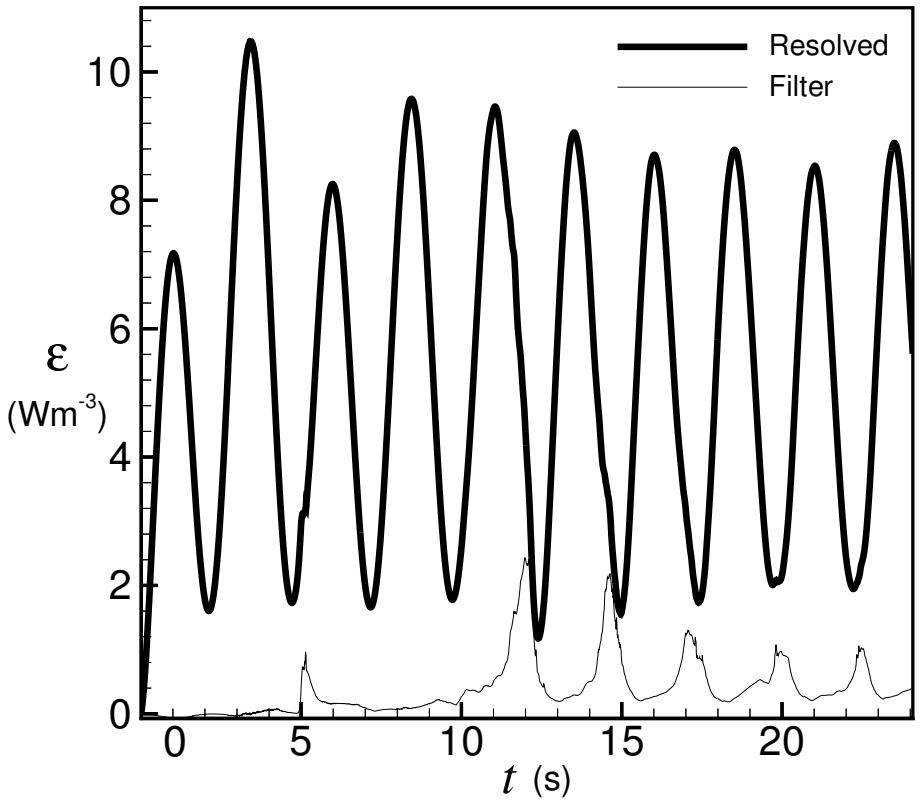

Figure 6.7: Volume averaged kinetic energy dissipation rates measured from the numerical experiments at well resolved scales (*Resolved*) and from the subgrid scale filter (*Filter*).

case" in which the subgrid scale filter makes the largest contribution to net dissipation. Thus it can be concluded that the flows are sufficiently resolved for the flow features of interest here for the experiments presented below. The maximum energy removal by filtering occurs at approximately $t = 12.0$ s and $t = 14.5$ s, when, comparing to Figure 6.5 (b), the volume averaged turbulent kinetic energy is maximum and the turbulence has generally cascaded down to smaller unresolved scales.

A common problem exists if the physical flow being simulated produces smaller energy containing eddies than can be well represented in the model. Generally, turbulence produces a cascade of energy towards smaller scales that continue down to

the Kolmogorov length-scale at which viscosity dominates inertial effects and energy dissipation is completed. According to Moin and Mahesh [54], the smallest resolved length scale is required to be of the order of η, where η is the Kolmogorov length scale defined by

$$\eta = \left(\frac{\nu^3}{\varepsilon}\right)^{1/4}, \tag{6.14}$$

where ε is the kinetic energy dissipation rate and ν the kinematic viscosity. Using the mean value for the dissipation rate, 6 W m^{-3}/1000 kg m^{-3}, the Kolmogorov length-scale becomes in this problem

$$\eta = \left(\frac{1000(10^{-6})^3}{6}\right)^{1/4} \approx 0.12 \quad \text{mm}. \tag{6.15}$$

For this case, the grid resolution is $\Delta x = 0.4$ mm, $\Delta y = 0.6$ mm, and $\Delta z = 0.1$ mm in the x-, y-, and z-direction, using the value of Δz near the wall. For the steady flow boundary layer, Spalart [55] conducted direct numerical simulations studies using a resolution of

$$\Delta x = 14.3\eta, \qquad \Delta y = 4.8\eta, \qquad \Delta z = 0.33\eta. \tag{6.16}$$

The resolution used in the three-dimensional numerical simulations in this work are

$$\Delta x = 3.3\eta, \qquad \Delta y = 5\eta, \qquad \Delta z = 0.83\eta. \tag{6.17}$$

Note additionally that during phases of strongest turbulence, $<< \varepsilon >> \approx 3$ W m^{-3}, giving a value of $\eta \approx 0.24$ mm corresponding here to grid spacing of

$$\Delta x = 0.42\eta \qquad \Delta y = 2.5\eta \qquad \Delta z = 0.42\eta. \tag{6.18}$$

The spatial resolution used in the three-dimensional model is adequate for the purposes of this work as the grid spacing is of the order of the Kolmogorov length scale and similar to that used in previous related work.

The Kolmogorov length-scale varies depending on the energy in the mean flow. In the numerical experiments of this work, it is generally somewhat smaller than the smallest eddies that can be well represented on the grid and a small net portion ($\sim$ 2-5 %) of subgrid scale energy dissipation is produced by the filter.

6.2.6 Velocity Profiles

Instantaneous velocity profiles during half a wave period are shown in Figure 6.8 (a). The profiles are not plotted over all the domain but only from $z = 0$ to $z = 1.5$ cm, the velocity being approximately constant above this height. It can be observed that the velocity near the bed changes direction before the free-stream velocity, $U_\infty(t)$, (e.g., $t = 15.01$ s and $t = 17.25$ s). Moreover, a phenomenon of "overshoot" often occurs near the boundary (e.g., $t = 16.25$ s); that is, there are elevations where the velocity amplitude exceeds the amplitude of the flow over the boundary layer, $U_m = 0.80$ m s^{-1}. The velocity overshoot occurs because the velocity defect, $U_\infty(t) - u(z,t)$, has the nature of a damped wave, which alternately adds to and subtracts from the free stream velocity, $U_\infty(t)$, at different heights. These two features are typical of oscillatory boundary layers. It can be verified that the flow is maximum at $t = 16.25$ s and that the perturbations in the x- and y-directions diminish at approximately a distance of 1.5 cm from the wall, indicating that this portion of the domain contains most of the boundary layer turbulence.

The instantaneous velocity profiles are also shown in a log z-axis plot in Figure 6.8 (b). Here, the velocity is plotted for $0 < z < L^{(z)}$. It can be noticed that the velocity distribution does not follow a logarithmic profile near the wall.

The horizontally averaged mean velocity profiles at the same times are shown in Figure 6.8 (c). The fluctuations in the velocity, seen in the instantaneous profiles, are eliminated by horizontally averaging the velocity. These are the types of mean

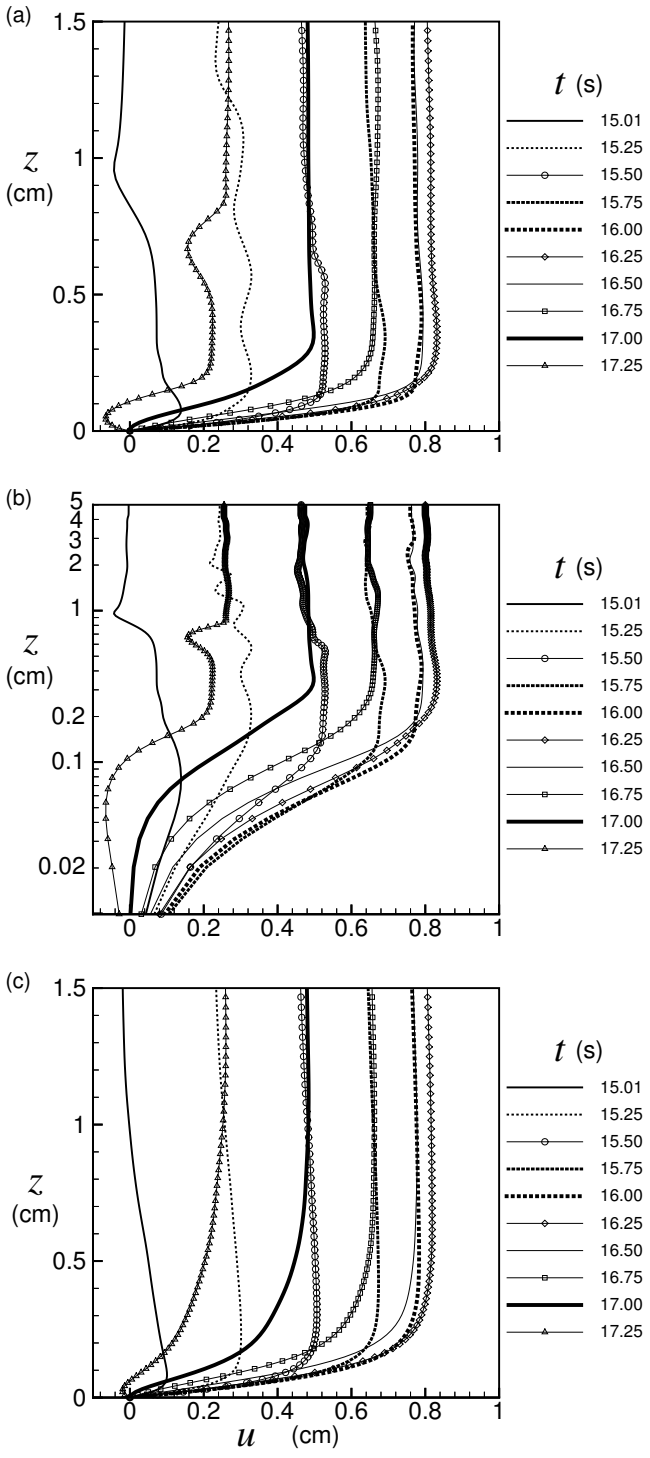

Figure 6.8: Instantaneous velocity profiles (a) for the 5 second period wave in the near wall region; and (b) on a log plot; and (c) mean velocity profiles at different times during half a wave period.

velocity profiles used below to evaluate the one-dimensional wave bottom boundary layer models.

6.2.7 One-Dimensional Model Comparisons

Results obtained with the Grant and Madsen ($G\&M$) and Trowbridge and Madsen ($T\&M$) eddy viscosity models are shown for different phases of flow, (a) at flow reversal, (b) during flow acceleration, (c) at maximum flow, and (d) during flow deceleration in Figure 6.9. These results are compared with those obtained with the solution for a constant viscosity ($Laminar$) and from the three-dimensional model ($3D$).

At flow reversal, Figure 6.9 (a), the different plots do not seem to match precisely at the top, this is due to the difficulty to get output at the exact same time from all the models but is considered negligible. The results show that for a sinusoidal free-stream, all the models give approximately the same shape of velocity profiles, however, the models seem to be more similar in the case of accelerating flow, panel (b), or maximum flow, panel (c), than near flow reversal, panel (a). Thus, accuracy of the one-dimensional models depends on the phase of the wave period, the best performance being near maximum flow and the largest differences between the three-dimensional model and the others being near flow reversal. The performance of these models varies also as a function of the distance from the boundary z. Generally, the Grant and Madsen and Trowbridge and Madsen type models overpredict the boundary layer thickness, δ_τ, and underpredict the shear near the wall, $\left.\frac{\partial u}{\partial z}\right|_w$. These models are based on the assumption of strongly turbulent flows, which are not always present in the three-dimensional model. For example, because of flow acceleration, the turbulent levels in this experiment decrease periodically as shown in Figures 6.4 and 6.5 and the assumptions of the one-dimensional models should

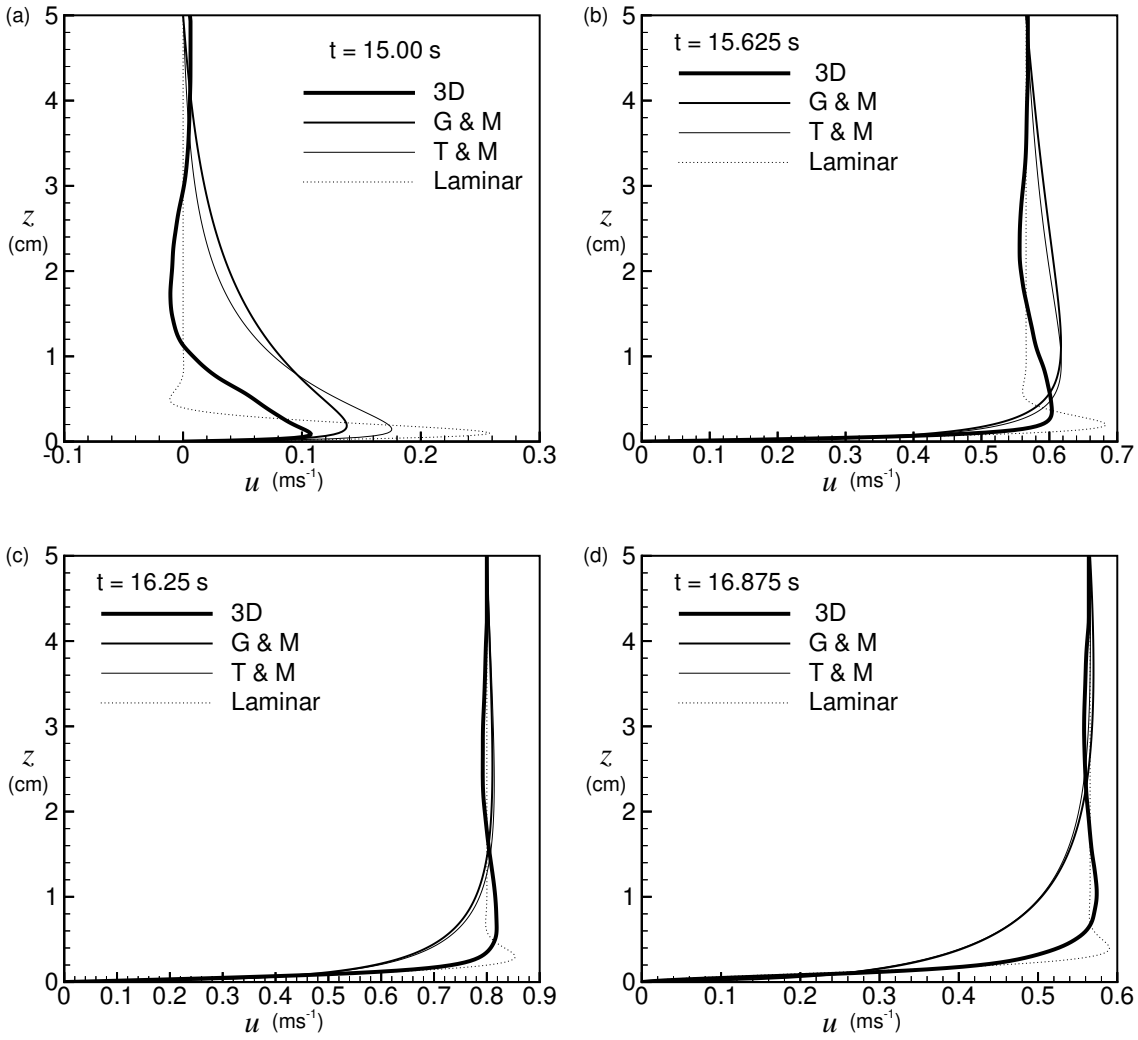

Figure 6.9: Comparisons of mean velocity profiles from the 3-dimensional model (3D), Grant and Madsen model (G & M), Trowbridge and Madsen model (T & M), and laminar model (Laminar) at different phases of the wave period for the 5 second period wave, at (a) t = 15.00 s, (b) t = 15.625 s, (c) t = 16.25 s, and (d) t = 16.875 s.

not be expected to apply. At these times, as shown in Figure 6.9 (d), the laminar solution more closely resembles the three-dimensional boundary-layer model profiles. The flow during phases of maximum flow is considered to be quasi-laminar, and the laminar solution is better than the one-dimensional models, as shown in Figure 6.9 (c). As predicted by Madsen (personal communication), the Grant and Madsen [5] and Trowbridge and Madsen [6] models do not significantly differ from one another for smooth boundaries under a simple monochromatic wave oscillation. Quantification of the accuracy of the one-dimensional models for different conditions are given below.

6.2.8 Particle Motions

Lagrangian particle x-z locations at the onset of turbulence are shown for a 12.5 second-period wave at $t = 6.2$ s in Figure 6.10 (*Case* 7). Tens of thousands of particles are released in the three-dimensional flows in a rectangular lattice before transition in the near-wall region. The locations of these particles are integrated forward in time as advected by the local fluid motions, e.g,

$$\frac{\partial \vec{X}_p}{\partial t} = \vec{u}_p \tag{6.19}$$

where the fluid velocities $\vec{u}_p(x(t), y(t), z(t), t)$ at the particle location $\vec{X}_p(x(t), y(t), z(t), t)$ are calculated using tri-linear interpolation. As time progresses, particles are distributed throughout the domain. Particles released in a region of linear wave dynamics return to their initial locations after one wave period. Deviations from this pattern are a characteristic of nonlinearity and turbulence. Figure 6.10 shows the x-z projection of particle locations near flow reversal. Some bursts of particles can be observed as the particles are entrained by the eddies generated by instabilities near flow reversal. When the flow transitions to turbulence, particles are diffused

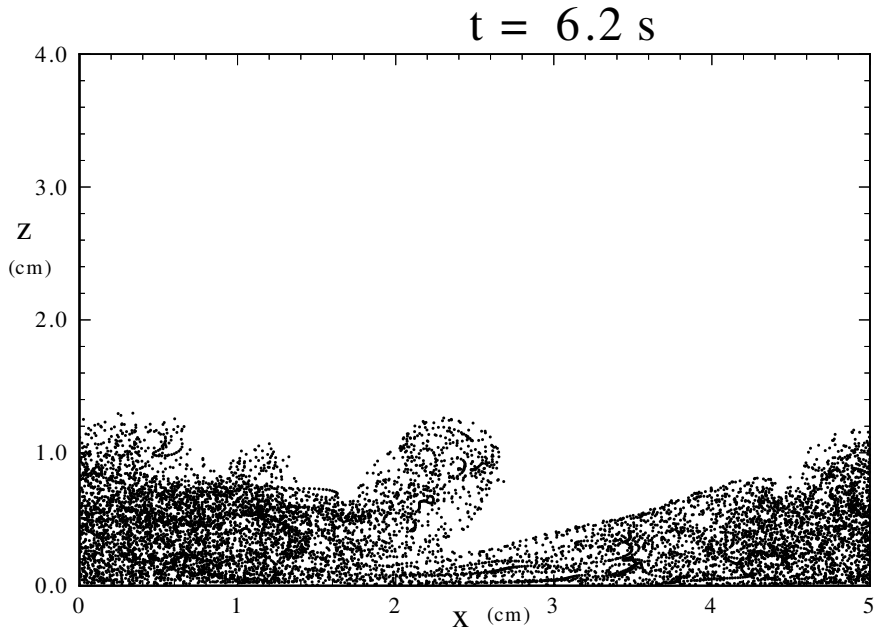

Figure 6.10: Side view of the x- and z-locations of instantaneous particles at the onset of turbulence for Case 7, T = 12.5 s, at $t = 6.2$ s.

away from the boundary and their time dependent locations are used to visualize the flow development and mass transfer across the boundary layer and to calculate the turbulent vertical mass diffusion coefficient.

6.2.9 Vertical Diffusion Coefficient

The vertical diffusion coefficient D_{z_0} in the boundary layer averaged over two time intervals, 5 s$< t <$ 15 s and 14 s $< t <$ 17 s is plotted in Figure 6.11. This coefficient is determined from the mean vertical displacement (Tennekes and Lumley [48]) using

$$D_z(z) = \frac{1}{2}\frac{\partial}{\partial t}\left\langle (z - z_0)^2 \right\rangle \tag{6.20}$$

where $\langle (z - z_0)^2 \rangle$ is the mean square vertical particle displacement averaged over a set of particles located in small vertical bins each with their own initial location, z_0,

at any time t. The strongest diffusion occurs near 0.7 cm, i.e., for particles passing

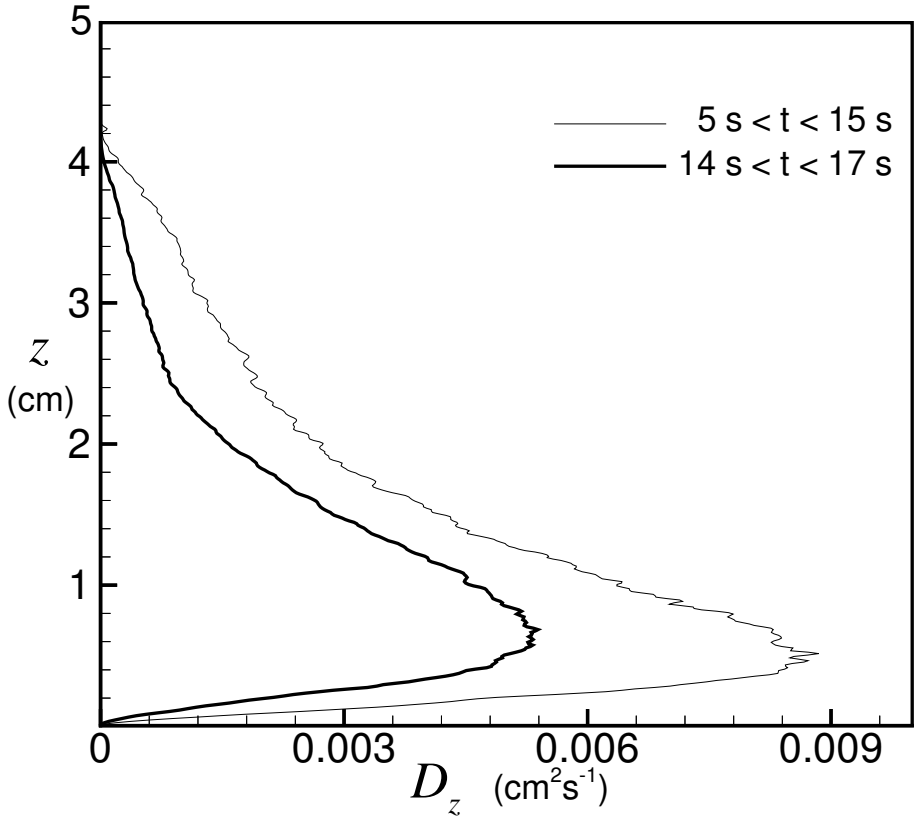

Figure 6.11: Vertical diffusion coefficients determined from particle motion in the boundary layer averaged over two different time intervals, 5 s $< t <$ 15 s and 14 s $< t <$ 17 s.

through the region located at a distance of approximately 0.7 cm from the wall. The magnitude of the vertical diffusion coefficient depends on the time interval, e.g., for a time average over 9.9 s $< t <$ 10.1 s, right at flow reversal, the magnitude of D_z would have been much larger. For this experiment, it can be concluded that the turbulent eddy viscosity is a function of time and that this quantity is more closely approximated by a quadratic function in z than a linear one. The vertical diffusion coefficient for mass is not the same as the diffusivity of momentum, ν_τ, and can differ from it by orders of magnitude (e.g., Schmidt number of salt water $\sim$ 700). For example, the

laminar diffusivity of momentum is 0.01 cm^2 s^1 but for salt water, the diffusivity of mass is 700 times smaller that the diffusivity of momentum. Nevertheless, it can be argued that the vertical profiles of turbulent diffusivities between mass and momentum should have similar structure, while differing significantly only in term of magnitude. It is noted that Fredsoe and Dieggard [56] suggest a diffusivity of momentum of the form $\nu_\tau(z) = \kappa z(1 - \frac{z}{\delta})\overline{u^*}$, which has similar vertical structure to the turbulent diffusivity calculated from this numerical experiment.

From Figures 6.10 and 6.11, it can be assumed that there is a significant net vertical transport of fluid across the boundary layer during the simulations.

6.2.10 Kinetic Energy Dissipation Approximations

This work is being done in connection with related field measurements of the wave bottom boundary layer. The field data can only provide information on boundary layer velocities on a single vertical profile, i.e., $u(z,t)$, $v(z,t)$, and $w(z,t)$. A major question is whether the field data can be used in a manner to make reasonable approximations to the dissipation rates in the boundary layer. This issue is addressed in the following manner.

The volume averaged kinetic energy dissipation rates obtained from the numerical model are compared with an estimate made from instantaneous data from a single vertical line of velocity measurements within the model, assuming homogeneous isotropic turbulence. Results are compared from the approximate method, the full three-dimensional simulations of *Case* 1 and for laminar flow in Figure 6.12. The three-dimensional volume averaged dissipation rate ($3D$) is given by

$$\varepsilon_{3D}(t) = \nu\Big\langle\Big\langle 2\Big(\frac{\partial u}{\partial x}\Big)^2 + 2\Big(\frac{\partial v}{\partial y}\Big)^2 + 2\Big(\frac{\partial w}{\partial z}\Big)^2 + \Big(\frac{\partial v}{\partial x} + \frac{\partial u}{\partial y}\Big)^2 +$$

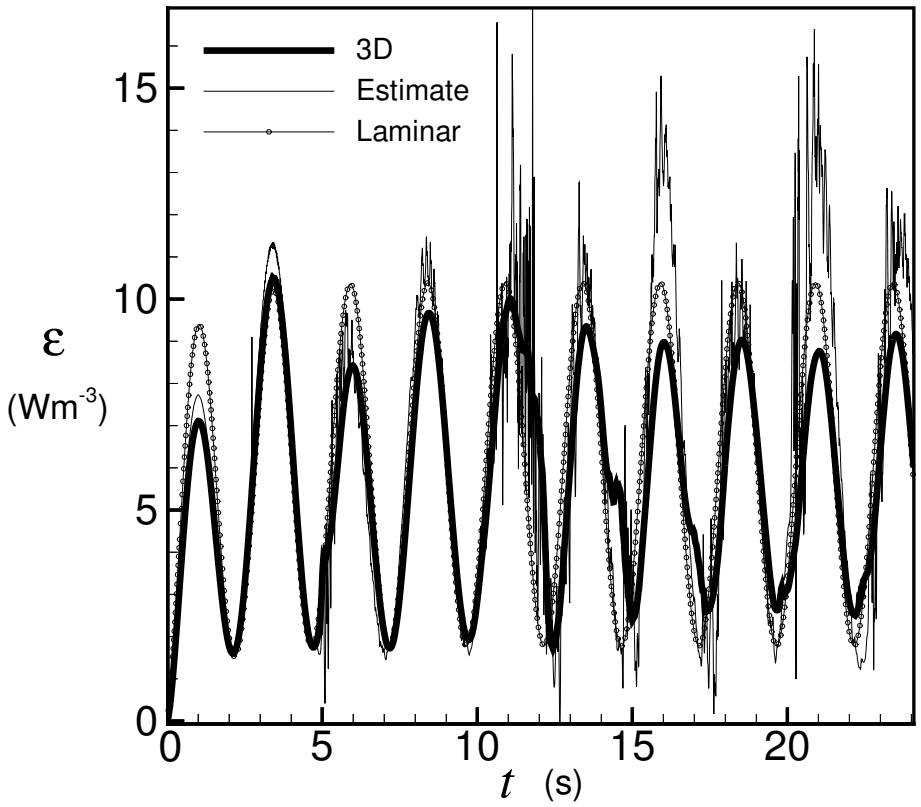

Figure 6.12: Volume averaged total kinetic energy dissipation rates measured from the (3D) numerical experiments compared with the estimate from instantaneous data from a single vertical line of velocity measurements within the model and for laminar flow.

$$\big(\frac{\partial w}{\partial y}+\frac{\partial v}{\partial z}\big)^2+\big(\frac{\partial u}{\partial z}+\frac{\partial w}{\partial z}\big)^2\big\rangle\big\rangle. \tag{6.21}$$

One approach to estimate unknowns terms in the dissipation rate ε is to use relations from homogeneous turbulence (Hinze [57]) even though the boundary layer is recognized to be neither homogeneous nor isotropic, e.g.,

$$\begin{aligned}
\Big\langle\Big\langle\big(\frac{\partial u}{\partial x}\big)^2\Big\rangle\Big\rangle &\approx \Big\langle\Big\langle\big(\frac{\partial v}{\partial y}\big)^2\Big\rangle\Big\rangle \approx \Big\langle\Big\langle\big(\frac{\partial w}{\partial z}\big)^2\Big\rangle\Big\rangle,\\
\Big\langle\Big\langle\big(\frac{\partial u}{\partial y}\big)^2\Big\rangle\Big\rangle &\approx \Big\langle\Big\langle\big(\frac{\partial u}{\partial z}\big)^2\Big\rangle\Big\rangle \approx \Big\langle\Big\langle\big(\frac{\partial v}{\partial x}\big)^2\Big\rangle\Big\rangle\ldots,\\
\Big\langle\Big\langle\big(\frac{\partial u}{\partial x}\frac{\partial v}{\partial x}\big)^2\Big\rangle\Big\rangle &\approx \Big\langle\Big\langle\big(\frac{\partial u}{\partial z}\frac{\partial w}{\partial x}\big)^2\Big\rangle\Big\rangle \approx \Big\langle\Big\langle\big(\frac{\partial v}{\partial z}\frac{\partial u}{\partial z}\big)^2\Big\rangle\Big\rangle.
\end{aligned} \tag{6.22}$$

These relations lead to an approximation of the kinetic energy dissipation rate, $\varepsilon_{Estimate}$, in terms of quantities that can be determined from the one-dimensional data

$$\varepsilon_{Estimate}(t) = \nu \left\langle \left\langle 6\left(\frac{\partial w}{\partial z}\right)^2 + 6\left(\frac{\partial u}{\partial z}\frac{\partial v}{\partial z}\right)^2 + 5\left(\frac{\partial v}{\partial z}\right)^2 + \left(\frac{\partial u}{\partial z}\right)^2 \right\rangle \right\rangle , \tag{6.23}$$

The laminar kinetic energy dissipation rate, $\varepsilon_{Laminar}$, is given by

$$\varepsilon_{Laminar}(t) = \nu \left\langle \left\langle \left(\frac{\partial u}{\partial z}\right)^2 \right\rangle \right\rangle . \tag{6.24}$$

The laminar curve has been calculated using the transient velocity obtained in Appendix B using the one-dimensional model with a constant viscosity. All the curves present a transient part for $t < 5$ s, which confirms the initial transient observed in Figure 6.5 (a).

Both approximations give reasonably accurate results for this experiment. The turbulent dissipation rates are similar to laminar dissipation rates, despite the fact that the flow exhibits other strong evidences of turbulence as shown in Figures 6.4 and 6.5 (a). In fact, dissipation rates are strongest when flow is near maximum values, that is, when the turbulence is suppressed by flow acceleration and the flow is quasi-laminar. This is because the term $\left\langle \left\langle \left(\frac{\partial u}{\partial z}\right)^2 \right\rangle \right\rangle$ is significantly larger than other terms in the dissipation rate. Most of the contribution to $\left\langle \left\langle \left(\frac{\partial u}{\partial z}\right)^2 \right\rangle \right\rangle$ occurs in the viscous sub-layer, in the near-wall region where turbulence is suppressed. Turbulent and laminar dissipation rates differ most during periods of flow deceleration and flow reversal. The one-dimensional estimate, $\varepsilon_{Estimate}$, is also similar in magnitude, however, significant noise appears in the signal. The estimated dissipation rate makes overestimates during some periods of maximum flow with better performance during the other three phases of flow. Integrated over $0 < t < 25$ s, the three methods give average values of $\varepsilon_{3D} = 5.72$, $\varepsilon_{Estimate} = 6.3$, and $\varepsilon_{Laminar} = 5.5$. In the case

of laminar flow, $\left\langle \left\langle \left(\frac{\partial u}{\partial z}\right)^2 \right\rangle \right\rangle$ would be higher than in the case of turbulent flow as observed in the velocity profiles shown in Figure 6.8 (a), at $t = 16.25$ s, at maximum flow, when the flow is considered to be laminar, and $t = 15.01$ s, at flow reversal.

6.2.11 Wall Shear

The wall shear component $\frac{\partial u}{\partial z}\big|_w$ in the x-y plane is given for two phases of the flow, near maximum flow in Figure 6.13 (a) and near flow reversal in Figure 6.13 (b). These figures suggest the spatial variability of the wall shear stress given by $\vec{\tau}_w = \mu \frac{\partial u}{\partial z}\big|_w \hat{i} + \mu \frac{\partial v}{\partial z}\big|_w \hat{j}$. This parameter is important to ocean problems because sediment suspension and movement are dependent on τ_w. Figure 6.13 (a) illustrates two-dimensional along-stream streaks, as observed in the velocity field in Figure 6.3 or dissipation rate in Figure 6.4. The wall shear component $\frac{\partial u}{\partial z}\big|_w$ in Figure 6.13 (a), varies by approximately a factor of 2 and is not homogeneous in y during periods of maximum flow. Spatial variation is even larger near flow reversal as shown in Figure 6.13 (b). Here, randomly distributed three-dimensional coherent structures, features of a turbulent event, are observed with characteristic length scales of approximately 0.5-1 cm, similar to the eddy sizes observed in Figure 6.4. Panel (b) is during a phase of transitioning flow as the turbulence spreads across the boundary layer in y and has not yet engulfed the fluid in the region $2 < y < 4$ cm.

In a laminar flow with a free stream velocity of the form $U_\infty(t) = U_m \sin(\omega t)$, the bed shear stress is given by

$$\begin{aligned} \frac{\tau_w}{\rho} &= \nu \frac{\partial u}{\partial z}\big|_{z=0} \\ &= \frac{\nu U_m}{\delta}[\sin(\omega t) + \cos(\omega t)] \\ &= \frac{\nu U_m}{\delta} \sin(\omega t + \pi/4), \end{aligned} \tag{6.25}$$

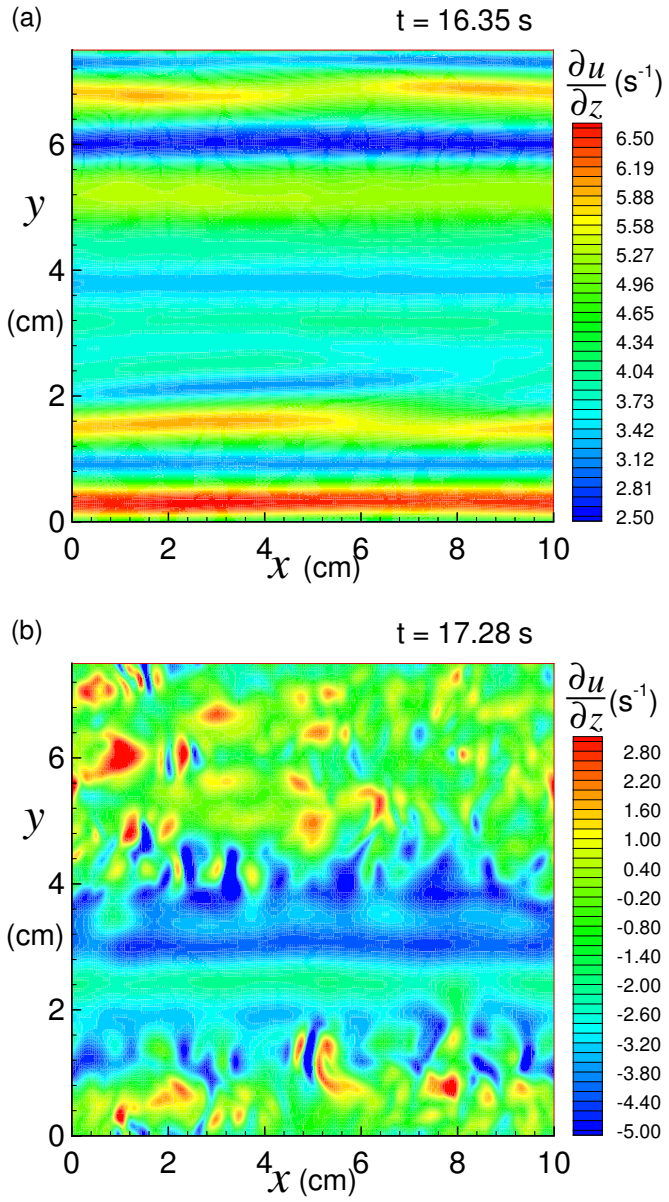

Figure 6.13: Wall shear component $\left.\frac{\partial u}{\partial z}\right|_w$ in an $x-y$ plane for Case 1, T = 5 s, near maximum flow at (a) $t = 16.35$ s, and near flow reversal at (b) $t = 17.28$ s.

From this equation, it can be noticed that there is a phase lag of 45° between the shear stress τ_w and the outer velocity $U_\infty(t)$. This phase difference is introduced because a barotropic adverse pressure gradient (constant with depth) can more easily turn that part of the flow which is located close to the bed in the boundary layer, since the flow has lower inertia in this region (Fredsoe and Deiggard [56]). In the turbulent case, the near-wall velocities are generally slower than in the laminar case (6.8 (a)) and the boundary layer is thicker, because of the vertical exchange of momentum by the eddies. For this reason, the phase shift between the bed shear stress τ_w and the free stream velocity $U_\infty(t)$ should not be as large in the turbulent case.

A plot of the wall shear stress and the absolute value of free stream velocity is given in Figure 6.14 in order to quantify the turbulent phase shift. By calculating maximum time-lagged cross correlations

$$R_{\tau_w U_\infty} = \frac{\langle \tau_w(t) \rangle \langle U_\infty(t-\phi) \rangle}{\sigma_{\tau_w} \sigma_{U_\infty}}, \tag{6.26}$$

the wall shear stress τ_w has been found to be ahead of the free stream velocity $U_\infty(t)$ by approximately 30°. This phase shift is comparable to values previously reported in the literature (Jonsson [9]) from laboratory measurements.

6.3 Reynolds Numbers Dependence

The model has been forced by simple harmonic free stream velocities of different wave amplitudes U_m or Reynolds numbers based on the wave amplitude $Re = \frac{U_m L^{(z)}}{\nu}$. The characteristics of these experiments are given in Table 4.1, as *Cases* 1-4.

6.3.1 Turbulent Kinetic Energy for Different Reynolds Numbers

The horizontally averaged turbulent kinetic energy for different amplitudes of forcing velocity, U_m = 0.60 m s^{-1} (*Case* 2), 0.40 m s^{-1} (*Case* 3) and 0.20 m s^{-1} (*Case* 4)

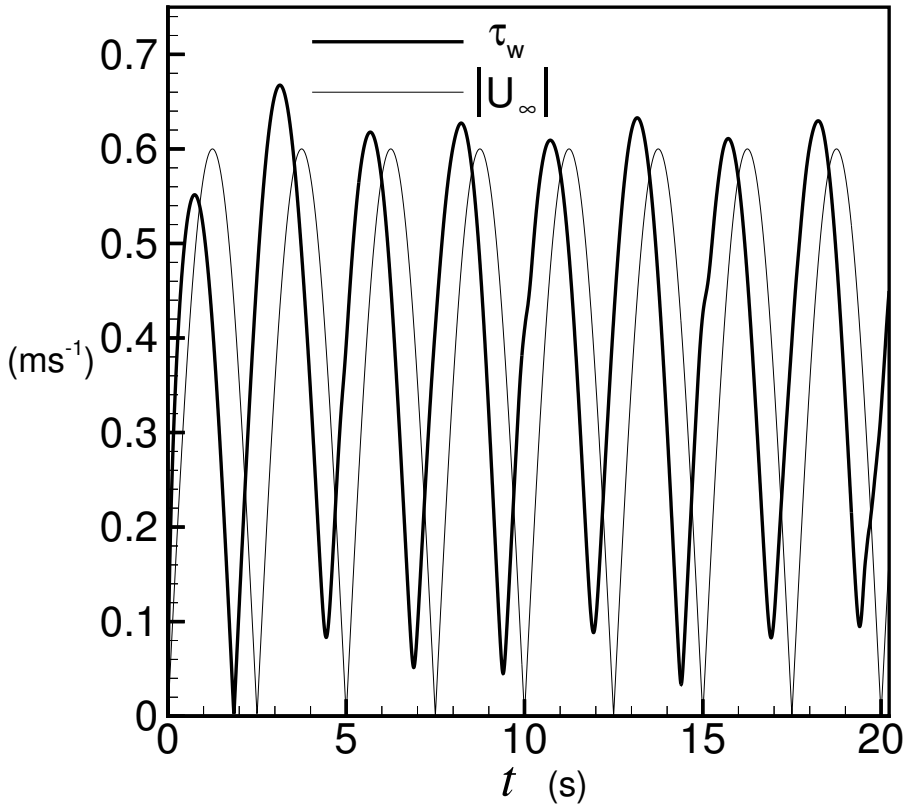

Figure 6.14: Comparison of the wall shear component $\tau_w = \frac{\partial u}{\partial z}|_w$ and absolute value of the free stream velocity $|U_\infty|$ as a function of time.

are shown in Figure 6.15 (a), (b), and (c), respectively, and can be compared with the 0.80 m s^{-1} sine wave (*Case* 1), shown in Figure 6.5 (a). The comparison of the intensity of these quantities shows that as the wave amplitude, U_m, decreases (i.e., Reynolds number decreases), the turbulent kinetic energy decreases. The strength of the turbulent kinetic energy and the turbulent boundary layer thickness, estimated to $\delta_\tau = 1$ cm, in Figure 6.15 (a) are qualitatively similar to Figure 6.5 (a). Figures 6.15 (b) and (c), which have lower scales in contour legend by approximately three orders of magnitude than Figures 6.5 (a) and 6.15 (a), do not develop bursts of turbulence. The weak fluctuations seen in panels (b) and (c) for $t < 5$ s are likely due to temporary amplification of the small perturbations (white noise) introduced in the beginning of

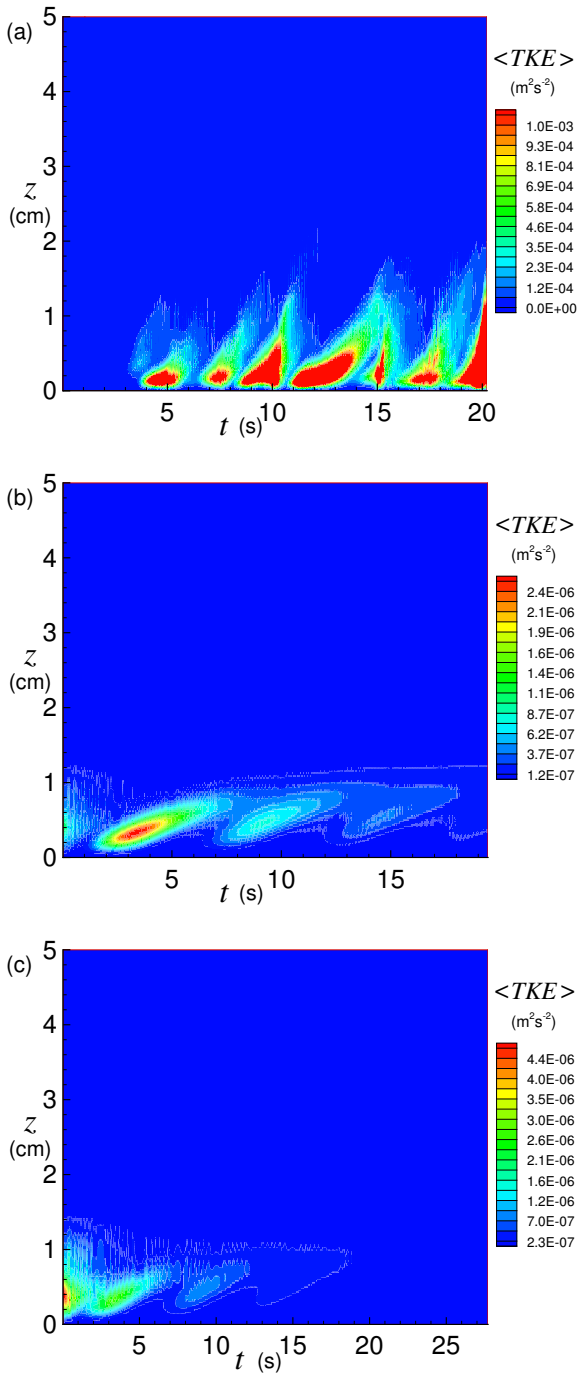

Figure 6.15: Horizontally averaged turbulent kinetic energy $\langle TKE(z,t)\rangle$ for (a) Case 2, $U_m = 0.6$ m s^{-1}; (b) Case 3, $U_m = 0.4$ m s^{-1}; and (c) Case 4, $U_m = 0.2$ m s^{-1}; compare also to Figure 6 for Case 1, $U_m = 0.8$ m s^{-1}; note change of scale in contour legend for each panel.

each run and which can grow and organize when linear instabilities are present in the velocity profiles. These fluctuations eventually decay and vanish after a few wave periods. Comparing the values of the frequency Reynolds numbers of these different cases, given in Table 4.1, to the transitional frequency Reynolds number given in the literature, $Re_{\omega trans} = 100,000$ (Jonsson [9]), it can be concluded that *Case* 1 and *Case* 2, in which $Re_\omega = 510,000$ and $Re_\omega = 290,000$, respectively, should be turbulent as their frequency Reynolds numbers are larger than $Re_{\omega trans}$. *Case* 3 can be considered in the transitional range as its Reynolds number $Re_\omega = 130,000$ is close to $Re_{\omega trans}$ and *Case* 4 is expected to be, and remains laminar with $Re_\omega = 32,000$. The laminar to turbulent transition occurs, in the model, for $Re = \frac{U_m L^{(z)}}{\nu} \approx 25,000$.

Cases 1-4 have $T = 5$ s, with different U_m. The magnitude of the acceleration of the wave forcing, $a = \frac{\partial U_\infty(t)}{\partial t}$, is plotted in Figure 6.16. Obviously, in these cases, the magnitude of the deceleration increases as the wave amplitude increases. It has been shown (e.g., Gad-El-Hak [40], piomelli *et* al. [41]) that the magnitude of the acceleration and deceleration are important parameters in the response of turbulence in a boundary layer. When the deceleration is weak or acceleration is strong, turbulence production is inhibited. These results suggest that for this wave frequency, decelerations less than 0.5 m s^{-1} are insufficient to overcome viscous damping of inflectional shear instabilities present near the wall during phases of deceleration and flow reversal.

6.3.2 Volume Mean Square Shear for Different Reynolds Numbers

The volume mean square shear for the x-component of velocity, u, for *Cases* 1-4 are displayed as a function of time in Figures 6.17 (a), (b), and (c). Comparing the

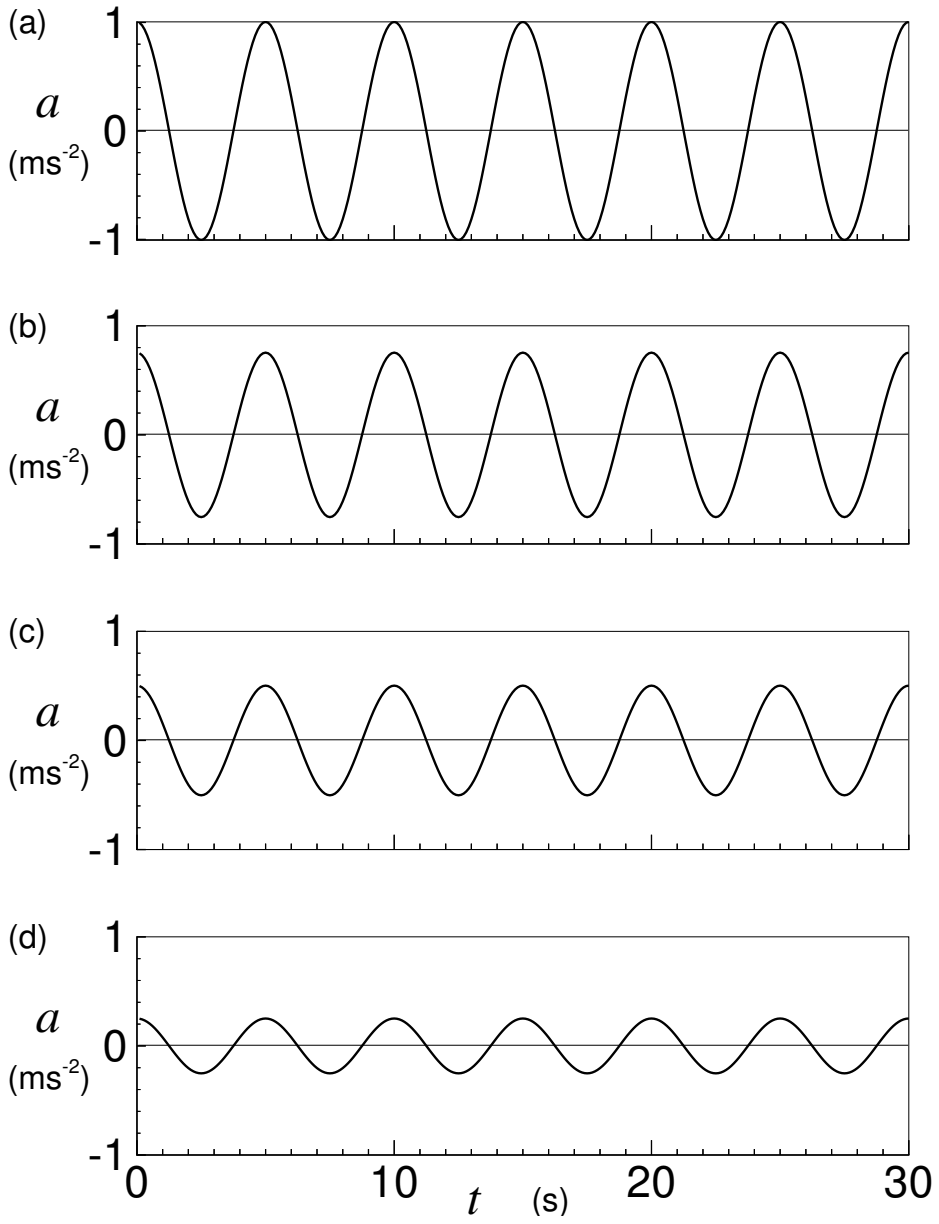

Figure 6.16: Time derivative of the free stream velocity, $a = \frac{\partial U_\infty(t)}{\partial t}$, for a sine wave of amplitude (a) Case 1, $U_m = 0.80$ m s^{-1}; (b) Case 2, $U_m = 0.60$ m s^{-1}; (c) Case 3; $U_m = 0.40$ m s^{-1}; and (d) Case 4, $U_m = 0.20$ m s^{-1}.

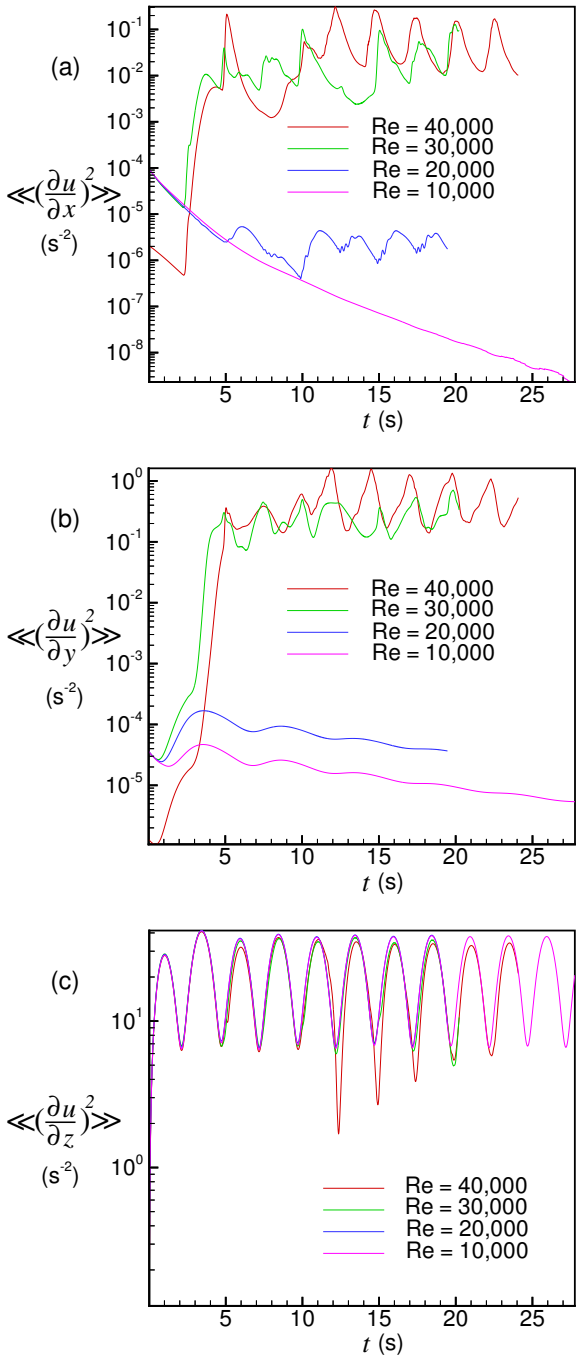

Figure 6.17: Volume mean square shear as a function of time for (a) $\left\langle\left\langle(\frac{\partial u}{\partial x})^2\right\rangle\right\rangle$, (b) $\left\langle\left\langle(\frac{\partial u}{\partial y})^2\right\rangle\right\rangle$, and (c) $\left\langle\left\langle(\frac{\partial u}{\partial z})^2\right\rangle\right\rangle$ for Case 1, Re = 40,000; Case 2, Re = 30,000; Case 3, Re = 20,000; and Case 4, Re = 10,000.

intensity of the mean square shears, it can be noticed that typically

$$\left\langle\left\langle \frac{\partial u}{\partial z}^2 \right\rangle\right\rangle \sim 40 \left\langle\left\langle \frac{\partial u}{\partial y}^2 \right\rangle\right\rangle \sim 400 \left\langle\left\langle \frac{\partial u}{\partial x}^2 \right\rangle\right\rangle \tag{6.27}$$

Note that $\left\langle\left\langle \frac{\partial u}{\partial y}^2 \right\rangle\right\rangle$ is larger than $\left\langle\left\langle \frac{\partial u}{\partial x}^2 \right\rangle\right\rangle$ during periods of laminar flow, that is when streamwise streaks are evident, $\frac{\partial u}{\partial y} \neq 0$, as seen in Figure 6.3 (b). Based on (6.27), it is evident why most of the energy dissipation comes from the term $\left\langle\left\langle \frac{\partial u}{\partial z}^2 \right\rangle\right\rangle$. This justifies why the approximate method for the energy dissipation given in Figure 6.12 is fairly accurate, since a term that is measured directly is dominant. Exponential growth in $\left\langle\left\langle \frac{\partial u}{\partial x}^2 \right\rangle\right\rangle$ and $\left\langle\left\langle \frac{\partial u}{\partial y}^2 \right\rangle\right\rangle$, for 3.5 s $< t <$ 5 s, shows evidence of linear instabilities present in the boundary layer flow during flow deceleration, the flow being maximum at $t \sim 3.75$ s and decelerating thereafter. $\left\langle\left\langle \frac{\partial u}{\partial x}^2 \right\rangle\right\rangle$ decreases as a function of time for the lower Reynolds number experiments particularly for $Re = 20,000$ ($Case$ 3) and $Re = 10,000$ ($Case$ 4). For $Re = 20,000$, the three-dimensional aspects of the flow decay in time from initial low level white noise. For $Re = 20,000$, $\left\langle\left\langle \frac{\partial u}{\partial x}^2 \right\rangle\right\rangle$ shows some small perturbations from $t = 5$ s, suggesting a flow near transition. The same comportment is observable in Figure 6.17 (b) with $\left\langle\left\langle \frac{\partial u}{\partial y}^2 \right\rangle\right\rangle$. Finally, $\left\langle\left\langle \frac{\partial u}{\partial z}^2 \right\rangle\right\rangle$, shown in Figure 6.15 (c) doesn't change significantly as a function of the Reynolds number and illustrates the periodic characteristic of the flow. This explains why volume-averaged and time-averaged net dissipation rates are similar for laminar and turbulent flows. Note also that the values of $\left\langle\left\langle \frac{\partial u}{\partial z}^2 \right\rangle\right\rangle$ are larger for $Re = 10,000$ (laminar flow) than for $Re = 40,000$ (strongest turbulence), in agreement with determinations of the volume averaged total kinetic energy dissipation rate from Figure 6.12 above.

6.4 Wave Periods

Numerical experiments have been conducting for different wave periods, T, holding $U_m = 0.8$ m s^{-1} constant. The characteristics of these runs are presented in Table 4.1.

6.4.1 Turbulent Kinetic Energy for Different Wave Periods

The horizontally averaged turbulent kinetic energy for different wave periods, $T = 3$ s (*Case* 5), $T = 8$ s (*Case* 6), $T = 12.5$ s (*Case* 7) and $T = \infty$ (*Case* 8) are shown in Figures 6.18 (a), (b), (c), and (d), respectively, and can be compared with the five-second period wave, shown in Figure 6.5 (a). Note that the scale in contour legend is not the same for panel (d). The comparison of the intensity of the turbulent kinetic energy shows that as the period T increases, or the frequency $\omega = \frac{2\pi}{T}$ decreases, the flow becomes more turbulent and the turbulent boundary layer thickness increases, e.g., $\delta_\tau = 0.5$ cm for $T = 3$ s, $\delta_\tau = 2.5$ cm for $T = 5$ s, $\delta_\tau = 3$ cm for $T = 8$ s and $\delta_\tau = 4$ cm for $T = \infty$ (this is evident if the contour levels are decreased to be the same as the other panels, but causes the rest of the structure to be obscured). In Figure 6.18 (c), turbulence is almost continuous in a sense that each event persists for $z > 2$ cm until the next begins near $z < 0.5$ cm. In the first three panels, the turbulent kinetic energy levels are periodic. However, in Figure 6.18 (d), the flow stays turbulent as the velocity never decreases for the steady flow, i.e., the flow can not be reorganized as in the oscillatory flows during flow acceleration. In the case of steady flow, the turbulence intensity becomes practically constant throughout the boundary layer for $t > 12$ s. Panel (d) represents the Rayleigh problem, an impulsively accelerated uniform flow over a flat plate. Initial attempts with the Rayleigh problem (not shown), using low-level white noise initialized with $u'^2 + v'^2 + w'^2 \sim 10^{-4} U_m$

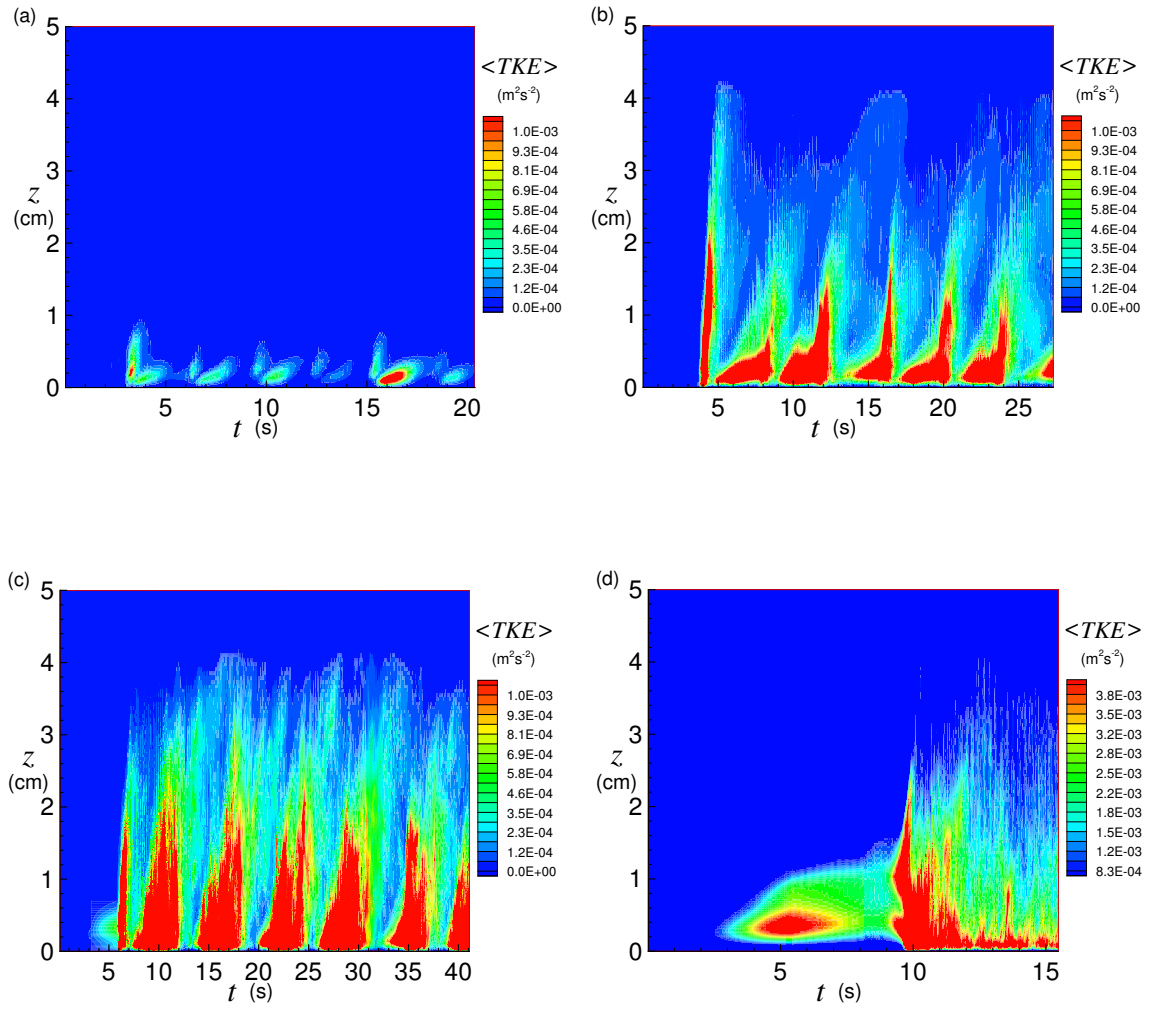

Figure 6.18: Horizontally averaged turbulent kinetic energy $\langle TKE(z,t)\rangle$ (m^2 s^{-2}) for (a) Case 5, T = 3 s; (b) Case 6, T = 8 s; (c) Case 7, T = 12.5 s; (d) Case 8, T = ∞; compare also to Figure 6 for Case 1, T = 5 s; note change of scale in contour legend for panel (d).

remained laminar. Initial perturbations associated with boundary layer instabilities grew for a short period of time and then decayed.

In laboratory experiments of a spatially developing boundary layer over a flat plate, the Tolmein-Schlichting (Schlichting [58]) instabilities have been found to develop when forced at unstable wavenumbers with a fluctuating ribbon over a smooth flat plate when $u' = 0.03U_m$. When smaller amplitude perturbations are attempted, the flow response is similar to what is observed in our Rayleigh experiments with low level white noise fluctuations. Tolmein-Schlitching waves do not lead to turbulence over smooth boundaries for the classical self similar Rayleigh velocity profile. The region of elevated velocity fluctuations shown in Figure 6.18 (d) for $4 < t < 7$ s are representative of streamwise streaks that grow and then decay before the flow transitions to turbulence at later time when hairpin vortices develop near $t = 9$ s that finally cause three-dimensionality to spread across the boundary layer.

Complicating the interpretation of the role of flow deceleration and acceleration, in understanding transitioning flows, it is noted that the derivative of the free stream velocity, $a = \dfrac{\partial U_\infty(t)}{\partial t}$, plotted in Figure 6.19, shows that as the wave period, T, increases, the magnitude of the acceleration-deceleration decreases. In these experiments, it is the flow with weaker deceleration that become more turbulent. However, it has also been seen that as T increases, the turbulence increases. Thus, it is suggested that the duration of deceleration phase can be more significant than its amplitude for different flow situations. In these cases. the frequency Reynolds number is still a useful predictor of flow transition, since Re_ω decreases as ω increases. For $Case$ 5, $Re_\omega \approx 300,000$ with $T = 3$ s, and the flow is only weakly turbulent, compared to $Cases$ 1, 6, and 7 with $T = 3$, 8, and 12.5 s with $Re_\omega \approx 510,000$, 815,000, and 1,270,000.

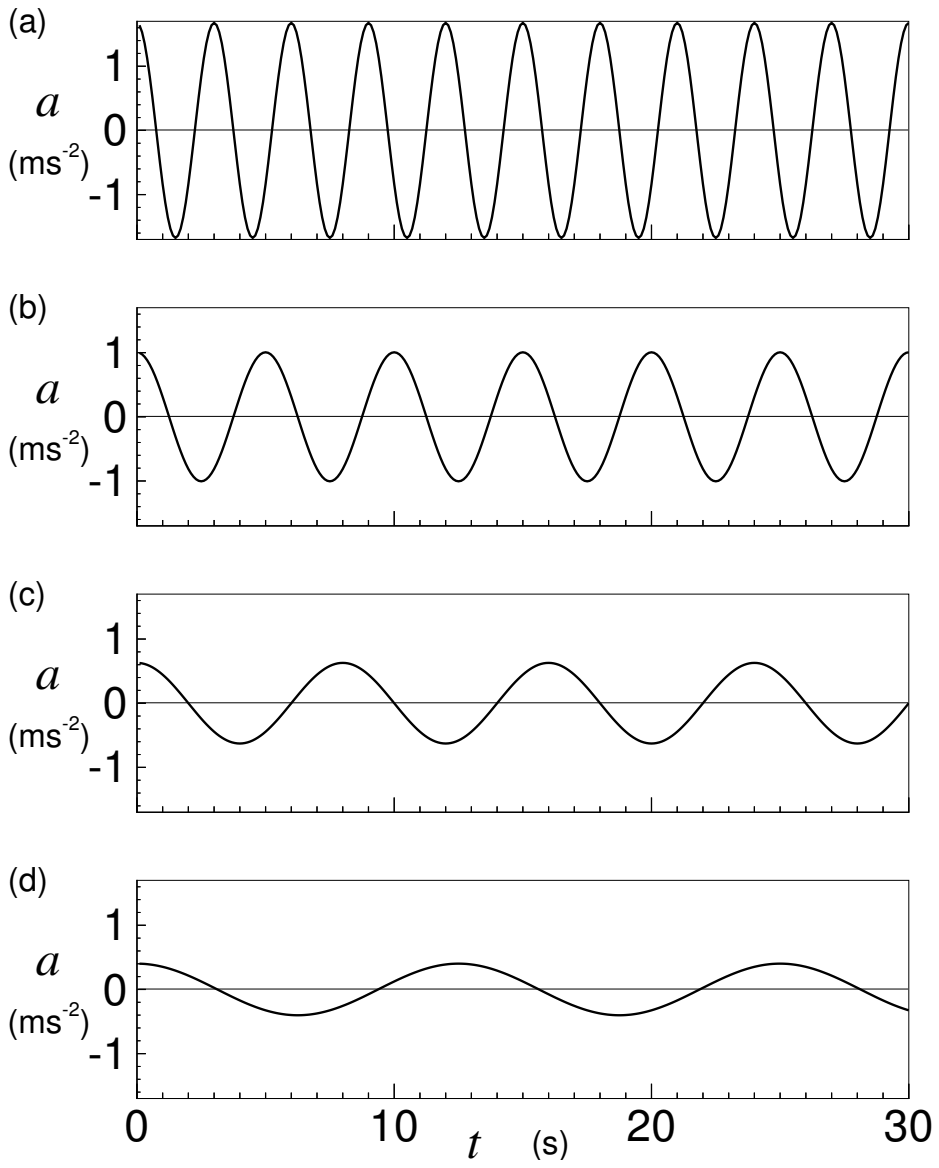

Figure 6.19: Time derivative of the free stream velocity, $a = \frac{\partial U_\infty(t)}{\partial t}$, for a sine wave of period (a) Case 5, $T = 3$ s; (b) Case 1, $T = 5$ s; (c) Case 6, $T = 8$ s; and (d) Case 7, $T = 12.5$ s.

6.4.2 One-Dimensional Model for Different Wave Periods

Results obtained with the Grant and Madsen ($G\&M$) and Trowbridge and Madsen ($T\&M$) eddy viscosity models are shown in Figure 6.20, for different phases of flow for *Cases* 5-7 with different wave periods. These results are compared with those obtained with the solution for a constant viscosity (*Laminar*) and the three-dimensional model ($3D$).

Figures 6.20 (a), (c), and (e) show velocity profiles at flow reversal, while Figures 6.20 (b), (d), and (f) present velocity profiles near maximum flow. As in Figure 6.9, all the models give the same basic shape of curves, however, the one-dimensional models seem to be more accurate in the case of maximum flow than near flow reversal. For a period of 3 seconds, the flow is not very turbulent so the laminar solution worked well for this case. The one-dimensional models generally underpredict $\frac{\partial u}{\partial z}$ near the wall and overpredict the boundary layer thickness, especially near flow reversal. For a 8-second period wave, as shown in Figures (c) and (d), the viscosity-based models are qualitatively much better than laminar results at flow reversal. Difficulties remain near maximum flow when turbulence decays because of flow acceleration. Figures 6.20 (e) and (f) show that the Grant and Madsen and Trowbridge and Madsen models give progressively better approximation as T and the net turbulence increase. These results will be quantified in more detail below.

6.5 Wave Shape

Numerical experiments have also been conducted for different shapes of free-stream velocity time series that would be produced by different shapes of surface waves, a skewed (steep) wave, a complex frequency wave, and a wave packet, to study the flow

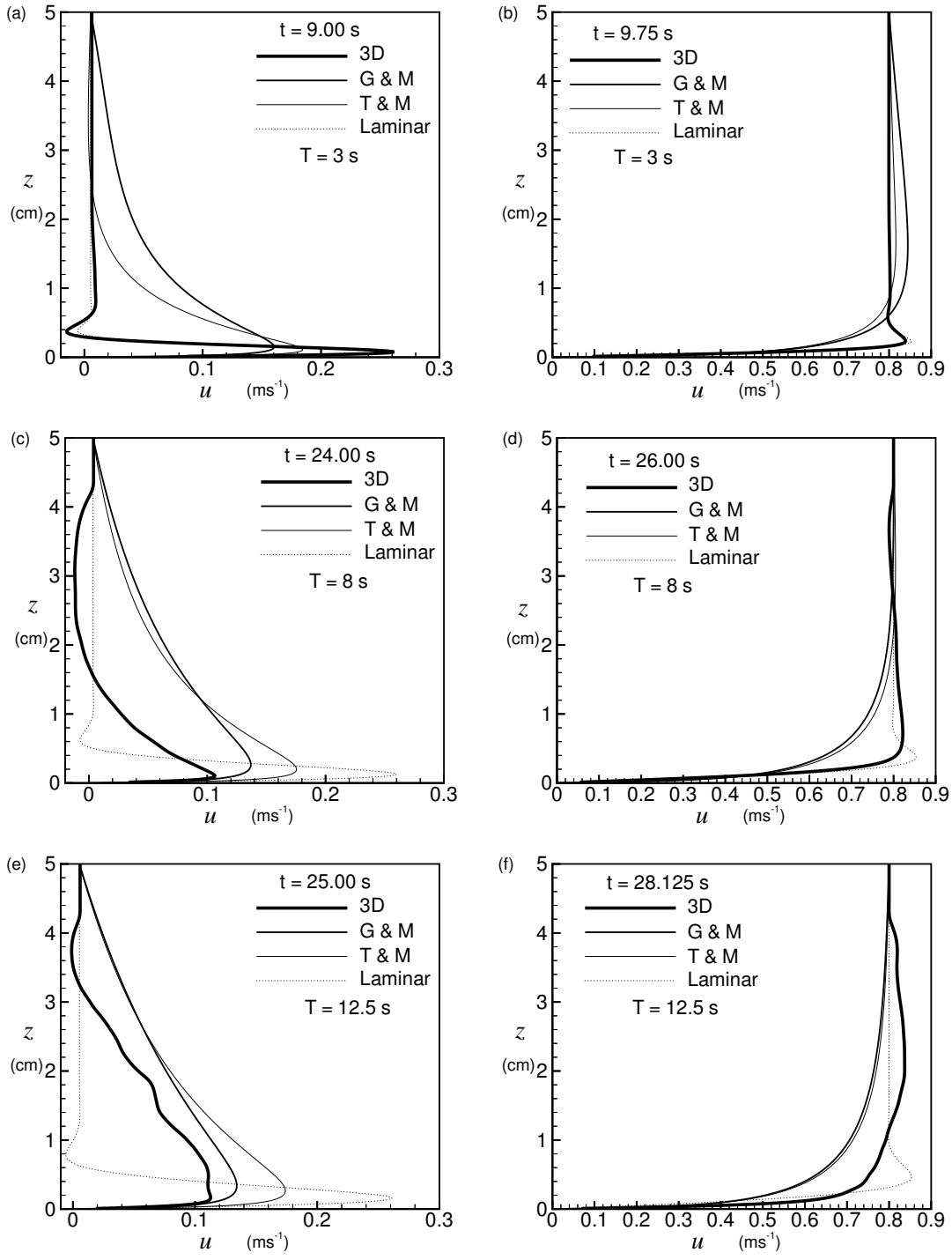

Figure 6.20: Comparisons of mean velocity profiles from the 3-dimensional model (3D), Grant and Madsen model (G & M), Trowbridge and Madsen model (T & M), and laminar model (Laminar) at different wave phases for Case 5, T = 3 s, at (a) $t = 9.00$ s and (b) $t = 9.75$ s; Case 6, T = 8 s, at (c) $t = 24.00$ s and (d) $t = 26.00$ s; and Case 7, T = 12.5 s, at (e) $t = 25.00$ s and (f) $t = 28.125$ s.

response in the boundary layer to these variations. The characteristics of these flows are given in Table 4.1.

6.5.1 Turbulent Kinetic Energy for Different Wave Shapes

The horizontally averaged turbulent kinetic energy for different types of forcing, skewed wave, complex wave, and wave packet, (*Cases* 9-11) are shown in Figures 6.21 (a), (b), and (c), respectively. The skewed wave forcing condition (*Case* 9) has a basic wave period $T = 5$ s. It is plotted in Figure 6.1 (b), and given by

$$U_\infty(t) = -0.8(U_{free} - 4.0), \tag{6.28}$$

where U_{free} is determined iteratively using

$$U_{free} = 4.0 + \sin\left[\frac{2\pi}{5}\left(t - \frac{C}{U_{old}^2}\right)\right], \tag{6.29}$$

where $C = 18$ is a constant and U_{old} equals the value of U_{free} at a previous iteration. The value of U_{free} is obtained by iteration, i.e., by substituting U_{old} by the previous value of U_{free} till the difference between U_{free} and U_{old} is less than 10^{-10}.

The skewed wave forcing velocity can be decomposed into two parts, the sharp phase, e.g., from $t = 5$ s to $t = 7$ s, and the gradual phase, e.g., from $t = 7$ s to $t = 10$ s. Generally, during more gradual deceleration phases, e.g., from $t = 12$ s to $t = 13.5$ s, some fast (i.e., 0.2 s) bursts of turbulence of characteristic thickness of 1 cm and turbulent kinetic energy level of approximately 2x10^{-3} m^2 s^{-2}, e.g., at $t = 13.5$ s, are present in Figure 6.21 (a). During sharp acceleration phases, the turbulent boundary layer response lasts about 1 s and has characteristic thickness of 0.5 cm and turbulent kinetic energy level of approximately 8x10^{-4} m^2 s^{-2}. A pattern of strong-weak-strong-weak turbulence can be observed. It is, however, interrupted by anomalous stronger turbulent bursts at $t = 15$ s and $t = 40$ s, i.e., every four

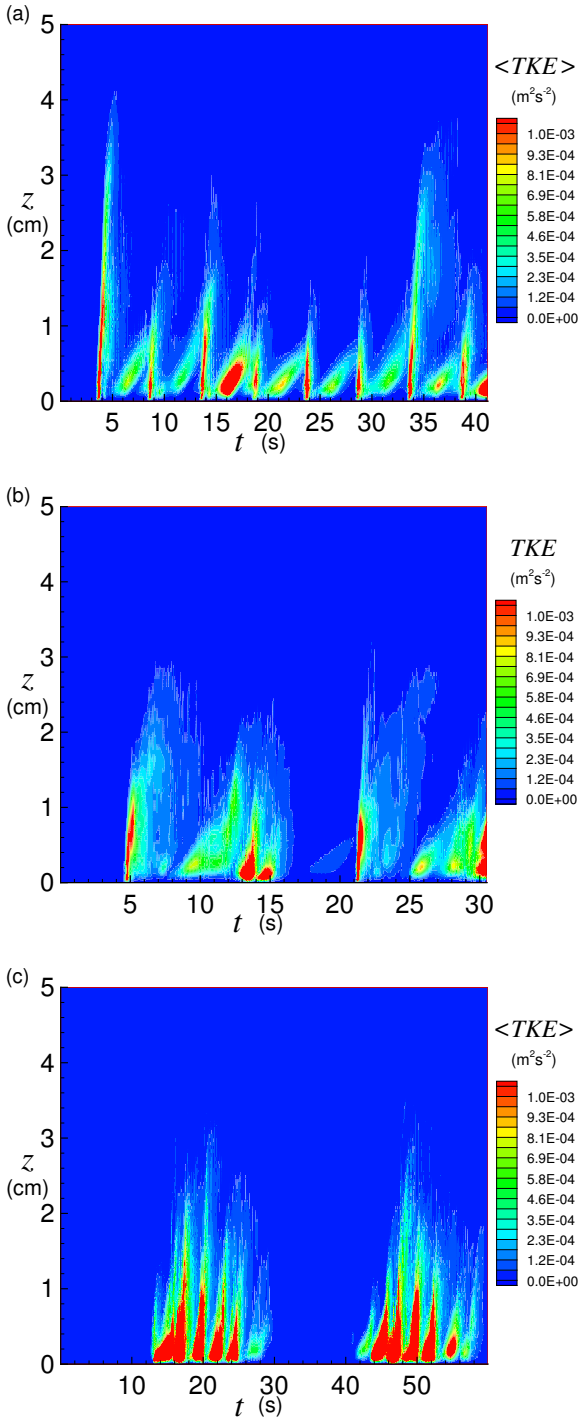

Figure 6.21: Horizontally averaged turbulent kinetic energy $\langle TKE(z,t)\rangle$ (m^2 s^{-2}) for (a) Case 9, skewed wave; (b) Case 10, complex wave; and (c) Case 11, wave packet.

wave periods. After these stronger bursts, the following wave periods exhibit weaker turbulence.

By calculating the acceleration of the flow, $a = \frac{\partial U_\infty(t)}{\partial t}$, plotted in Figure 6.22 (a), it can be observed that during gradual phases, the deceleration of the flow, which destabilizes the boundary layer, is relatively weak, i.e., 0.5 m s^{-2} and lasts 1.5 s, e.g., from $t = 7$ s to $t = 8.5$ s. During sharp phases, the deceleration of the flow is stronger, i.e., about 2.7 m s^{-2} and last only 0.5 s, e.g., from $t = 10.5$ s to $t = 11$ s.

The complex wave (*Case* 10) is obtained by adding 5 sine waves with different amplitudes, frequencies, and phases, such that

$$\begin{aligned} U_\infty(t) &= 0.2\sin(\frac{2\pi}{2}t + 1) + 0.3\sin(\frac{2\pi}{3}t + 34.9) + 0.3\sin(\frac{2\pi}{5}t + 1.6) + \\ & \quad 0.3\sin(\frac{2\pi}{7}t + 7) + 0.3\sin(\frac{2\pi}{11}t + 15). \end{aligned} \tag{6.30}$$

The plot of the free stream velocity is shown in Figure 6.1 (c). The horizontally averaged turbulent kinetic energy for this complex wave forcing is given in Figure 6.21 (b). Significant turbulent bursts originate at approximately $t = 5$ s, $t = 9$ s, $t = 12.5$ s, $t = 14$ s, $t = 21$ s, $t = 26$ s and $t = 28$ s. By considering the derivative of the velocity plotted in Figure 6.22 (b), these bursts may be directly associated with periods of flow deceleration of about $a = 1.1$ m s^{-2}, $a = 1.5$ m s^{-2}, $a = 0.8$ m s^{-2}, $a = 1.2$ m s^{-2}, $a = 1.6$ m s^{-2}, $a = 0.9$ m s^{-2} and $a = 1.2$ m s^{-2}, respectively. Turbulent events do not occur for example at $t = 18$ s or $t = 23$ s during phases of flow deceleration with amplitudes of the order of $a = 0.2$ m s^{-2}, $a = 0.5$ m s^{-2}. For this experiment, whenever deceleration exceeds a threshold of approximately 0.8 m s^{-2}, the boundary layer becomes turbulent.

The wave packet (*Case* 11), product of two sine functions, is given by

$$U_\infty(t) = 0.8\sin(\frac{2\pi}{5}t)\sin(\frac{2\pi}{60}t) \tag{6.31}$$

This represents a carrier wave with an envelope of 30 seconds modulating a higher frequency wave with period $T = 5$ s. The wave packet essentially groups several different Reynolds number experiments together since U_m effectively changes over each short wave period of 5 s. Time series of the free-stream velocity are plotted in Figure 6.1 (d). The wave packet forcing condition induces corresponding packets of turbulence with a phase lag, as shown in Figure 6.21 (c). The boundary layer thickness, $\delta_\tau = 2$ cm, has the same basic shape as the carrier envelope. Clearly, the fundamental frequency of 5 seconds is evident in the bursts of turbulent kinetic energy. Asymmetry in the turbulent kinetic energy response is visible about the maximum of the envelope, which is centered at $t = 15$ s and $t = 45$ s. The turbulent kinetic energy has maximum near $t = 19$ s and $t = 49$ s, a phase lag of about 4 seconds or approximately one wave period. This suggests that turbulence levels during preceding events influences the stability and production of turbulence during subsequent events. The periodicity of the turbulent kinetic energy, seen in *Cases* 1-4, is clearly evident for the case of the wave packet. The flow becomes turbulent at $t = 12.5$ s and half a period later at $t = 42.5$ s when the free stream velocity $U_\infty(t)$ reaches a certain value of 0.45 m s^{-1}. Then the turbulence decays when the magnitude of the velocity $U_\infty(t)$ again becomes too small, around $t = 28$ s and $t = 58$ s. It can be noticed in Figure 6.22 (c), that turbulence first develops when the deceleration of the flow is greater than $a = 0.95$ m s^{-2} and vanishes around $t = 28$ s when $a = 0.6$ m s^{-2}.

It can be concluded that a different wave form, i.e., a different time-dependence of the free-stream velocity, especially near flow reversal, causes a different turbulent response in the turbulent boundary layer. The magnitude of the deceleration, the duration of deceleration, and the recent history of the turbulence levels in the previous wave oscillations are important parameters in the generation of turbulence.

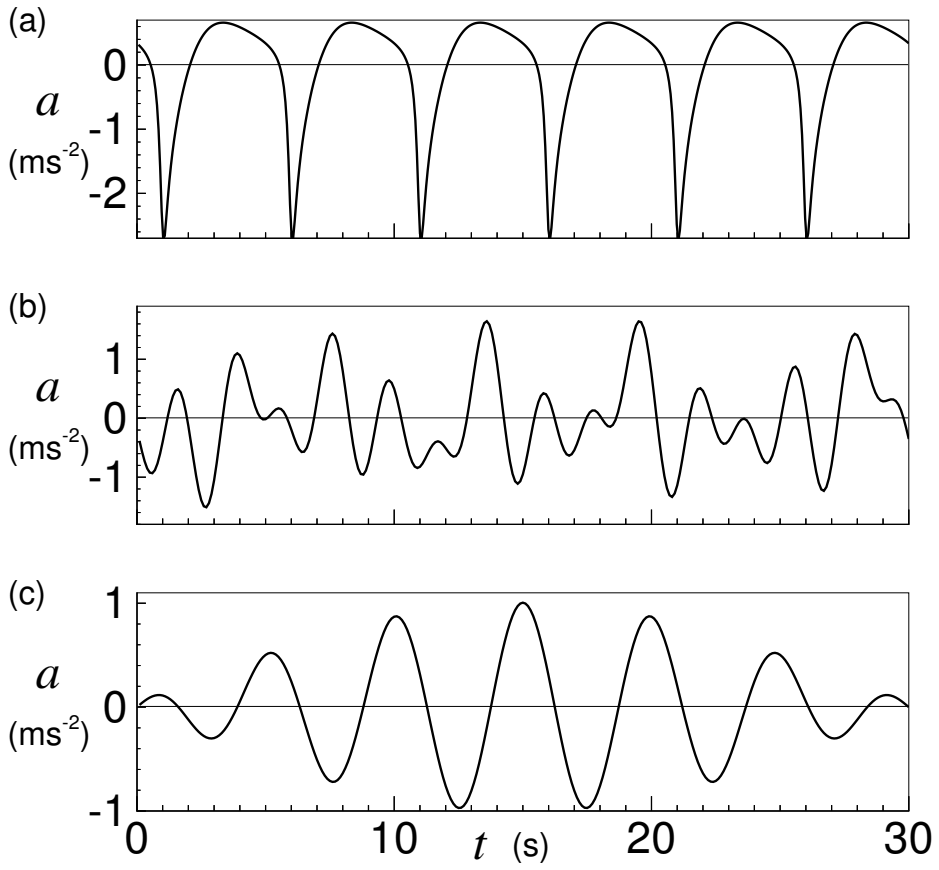

Figure 6.22: Time derivative of the free stream velocity, $a = \frac{\partial U_\infty(t)}{\partial t}$, for different shapes of waves (a) Case 9, skewed wave; (b) Case 10, complex wave; and (c) Case 11, wave packet.

6.5.2 One-Dimensional Comparisons for Different Wave Shapes

Results obtained with the Grant and Madsen ($G\&M$) and Trowbridge and Madsen ($T\&M$) eddy viscosity models are shown in Figure 6.23, for the skewed and complex cases, for different phases of flow. These results are compared with those obtained with a constant viscosity ($Laminar$) and from the three-dimensional model ($3D$).

Figure 6.23 (a) presents velocity profiles of the skewed wave at $t = 13.75$ s. Figure 6.1 (b) shows that this is during a phase of flow reversal and velocity profiles in Figure 6.21 (a) indicates it is during a phase of strong turbulence. Figure 6.23 (b) shows the velocity profiles at $t = 15.50$ s, which corresponds to a period of maximum flow. Figure 6.23 (c) presents velocity profiles of the complex case at $t = 16.00$, i.e., during two successive phases of flow reversal (Figure 6.1 (c)) and panel (d) presents the velocity profiles at $t = 20.00$ s, which corresponds to a period of maximum flow.

As for previous cases, the one-dimensional models give good approximations of the three-dimensional model at phases of strong flow, as shown in Figures 6.23 (b) and (d). Similarly, the one-dimensional models underpredicts $\frac{\partial u}{\partial z}$ near the wall and overpredicts the boundary layer thickness, especially at flow reversal. It can be seen that the Grant and Madsen ($G\&M$) and Trowbridge and Madsen ($T\&M$) models give a better approximation of the three-dimensional model in the case of flow reversal periods than the laminar velocity profile.

6.6 Combined Mean Flow and Wave Features

The next group of numerical experiments includes mean cross currents of different intensities in the y-direction in the model, perpendicular to the direction of the wave oscillation. The characteristics of these wave-current flows ($Cases$ 12-14) are de-

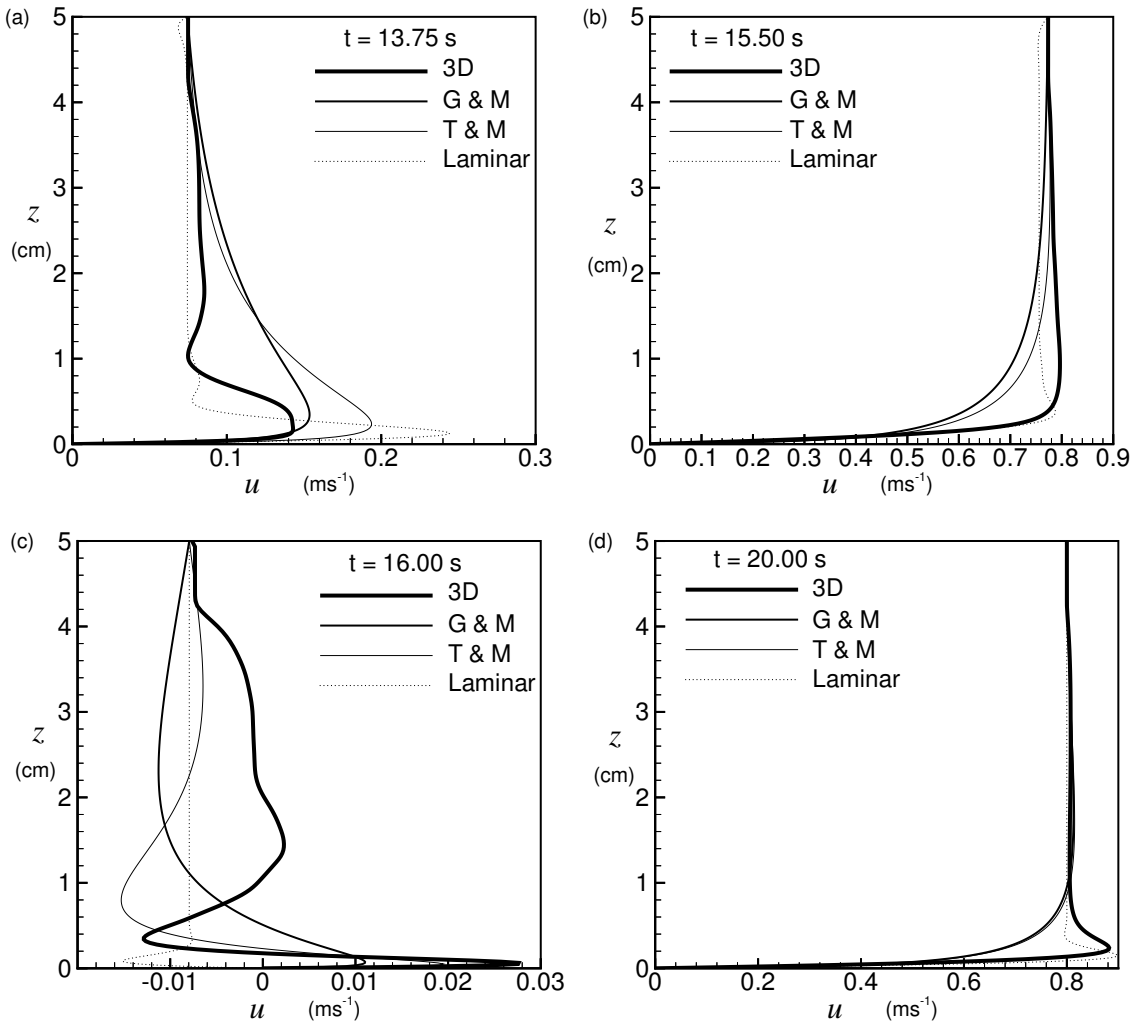

Figure 6.23: Comparisons of mean velocity profiles from the 3-dimensional model (3D), Grant and Madsen model (G & M), Trowbridge and Madsen model (T & M), and laminar model (Laminar) at different phases of wave for Case 9, skewed wave, at (a) t = 13.75 s and (b) t = 15.50 s; and Case 10, complex wave, at (c) t = 16.00 s and (d) t = 20.00 s.

scribed in Table 4.1.

6.6.1 Turbulent Kinetic Energy for Different Wave-Current Flows

The horizontally averaged turbulent kinetic energy for different mean currents, $V_\infty =$ 0.15 m s^{-1} (*Case* 12), $V_\infty = 0.30$ m s^{-1} (*Case* 13) and $V_\infty = 0.60$ m s^{-1} (*Case* 14), added to a five-second period wave, $U_\infty = 0.60 \sin(\frac{2\pi}{5})$ m s^{-1}, are shown in Figures 6.24 (a), (b), and (c), respectively.

These plots can be compared with Figure 6.15 (a), for $V_\infty = 0.0$ m s^{-1} (*Case* 2). Figure 6.24 (a) is significantly less turbulent than the case without any mean current, and the turbulence decreases with time. Hence, addition of a weak mean current to the wave boundary layer decreases the intensity of the turbulence. Figure 6.24 (a) is a oscillatory wave flow with a weak drift. For panel (b) and (c), the addition of a mean current causes the boundary layer thickness to increase. In *Case* 14, the boundary layer thickness, δ_τ, can not be determined as it is simply larger than $L^{(z)}$. Most of the turbulent kinetic energy, however, is below 3 cm, with occasional eddies that hit the sponge layer. Flow visualizations suggest that the experiment represented in panel (c) is like a steady mean current with shifting direction and panel (b) is in an intermediate regime where, both, wave and steady flow features are present. The Reynolds number, in these cases, is determined with a maximum velocity amplitude $(U_m^2 + V_\infty^2)^{1/2}$. In panel (c), there is a discernible wave pulse in the turbulent kinetic energy related to wave flow reversal. Some qualitative similarities to the steady-flow case, Figure 6.18 (c), can be observed. The initial transition to turbulence for panel (a) and (b) occurs at $t = 5$ s, right at flow reversal. For panel (c), however, transition occurs at $t = 2.5$ s. This is probably related to stronger instability associated with the stronger mean current. For $V_\infty = 0.30$ m s^{-1}, the turbulence does not completely

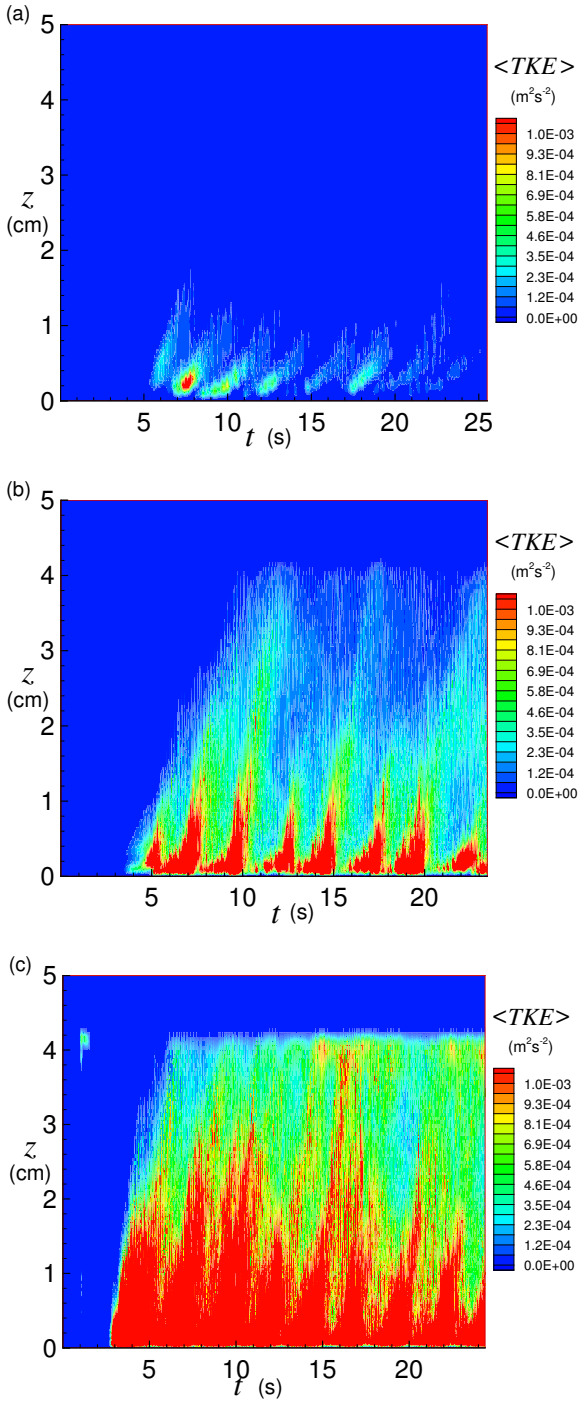

Figure 6.24: Horizontally averaged turbulent kinetic energy $\langle TKE(z,t)\rangle$ (m^2 s^{-2}) for a sine wave, T = 5 s and U$_m$ = 0.60 m s^{-1} and a mean current (a) Case 12, V$_\infty$ = 0.15 m s^{-1}; (b) Case 13, V$_\infty$ = 0.30 m s^{-1}; and (c) Case 14, V$_\infty$ = 0.60 m s^{-1}; compare also to Figure 14 (a) for Case 2, V$_\infty$ = 0.0 m s^{-1}.

extinguish between wave cycles compared to *Cases* 1 or 2 (i.e., at similar Re). This must be caused by the influence of the mean flow and continuous turbulent production in the y-direction.

6.6.2 Wall Shear Components for Different Mean Currents

Horizontally averaged wall shear components in the x-direction, τ_{xw}, and in the y-direction, τ_{yw}, as well as the root mean squared variances σ_{xw} and σ_{yw} are shown for different strengths of mean currents for combined wave-current experiments, $V_\infty = 0.0$ m s^{-1} (*Case* 2), $V_\infty = 0.15$ m s^{-1} (*Case* 12), $V_\infty = 0.30$ m s^{-1} (*Case* 13) and $V_\infty = 0.60$ m s^{-1} (*Case* 14) in Figure 6.25 (a), (b), (c) and (d), respectively. These quantities are given by

$$\tau_{xw} = \mu \left\langle \frac{\partial u}{\partial z}\Big|_w \right\rangle, \tag{6.32}$$

$$\tau_{yw} = \mu \left\langle \frac{\partial v}{\partial z}\Big|_w \right\rangle, \tag{6.33}$$

$$\sigma_{xw} = \mu \left\langle \left(\frac{\partial u}{\partial z}\Big|_w (x,y,t) - \left\langle \frac{\partial u}{\partial z}\Big|_w (t) \right\rangle \right)^2 \right\rangle^{1/2}, \tag{6.34}$$

$$\sigma_{yw} = \mu \left\langle \left(\frac{\partial v}{\partial z}\Big|_w (x,y,t) - \left\langle \frac{\partial v}{\partial z}\Big|_w (t) \right\rangle \right)^2 \right\rangle^{1/2}, \tag{6.35}$$

In panel (a), the u-component of the shear is almost periodic and sinusoidal and the variations from the horizontally mean wall shear, σ_{xw} and σ_{yw}, are small. In panel (a) and (c), $\sigma_{xw} > \sigma_{yw}$, which is a characteristic of the wave dominated situation, in panel (d), however, σ_{xw} is nearly equal to σ_{yw}, suggesting a more isotropic response during turbulence and that the flow, when $U_\infty = V_\infty$, is at a 45° angle. In panel (a), there is no mean shear in the y-direction. In panel (b), τ_{yw} decreases rapidly from $t = 0$ to $t = 5$ s from the value 0.2 Pa to 0.01 Pa, as the mean velocity profile adjusts from the initialized thin boundary layer profile. σ_{xw} and σ_{yw} are much smaller than in panel (a), as this case is less turbulent, as seen in Figure 6.24 (a). In panels (c)

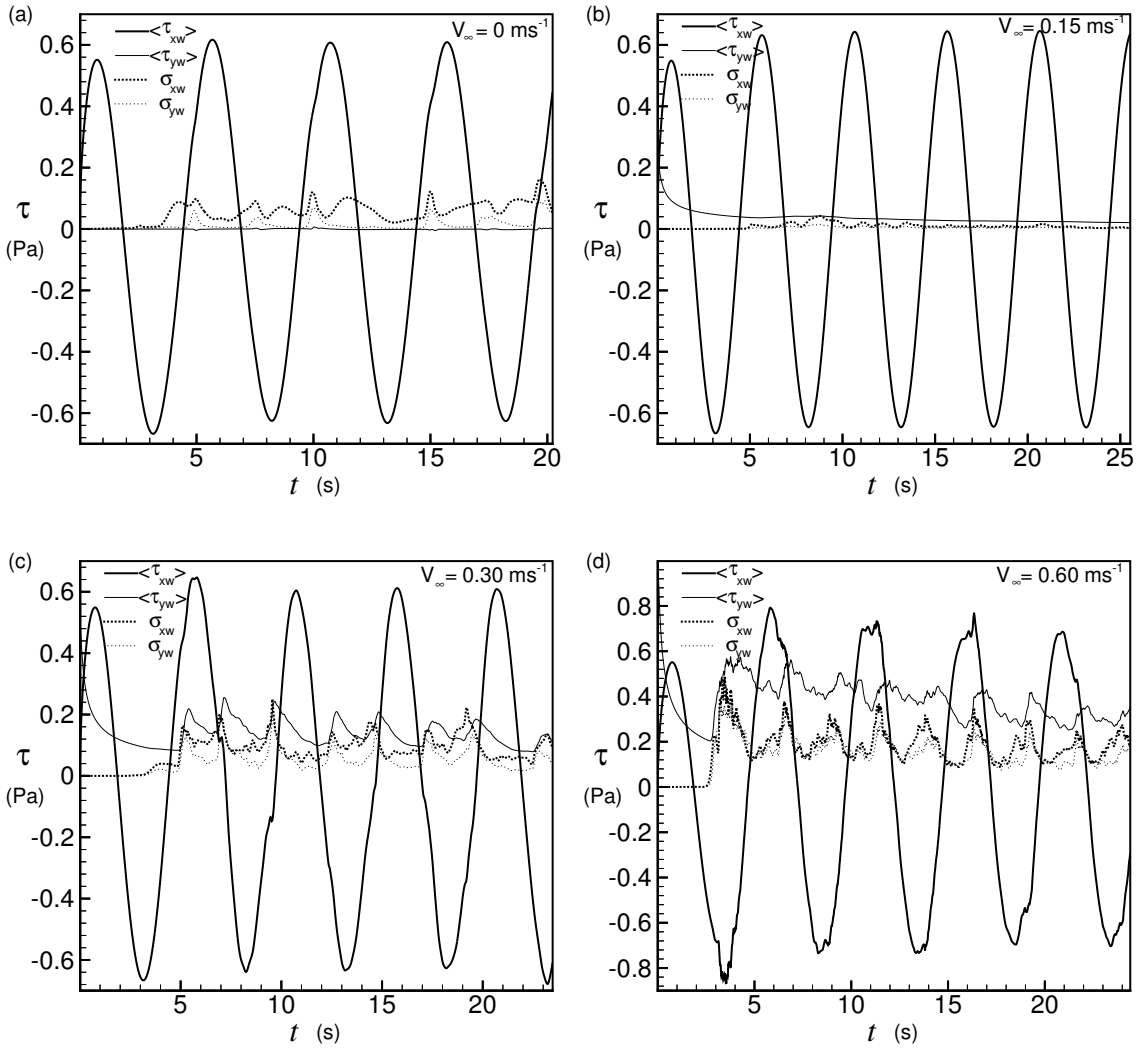

Figure 6.25: Horizontally averaged wall shear components $\langle \tau_{xw} \rangle = \mu \left\langle \frac{\partial u}{\partial z}\Big|_w \right\rangle$ and $\langle \tau_{xw} \rangle = \mu \left\langle \frac{\partial v}{\partial z}\Big|_w \right\rangle$ (Pa) and root mean squared (rms) variance σ_{xw} and σ_{yw} (Pa), e.g., $\sigma_{xw} = \mu \left\langle \left(\frac{\partial u}{\partial z}\Big|_w (x,y,t) - \left\langle \frac{\partial u}{\partial z}\Big|_w (t) \right\rangle \right)^2 \right\rangle^{1/2}$ for different cases of wave-mean current flow: (a) Case 2, $\mathrm{V}_\infty = 0.0$ m s^{-1}; (b) Case 12, $\mathrm{V}_\infty = 0.15$ m s^{-1}; (c) Case 13, $\mathrm{V}_\infty = 0.30$ m s^{-1}; and (d) Case 14, $\mathrm{V}_\infty = 0.60$ m s^{-1}, all with $U_\infty(t) = 0.6 \sin(\frac{2\pi}{5} t)$ m s^{-1}.

and (d), it can be observed that as the current V_∞ increases, the y-component of the shear increases and its intensity fluctuates around 0.2 Pa and 0.4 Pa, respectively, for $V_\infty = 0.30$ m s^{-1} (*Case* 13) and $V_\infty = 0.60$ m s^{-1} (*Case* 14). Interestingly, τ_{yw} still decreases slowly with time. In Figure 6.25 (c), τ_{xw} is still periodic in time but is less like a sine wave than in Figure 6.25 (a). In Figure 6.25 (d), τ_{xw} increases to approximately 0.7-0.8 Pa compared to 0.6 Pa for panels (a), (b), and (c). For turbulent flows, the critical shear stress needed to suspend sediment of median grain size, d_{50}, on a flat horizontal surface is around 0.2 Pa for typical sand grains with diameters of approximately 0.2 mm (Julien [59]). The root mean squared variances increase as the mean currents and turbulence increase as shown in panels (c) and (d), suggesting that local wall shear stresses will significantly exceed mean values as turbulence levels increase, leading to increase potential for erosion of bed material (e.g. Figure 6.13).

6.7 Summary of the Experiments

Quantitative comparisons of average properties between the different numerical experiments conducted with the three-dimensional are presented.

6.7.1 RMS Differences in Mean Velocity Profiles

The root mean squared (*rms*) differences between the mean velocity profiles from the three-dimensional model and the various one-dimensional model predictions including the Grant and Madsen ($G\&M$), Trowbridge and Madsen ($T\&M$), and laminar (*laminar*) models for different cases; $T = 5$ s (*Case* 1), $T = 12.5$ s (*Case* 7), and complex wave (*Case* 10), are shown in Figure 6.26, (a), (b), and (c), respectively. The *rms* differences between the mean velocity profiles from the tree-dimensional model

$(3D)$ and the one-dimensional model is given by

$$rms(t) = \left(U_{3D}(t)^2 - U_{1D}(t)^2\right)^{1/2}. \tag{6.36}$$

The rms differences are not shown here from $t = 0$ s but for later periods when turbulence is present.

In Figure 6.26 (a), the laminar model (*laminar*) more closely approximates the velocity profiles determined with the three-dimensional model than the others models. The differences calculated are, however, relatively small in magnitude between all these models in this case. For $T = 12.5$ s, shown in panel (b), the flow is more turbulent, and the Grant and Madsen ($G\&M$) and Trowbridge and Madsen ($T\&M$) models give overall better agreement with the three-dimensional model than the laminar model (*laminar*). In Figure 6.26 (c), in the complex forcing case, the Grant and Madsen ($G\&M$) and Trowbridge and Madsen ($T\&M$) models give always a better approximation than the laminar model (*laminar*). There is no clear superiority between the Grant and Madsen model and Trowbridge and Madsen model.

The conclusion is that Madsen type models have best performance for more strongly turbulent and complex wave forcing conditions, and poorer performance for flows with intermittent turbulence.

6.7.2 Turbulent Kinetic Energy and Kinetic Energy Dissipation Rates

Lastly, spatial and temporal means of the turbulent kinetic energy and the kinetic energy dissipation rate from the three-dimensional experiments are presented. These are compared to laminar results for different values of the wave period T, panels (a) and (b), different Reynolds numbers, panels (c) and (d), and different mean currents, V_∞, panels (c) and (d), in Figure 6.27.

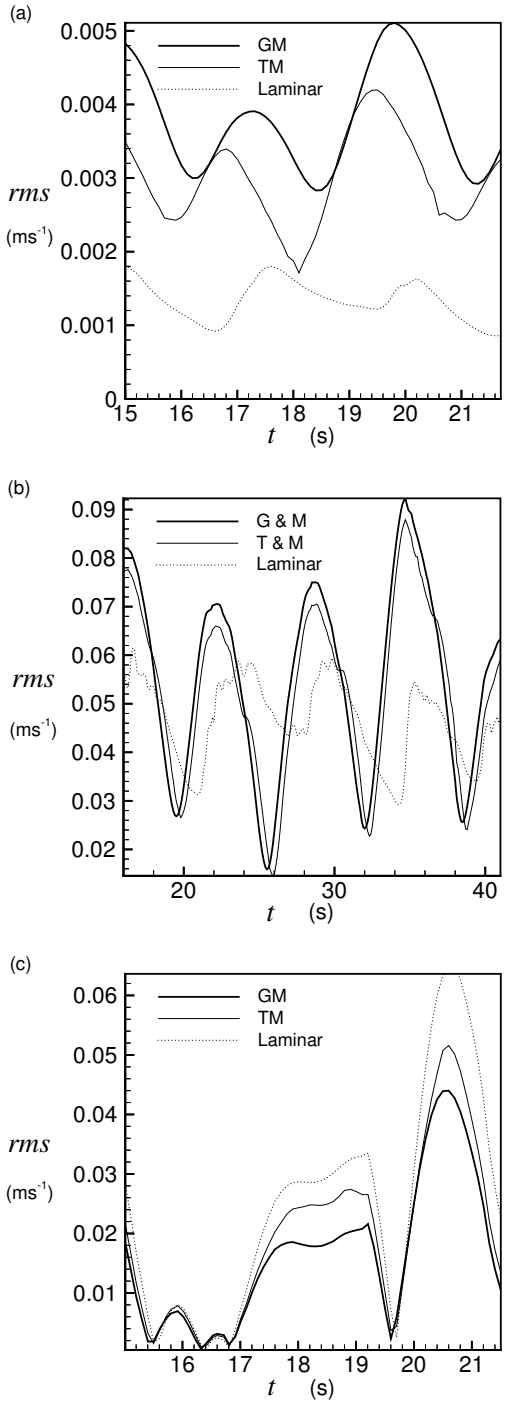

Figure 6.26: Root mean square differences (rms) between the mean velocity profiles from the 3-dimensional model and other model predictions including the Grant and Madsen model (G & M), Trowbridge and Madsen model (T & M), and laminar model (Laminar) as a function of time for (a) Case 1, T = 5 s; (b) Case 7, T = 12.5 s; (c) Case 10, complex wave.

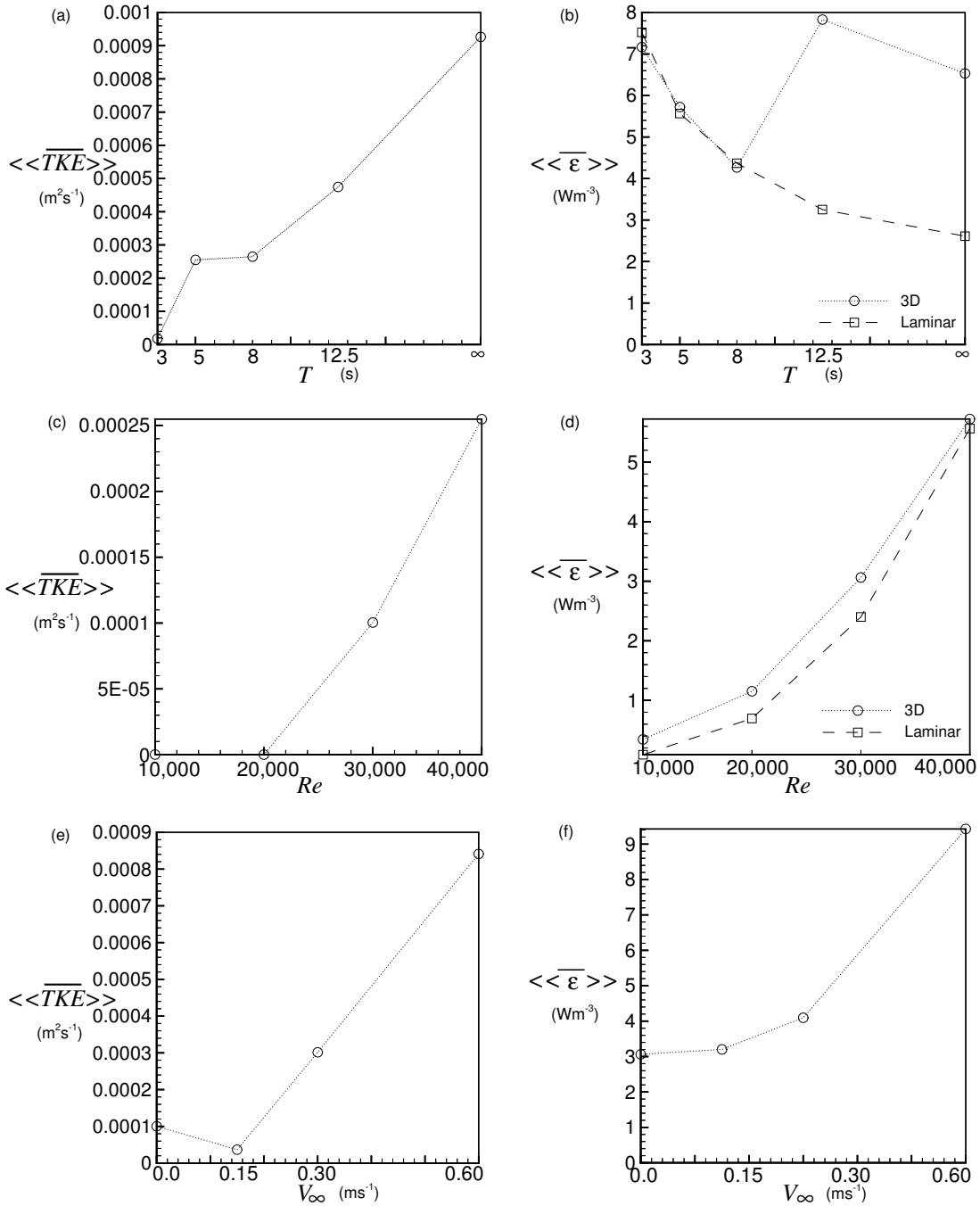

Figure 6.27: Spatial and temporal mean of turbulent kinetic energy for various experiments with (a) different values of the wave period T; (c) different Reynolds numbers with T = 5 s; and (e) different values of current V_∞. Spatial and temporal mean of kinetic energy dissipation rate from the turbulent simulations compared to laminar results for (b) different values of the wave period T; (d) different Reynolds numbers with T = 5 s; and (f) different values of current V_∞.

The mean turbulent kinetic energy increases as the period T increases as shown in panel (a), consistent with the increase in boundary layer thickness with T. The mean turbulent kinetic energy varies as T increases by approximately a factor of 3 from $T = 5$ s to $T = \infty$. The dissipation rate, plotted in panel (b), decreases as T increases for laminar flow but increases above the laminar results for the most turbulent cases, $T = 12.5$ s ($Case$ 7) and $T = \infty$ ($Case$ 8), in the three-dimensional model.

The mean turbulent kinetic energy also increases as the Reynolds number increases, for fixed $T = 5$ s, as shown in Figure 6.27 (c). The dissipation rate, panel (d), also increases for both the laminar and three-dimensional models as the Reynolds number increases. The three-dimensional results is slightly higher than the laminar result for $10,000 < Re < 30,000$.

Figure 6.27 (e) shows a point of inflection of the turbulent kinetic energy at $V_\infty = 0.15$ m s^{-1}, this case being less turbulent than the others. Generally, as the current V_∞ increases, the turbulent kinetic energy and dissipation rates increase, as shown in Figures 6.27 (e) and (f).

Chapter 7

Conclusion

Numerical experiments have been conducted with the high-resolution time-dependent three-dimensional numerical model developed by Slinn and Riley [4] in order to study the dynamics of the wave bottom boundary layer. Some improvements to the model have been implemented and four sets of parameter studies have been conducted. The first set of experiments has utilized simple harmonic waves with different wave amplitudes, U_m. A second set of experiments has varied the wave period, T. This set includes the limiting case of a steady flow. The third set of experiments has analyzed the flow response for different types of wave, e.g., a skewed wave, a complex wave, and a wave packet. The fourth and final set of experiments has examined the impact of including a mean current, V_∞, in the y-direction added to a 0.60 m s^{-1} sine wave propagating in the x-direction.

Variations of free-stream velocities, similar to those common in nature, have been applied. The results have shown that the model can make direct estimates for wave dissipation rates and turbulent kinetic energy for turbulent boundary layers that occur near the sea bed. Numerical experiments have been done to improve understanding of the properties of turbulence. Results have shown the dependence of the boundary layer on surface wave field conditions (wave amplitude, wave frequency, wave shape, presence of mean current) and described the different kinds of flow, laminar,

transitional, and turbulent that are produced.

Analysis of the basic flow features for a five second period wave of maximum amplitude 0.80 m s^{-1} has shown that the turbulence in the wave bottom boundary layer depicts initial transients during the first two wave periods before achieving a quasi-steady behavior. Subsequently, turbulent bursts become episodic in nature and are coupled to the wave cycle. Accelerating flow organizes the boundary layer structure, and decelerating flow destabilizes the boundary layer. Turbulent levels are usually the strongest near flow reversal. Moreover, the decay of turbulence seems to be more sudden than the onset of turbulence. The study of the kinetic energy dissipation rates has shown that the model is well-resolved and that the spatial resolution used in the three-dimensional model is adequate to the purposes of this work as the grid spacing is of the order of the Kolmogorov length scale. Instantaneous and mean velocity profiles show the characteristic features of wave bottom boundary layers, including the phenomenon of overshoot which occurs near the wall.

The model has been tested for different Reynolds numbers based on $Re = \frac{U_m L^{(z)}}{\nu}$, by varying the wave amplitude, U_m, and holding the wave period fixed. As the wave amplitude decreases, the turbulent kinetic energy and the turbulent boundary layer thickness decrease. A significant factor may be that the magnitude of the deceleration of the wave forcing decreases as the wave amplitude decreases. The laminar to turbulent transition occurs in the model for $Re \sim 25,000$, which is in good agreement with previous laboratory experiments (Jonsson [9]).

Results of numerical experiments that varied the wave period, T, show that as the wave period increases, the boundary layer thickness increases and the flow becomes more turbulent, with the steady flow being the most turbulent. As the magnitude of the acceleration-deceleration phases decreases as the wave period increases, it is suggested that the duration of deceleration phase can be more significant than its

amplitude for some flow situations.

Different shapes of wave forcing have also been examined to understand the dynamics at flow reversal. It has been concluded that the magnitude of the deceleration, the duration of the deceleration phase, the Stokes layer thickness, and the recent history of the flow during preceding wave periods are important parameters in the origin and intensity of the turbulence.

Finally, mean currents of various amplitudes, perpendicular to the direction of wave oscillation, have been added to the model. The impact of a weak current ($V_\infty \sim 0.25U_m$) is to reduce the turbulence produced by the wave motion. The addition of a relatively strong current ($V_\infty > 0.5U_m$) results in increasingly turbulent flows as V_∞ increased.

The oscillatory boundary layer has been also modeled numerically with the one-dimensional eddy viscosity models of Grant and Madsen [5], $\nu_\tau(z) = \kappa z u^*_{max}$ and Trowbridge and Madsen [6], $\nu_\tau(z,t) = \kappa z u^*$. Spatially and temporally varying vertical eddy diffusivities, $\nu_\tau(z,t)$, were compared to the three-dimensional simulations and found to perform reasonably well for a broad range of conditions. These one-dimensional models seem, however, to overpredict the boundary layer thickness, δ_τ, and underpredict the shear near the wall, especially during periods of flow reversal or when flow acceleration inhibits turbulent production. The Grant and Madsen and Trowbridge and Madsen models are shown to give better approximations as the wave period, T, increases, as the flow becomes more turbulent, or when the free-stream forcing is not monochromatic.

Appendix A

Sixth-Order Compact Scheme

First Derivatives

Interior Domain Scheme

Following the work of Lele [46], except for the boundary values, each line of the tridiagonal matrix to solve for each derivative is of the form

$$12u_{x(i+1)} + 36u_{xi} + 12u_{x(i-1)} = \frac{1}{h}(u_{i+2} + 28u_{i+1} - 28u_{i-1} - u_{i-2}), \qquad (A1)$$

where h is the constant distance between the grid points and the right hand side is known explicitly. The truncation error for this scheme is found to be $\frac{4}{7!}h^6$.

Boundary Conditions

The boundary conditions are fifth-order accurate boundary scheme as boundary schemes can be one order less accurate than an interior domain scheme without degrading the overall accuracy of the interior scheme (Kreiss [60]). If the independent variable is periodic in the x-direction, then the system of relations written for each node can be solved together as a linear system of equations for the unknown derivative values. However for non-periodic cases, additional relations are required for the near boundary nodes. In the model, three kinds of boundary conditions are therefore employed, periodic, Dirichlet, and von Neumann boundary conditions.

Periodic Boundary Conditions In the model, the periodicity of the velocity in the x-direction is of the type $u_1 = u_n$, where n is the upper index of the set of nodes. Therefore, the relations for the derivatives at the nodes 1, 2, n-1 and n are

$$12u_{xn} + 36u_{x1} + 12u_{x2} = \frac{1}{h}(-u_{n-2} - 28u_{n-1} + 28u_2 + u_3) \qquad \text{(node 1)}, \qquad (A2)$$

$$12u_{x1} + 36u_{x2} + 12u_{x3} = \frac{1}{h}(-u_{n-1} - 28u_1 + 28u_3 + u_4) \qquad \text{(node 2)}, \qquad (A3)$$

$$12u_{x(n-2)} + 36u_{x(n-1)} + 12u_{xn} = \frac{1}{h}(-u_{n-3} - 28u_{n-2} + 28u_1 + u_2) \qquad \text{(node n-1)}, \quad (A4)$$

$$12u_{x(n-1)} + 36u_{x(n)} + 12u_{x1} = \frac{1}{h}(-u_{n-2} - 28u_{n-1} + 28u_2 + u_3) \qquad \text{(node n)}. \quad (A5)$$

The case of periodic boundary conditions is the simplest to implement numerically. The resulting tridiagonal matrix is not simply banded but includes two extra coefficients, one each in the upper-right and lower left corners of the left-hand-side matrix.

Dirichlet Boundary Conditions The Dirichlet boundary condition is used when the value of the velocity u is given for the boundary nodes. Numerical boundary conditions are implemented for the first or last two points of the grid

$$12u_{x1} + 48u_{x2} = \frac{1}{h}(-37u_1 + 8u_2 + 36u_3 - 8u_4 + u_5) \qquad \text{(node 1)}, \qquad (A6)$$

$$24u_{x2} + 36u_{x3} = \frac{1}{h}(-3u_1 - 44u_2 + 36u_3 + 12u_4 - u_5) \qquad \text{(node 2)}, \qquad (A7)$$

$$36u_{x(n-2)} + 24u_{x(n-1)} = \frac{1}{h}(3u_n + 44u_{n-1} - 36u_{n-2} - 12u_{n-3} + u_{n-4}) \qquad \text{(node n-1)}, \quad (A8)$$

$$24u_{x(n-1)} + 36u_{x(n-2)} = \frac{1}{h}(37u_n - 8u_{n-1} - 36u_{n-2} + 8u_{n-3} - u_{n-4}) \qquad \text{(node n)}. \quad (A9)$$

Von Neumann Boundary Conditions In the case of Von Neumann boundary conditions, the normal derivatives are specified on the boundary, that is u_{x1} and u_{xn} are known. Then the tridiagonal matrix is simplified and the relations for the nodes 2 and n-1 are given by

$$12u_{x1} + 36u_{x2} + 12u_{x3} = \frac{1}{h}(-u_{n-1} - 28u_1 + 28u_3 + u_4) \qquad \text{(node 2)}, \qquad (A10)$$

$$12u_{x(n-2)} + 36u_{x(n-1)} + 12u_{xn} = \frac{1}{h}(-u_{n-3} - 28u_{n-2} + 28u_1 + u_2) \qquad \text{(node n-1)}. \quad (A11)$$

The resulting tridiagonal matrices are computationally inexpensive and tridiagonal solvers are used to compute the derivatives.

Second Derivatives

Interior Domain Scheme

The second derivatives of the velocity are also calculated using Hermitian compact or Padé series techniques. The truncation error for this scheme is $-\frac{8}{11}\frac{23}{8!}h^6$. The resulting tridiagonal matrix to solve for each derivative is, except for the boundary values, of the form

$$8u_{xx(i+1)} + 44u_{xxi} + 8u_{xx(i-1)} = \frac{1}{h^2}(3u_{i+2} + 48u_{i+1} - 51u_i + 48u_{i-1} - 3u_{i-2}), \quad (A12)$$

where h is the distance between the grid points and the right hand side is known explicitly.

Boundary conditions

The boundary conditions are also fifth-order accurate.

Periodic boundary conditions The relations for the derivatives for periodic boundary conditions at the nodes 1 and n are

$$8u_{xxn}+44u_{xx1}+8u_{xx2} = \frac{1}{h^2}(3u_{n-2}+48u_{n-1}-102u_n+48u_2+3u_3) \qquad \text{(node 1)}, \quad (A13)$$

$$8u_{xx(n-1)} + 44u_{xn} + 8u_{xx1} = \frac{1}{h^2}(3u_{n-2} + 48u_{n-1} - 102u_n + 48u_2 + 3u_3) \qquad \text{(node n)}. \quad (A14)$$

Dirichlet Boundary Conditions Numerical boundary conditions are implemented for the first or last two points of the grid for Dirichlet boundary conditions are

$$12u_{xx1} + 120u_{xx2} = \frac{1}{h^2}(145u_1 - 304u_2 + 174u_3 - 16u_4 + u_5) \qquad \text{(node 1)}, \quad (A15)$$

$$12u_{x(n)} + 120u_{x(n-1)} = \frac{1}{h^2}(145u_n - 304u_{n-1} + 174u_{n-2} - 16u_{n-3} + u_{n-4}) \qquad \text{(node n)}. \tag{A16}$$

Von Neumann Boundary Conditions In the case of von Neumann boundary conditions, the relations for the nodes 2 and n-1 are given by

$$u_{xx1} + \frac{830}{257}u_{xx2} = -\frac{725}{257}\frac{1}{h}u_{x1} + \frac{1}{h^2}(-\frac{1225}{443}u_2 + \frac{533}{201}u_3 + \frac{44}{257}u_4 - \frac{46}{797}u_5) \quad \text{(node 2)}, \tag{A17}$$

$$u_{xxn} + \frac{830}{257}u_{xx(n-1)} = \frac{725}{257}\frac{1}{h}u_{xn} + \frac{1}{h^2}(-\frac{1225}{443}u_{n-1} + \frac{533}{201}u_{n-2} + \frac{44}{257}u_{n-3} - \frac{46}{797}u_{n-4}) \qquad \text{(node n-1)}. \tag{A18}$$

Comparison of Schemes

The new compact scheme has been tested for simple wave functions, 2π-periodic sums of sine functions of different frequencies, before being implemented in the model. Different schemes of computation of first and second derivatives, second-order finite difference scheme, fourth-order compact scheme and sixth-order compact scheme have been compared. The root mean squared (rms) difference between the different schemes and the analytic solution has been calculated at each grid point i, that is for the first derivative case to

$$rms(i) = \sqrt{\frac{(u_{xi}|_{computed} - u_{xi}|_{analytic})^2}{(u_{xi}|_{analytic})^2}} \tag{A19}$$

and then by summation over all the domain, the value of the rms difference of the first derivative computation for each scheme has been found to be equal to 0.2866 for the second-order scheme, $2.6166.10^{-2}$ for the fourth-order scheme and $3.7857.10^{-3}$ for the sixth-order one. The sixth-order compact scheme is therefore more accurate than the others of one order of magnitude at least. For finite-difference approximations of the first derivatives, the measure of accuracy or resolving efficiency of different

compact-scheme implementations has been defined (Lele [46]). This measure, called the modified wavenumber, represents the accuracy of the differentiation with respect to the exact one as a function of wavenumber $k\triangle x$, where $\triangle x$ is the grid space. The modified wavenumber of the sixth-order accuracy scheme for the first derivative is computed, following the work of Lele [46] as

$$\omega'(k\triangle x) = \frac{28\sin k\triangle x + \sin 2k\triangle x}{18 + 12\cos k\triangle x}. \qquad (A20)$$

Modified wavenumbers of the first derivative for second-order, fourth-order and sixth-order discretizations are plotted in comparison with the exact differentiation in Figure 1.

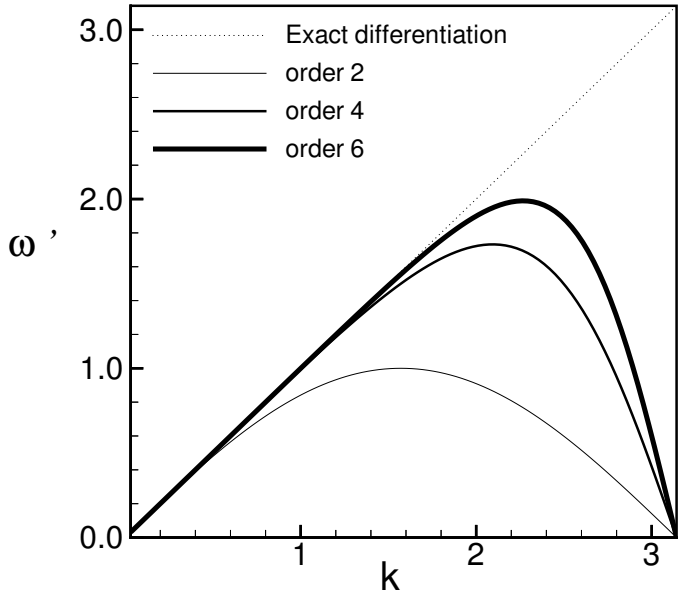

Figure 1: Modified wavenumbers of the first derivative for second-order, fourth-order and sixth-order discretizations in comparison with the exact differentiation.

This graph shows how close the different schemes come to the exact one. The function has a period of 2π, that is, the wavenumber π is equivalent to the $2\triangle x$ wave, $\pi/2$ is equivalent to the $4\triangle x$ wave ... The superiority of the sixth-order scheme

over the fourth or second-order schemes can again be noticed for a wider range of wavenumbers. For a wavenumber greater than $4\triangle x$ (or $\pi/2$), the sixth-order scheme is closer to the exact differentiation than the two other schemes.

The modified wavenumber of the sixth-order accuracy scheme for second derivatives is given by, following the work of Lele [46],

$$\omega''(k\triangle x) = \frac{51 - 48\cos k\triangle x - 3\cos 2k\triangle x}{22 + 8\cos k\triangle x}. \qquad (A21)$$

A plot of the modified wavenumbers of the second derivative for the second-order, fourth-order and sixth-order schemes is given in Figure 2.

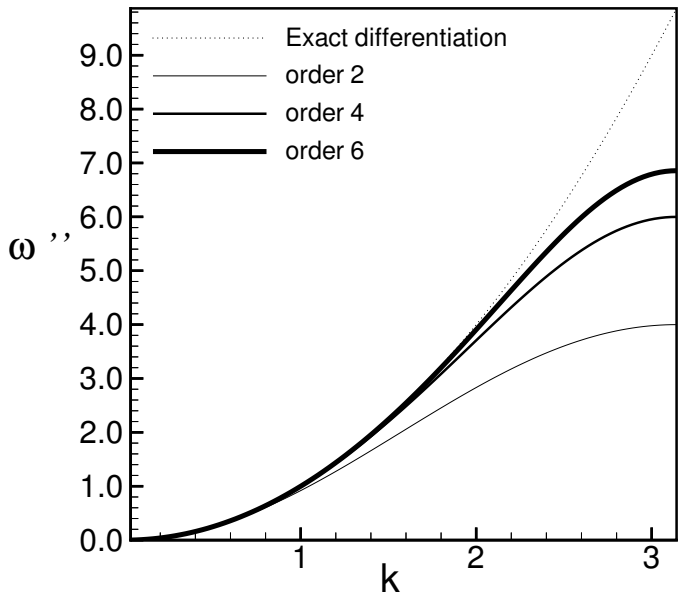

Figure 2: Modified wavenumbers of the second derivative for second-order, fourth-order and sixth-order discretizations in comparison with the exact differentiation

It can be checked, as for the first derivative, that the new compact scheme gives a better accuracy for a larger range of wavenumbers.

Appendix B

Transient Solution

By considering the following changes of variables, $U_s^* = \frac{U_s}{U_0}$, $U_t^* = \frac{U_t}{U_0}$, $T = \omega t$, and $Z = \sqrt{\frac{\omega}{\nu}} z$, the steady state solution of the Stokes's problem for a free stream velocity wave of the form $U_\infty(t) = U_0 \sin(\omega t)$ becomes

$$U_s^*(Z,T) = \sin T - \sin(T - \frac{Z}{\sqrt{2}}) \exp(-\frac{Z}{\sqrt{2}}), \tag{B1}$$

and the transient solution corresponds to the equation

$$\frac{\partial U_t^*}{\partial T} = \frac{\partial^2 U_t^*}{\partial Z^2}. \tag{B2}$$

As the fluid is initially quiescent,

$$U_t^*(Z,0) = -U_s^*(Z,0) = [-\sin T + \sin(T - \frac{Z}{\sqrt{2}}) \exp(-\frac{Z}{\sqrt{2}})]|_{T=0}$$

$$= \sin(-\frac{Z}{\sqrt{2}}) \exp(-\frac{Z}{\sqrt{2}}). \tag{B3}$$

A solution for an oscillatory flow over a flat plate is developed following the approach of Panton [51] for flow over an oscillating plate. This problem can be assimilated to the unsteady heat conduction in a semi finite slab, with an initial temperature $f(x)$ and the surface temperature initially at zero. The heat conduction equation is of the form

$$\frac{\partial v}{\partial t} - k\frac{\partial^2 v}{\partial x^2} = 0, \tag{B4}$$

where $v(x)$ is given by Carslaw and Jaeger [61],

$$v(x) = \frac{1}{2\sqrt{\pi k t}} \int_0^\infty f(x') \left[\exp(-\frac{(x-x')^2}{4kt}) - \exp(-\frac{(x+x')^2}{4kt})\right] dx', \tag{B5}$$

in which $f(x')$ is the initial temperature profile. In the boundary layer problem, $\frac{\partial U_t^*}{\partial T} = \frac{\partial^2 U_t^*}{\partial Z^2}$, the transient solution becomes

$$U_t^*(Z,T) = \frac{1}{2\sqrt{\pi T}} \int_0^\infty f(\xi) \left[\exp(-\frac{(Z-\xi)^2}{4T}) - \exp(-\frac{(Z+\xi)^2}{4T}) \right] d\xi, \qquad (B6)$$

where $f(\xi)$ is the initial velocity that is

$$f(\xi) = \Im(\exp(-\frac{1+i}{\sqrt{2}\xi})), \qquad (B7)$$

where $\Im$ represent the imaginary part. Then,

$$U_t^*(Z,T) = \frac{1}{2\sqrt{\pi T}} \int_0^\infty \Im \left[\exp(-\frac{1+i}{\sqrt{2}}\xi - \frac{(Z-\xi)^2}{4T}) - \exp(-\frac{1+i}{\sqrt{2}}\xi - \frac{(Z+\xi)^2}{4T}) \right] d\xi, \qquad (B8)$$

or

$$U_t^*(Z,T) = \frac{1}{2\sqrt{\pi T}} \Im \int_0^\infty$$
$$\left[\exp(-(\frac{1}{4T}\xi^2 + (\frac{Z}{2T} - \frac{1+i}{\sqrt{2}})\xi + \frac{Z^2}{4T})) - \exp(-(\frac{1}{4T}\xi^2 + (\frac{Z}{2T} + \frac{1+i}{\sqrt{2}})\xi + \frac{Z^2}{4T})) \right] d\xi, \qquad (B9)$$

According to Abramowitz and Stegun [62],

$$\int_0^\infty \exp(-(\alpha t^2 + 2\beta t + \gamma)) dt = \frac{1}{2}\sqrt{\frac{\pi}{\alpha}} \exp(\frac{\beta^2 - \alpha\gamma}{\alpha}) erfc(\frac{\beta}{\sqrt{\alpha}}), \qquad (B10)$$

where, in the boundary layer problem,

$$\alpha = \frac{1}{4T},$$
$$\beta = -\frac{1}{2}(\pm\frac{Z}{2T} + \frac{1+i}{\sqrt{2}}),$$
$$\gamma = \frac{Z^2}{4T}, \qquad (B11)$$

and where $erfc$ is the complementary error function given by

$$erfc(x) = 1 - erf(x) = 1 - \frac{2}{\sqrt{\pi}} \int_0^x exp(-t^2) dt = \frac{2}{\sqrt{\pi}} \int_x^\infty exp(-t^2) dt, \qquad (B12)$$

erf being the error function. Then

$$U_t^*(Z,T) = \Im\Big(\frac{1}{2}\exp(-\frac{1+i}{\sqrt{2}}+iT)erfc(\sqrt{\frac{T}{2}}(1+i-\frac{Z}{T\sqrt{2}}))$$

$$\frac{1}{2}\exp(\frac{1+i}{\sqrt{2}}+iT)erfc(\sqrt{\frac{T}{2}}(1+i+\frac{Z}{T\sqrt{2}}))\Big). \qquad (B13)$$

It can be checked that the real part of this expression is the transient solution to the problem of a free stream velocity oscillating as $-\cos T$ instead of $\sin T$.

To find the imaginary part of this expression, since no exact expression of the decomposition of the error function in real and imaginary parts exits, an approximation of the error function given by Abramowitz and Stegun [62] is used

$$erfc(x+iy) = 1-erf(x+iy) = 1-(erfx+\frac{\exp(-x^2)}{2\pi x}[(1-cos2xy)+isin2xy]+...), \qquad (B14)$$

and an approximation of the transient laminar solution is determined

$$U_t^*(Z,T) = \frac{1}{2}\exp(-\frac{Z}{\sqrt{2}})sin(-\frac{Z}{\sqrt{2}}+T)[1-erf(a)-\frac{\exp(-a^2)}{2\pi a}(1-\cos 2ab)]-$$

$$\frac{1}{2}\exp(-\frac{Z}{\sqrt{2}})\cos(-\frac{Z}{\sqrt{2}}+T)[\frac{\exp(-a^2)}{2\pi a}\sin 2ab]-$$

$$\frac{1}{2}\exp(\frac{Z}{\sqrt{2}})sin(\frac{Z}{\sqrt{2}}+T)[1-erf(c)-\frac{\exp(-c^2)}{2\pi c}(1-\cos 2cb)]-$$

$$\frac{1}{2}\exp(\frac{Z}{\sqrt{2}})\cos(-\frac{Z}{\sqrt{2}}-T)[\frac{\exp(-c^2)}{2\pi c}\sin 2cb], \qquad (B15)$$

where $a = \sqrt{\frac{T}{2}}(1-\frac{z\sqrt{\frac{\omega}{\nu}}Z}{T\sqrt{2}})$, $b = \sqrt{\frac{T}{2}}$, $c = \sqrt{\frac{T}{2}}(1+\frac{Z}{T\sqrt{2}})$, $U_t = \frac{u_t}{U_0}$, $T = \omega t$, and $Z = z\sqrt{\frac{\omega}{\nu}}$.

In dimensional form, the transient velocity is

$$U_t(Z,T) = \frac{1}{2}U_m\exp(-\sqrt{\frac{\omega}{2\nu}}z)sin(-\sqrt{\frac{\omega}{2\nu}}z+\omega t)[1-erf(a)-\frac{\exp(-a^2)}{2\pi a}$$

$$(1-\cos 2ab)]-$$

$$\frac{1}{2}U_m \exp(-\sqrt{\frac{\omega}{2\nu}}z)\cos(-\sqrt{\frac{\omega}{2\nu}}z+\omega t)[\frac{\exp(-a^2)}{2\pi a}\sin 2ab]-$$
$$\frac{1}{2}U_m \exp(\sqrt{\frac{\omega}{2\nu}}z)sin(\sqrt{\frac{\omega}{2\nu}}z+\omega t)[1-erf(c)-\frac{\exp(-c^2)}{2\pi c}$$
$$(1-\cos 2cb)]-$$
$$\frac{1}{2}U_m \exp(\sqrt{\frac{\omega}{2\nu}}z)\cos(\sqrt{\frac{\omega}{2\nu}}z+\omega t)[\frac{\exp(-c^2)}{2\pi c}\sin 2cb], \qquad (B16)$$

where $a=\sqrt{\frac{\omega t}{2}}(1-\frac{\sqrt{\frac{\omega}{\nu}}z}{\omega t\sqrt{2}})$, $b=\sqrt{\frac{\omega t}{2}}$, and $c=\sqrt{\frac{\omega t}{2}}(1+\frac{\sqrt{\frac{\omega}{\nu}}z}{\omega t\sqrt{2}})$.

More terms in the approximation of the error functions have been used, however, the velocity obtained did not not vary measurably.

It can be checked that the no-slip condition is respected, i.e., $U_t(0,t)=0$, the fluid is initially quiescent, i.e., $U_t(z,0)=U_m\sin(-\frac{z}{\delta_s})\exp(-\frac{z}{\delta_s})$, and the transient velocity vanishes as t becomes large, i.e., $U_t(z,\infty)=0$.

Appendix C

Implementation of the One-Dimensional Model

The domain of the boundary layer is covered by a grid of successive points spaced out by a step size $\triangle z$ in the normal direction as shown in Figure 3.

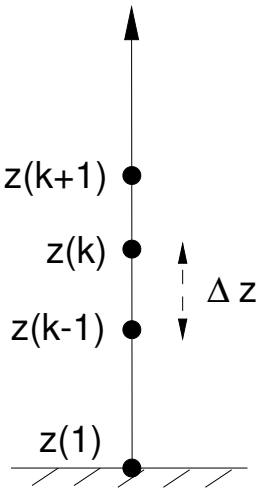

Figure 3: Step size finite-difference grid for the calculation of turbulent boundary layer.

By using second order spatial differences, the derivative of the velocity at the point k can be written as

$$\frac{\partial u}{\partial z}\Big|_{(k,n)} = \frac{u_{k+1,n} - u_{k-1,n}}{2\triangle z} + \vartheta(\triangle z^2). \qquad (C1)$$

The governing equation, considering $\nu_\tau = \nu_\tau(k,n)$, becomes

$$\frac{\partial u(k,n)}{\partial t} - \frac{\partial U_\infty(n)}{\partial t} = \frac{\partial}{\partial z}\left(\nu_\tau(k,n)\frac{u(k+1,n)}{2\triangle z}\right) - \frac{\partial}{\partial z}\left(\nu_\tau(k,n)\frac{u(k-1,n)}{2\triangle z}\right), \quad (C2)$$

and is further discretized as

$$\frac{\partial u(k,n)}{\partial t} - \frac{\partial U_\infty(n)}{\partial t} = \nu_\tau(k+1,n)\frac{u(k+2,n)}{(2\triangle z)^2} - \nu_\tau(k-1,n)\frac{u(k,n)}{(2\triangle z)^2} -$$

$$\nu_\tau(k+1,n)\frac{u(k,n)}{(2\triangle z)^2}+\nu_\tau(k-1,n)\frac{u(k-2,n)}{(2\triangle z)^2}.$$

If the viscosity is considered to be constant, that is independent of time and of the z-coordinate, (C3) becomes

$$\frac{\partial u(k,n)}{\partial t}-\frac{\partial U_\infty(n)}{\partial t}=\nu\frac{u(k+2,n)-2u(k,n)+u(k-2,n)}{(2\triangle z)^2}. \qquad (C4)$$

As this scheme is not "compact" enough because it doesn't involve a relation between grid points on a smaller stencil than the standard finite difference formula, the same steps are done using a space interval of $\triangle z/2$ instead of $\triangle z$ as shown in Figure 3. A new derivative of the velocity at the grid point k is therefore obtained

$$\frac{\partial u}{\partial z}\Big|_{(k,n)}=\frac{u(k+1/2,n)-u(k-1/2,n)}{\triangle z}+\vartheta(\triangle z^2). \qquad (C5)$$

By introducing an new variable

$$H(k)=\nu_\tau(k,n)\frac{\partial u(k,n)}{\partial z}, \qquad (C6)$$

then

$$\frac{\partial H(k)}{\partial z}\Big|_k=\frac{H_{k+1/2}-H_{k-1/2}}{\triangle z}. \qquad (C7)$$

By approximating the value of the eddy viscosity at one point by the average value of the viscosity calculated with the values of the viscosity spaced out by $\triangle z/2$, with $\triangle z$ small, such that

$$\nu_\tau(k+1/2,n)=\frac{\nu_\tau(k,n)+\nu_\tau(k+1,n)}{2}, \qquad (C8)$$

the new variable becomes at point $k+1/2$ and $k-1/2$, respectively

$$H(k+1/2)=\frac{\nu_\tau(k,n)+\nu_\tau(k+1,n)}{2}\left[\frac{u(k+1,n)-u(k,n)}{\triangle z}\right], \qquad (C9)$$

$$H(k-1/2)=\frac{\nu_\tau(k-1,n)+\nu_\tau(k,n)}{2}\left[\frac{u(k,n)-u(k-1,n)}{\triangle z}\right]. \qquad (C10)$$

Thus, after manipulation, (C7) becomes

$$\frac{\partial H(k)}{\partial z}\Big|_k = \frac{1}{2\triangle z^2}[(\nu_\tau(k,n)+\nu_\tau(k+1,n))u(k+1,n) - (\nu_\tau(k-1,n)+2\nu_\tau(k,n)+$$

$$\nu_\tau(k+1,n))u(k,n)) + (\nu_\tau(k-1,n)+\nu_\tau(k,n))u(k-1,n)], \qquad (C11)$$

and if the viscosity is constant,

$$\frac{\partial u(k,n)}{\partial t} - \frac{\partial U_\infty(n)}{\partial t} = \nu\frac{u(k+1,n)-2u(k,n)+u(k-1,n)}{\triangle z^2}. \qquad (C12)$$

By differentiating the velocity with respect to time and choosing $\triangle t$ as small as possible, the time derivative velocity becomes

$$\frac{\partial u}{\partial t}\Big|_k = \frac{u(k,n+1)-u(k,n)}{\triangle t} \qquad \triangle t \leq \frac{2\triangle z^2}{\nu_{\tau_{max}}}C, \qquad (C13)$$

where $C \leq 1$ for stability. The value $C = 1/2$ has been chosen, for a more accurate approximation.

Finally, the expression of the velocity at the position k and at the time $n+1$ in function of the velocity at the time n is

$$u(k,n+1) = u(k,n) + \triangle t\frac{\partial U_\infty(n)}{\partial t} + \frac{\triangle t}{2\triangle z^2}\Big[(\nu_\tau(k,n)+\nu_\tau(k+1,n))u(k+1,n) -$$

$$(\nu_\tau(k-1,n)+2\nu_\tau(k,n)+\nu_\tau(k+1,n))u(k,n)+$$

$$(\nu_\tau(k-1,n)+\nu_\tau(k))u(k-1,n)\Big]. \qquad (C14)$$

In the explicit calculations, the velocity is known at $t = n$ and sought at $t = n+1$. The computing time and accuracy of the method depend on the step size used in the calculation, but generally for the parameters chosen, a few wave periods can be calculated on the order of 10 minutes of CPU time on a DEC-Alpha 600au workstation.

Bibliography

[1] Prandtl, L., *On the Motion of a Fluid with Very Small Viscosity*, Third International Congress of Mathematicians, Heidelberg, 1904.

[2] Reynolds, O., *Philos. Trans. R. Soc.*, London Ser., A 186, 123-164, 1895.

[3] Mei, C. C., *The Applied Dynamics of Ocean Surface Waves*, 70 pp., World Scientific, Publishing Co., Singapore, 1989.

[4] Slinn, D. N., Riley, J. J., A Model for the Simulation of Turbulent Boundary Layers in an Incompressible Stratified Flow, *Journal of Computational Physics*, 144, 550-602, 1998.

[5] Grant, W. D., Madsen, O. S., The Continental-Shelf Bottom Boundary Layer, *Annual Review of Fluid Mechanics*, 18, 265-305, 1986.

[6] Trowbridge, J., Madsen, O.S., Turbulent Wave Boundary Layers 1. Model Formulation and First-Order Solution, *Journal of Geophysical Research*, 89, 7989-7997, 1984.

[7] Stokes, G. G., *Trans. Camb. Phil. Soc.*, 50, 287, 1845.

[8] Batchelor, G. K., *An Introduction to Fluid Dynamics*, 615 pp., Cambridge University Press, Cambridge, 1967.

[9] Jonsson, I. G., A New Approach to Oscillatory Rough Turbulent Boundary Layer, *Ocean Engineering*, Vol. 7, 109-152, 1980.

[10] Iwagaki, Y., Kakinuma, T., On the Bottom Friction Factor of the Akita Coast, *Coastal Engineering in Japan*, 6, 83-91, 1963.

[11] Jensen, B., L., Sumer, B., M., Fredsoe, J., Turbulent Oscillatory Boundary Layers at High Reynolds Numbers, *Journal of Fluid Mechanics*, 206, 265-297, 1989.

[12] Hino, M., Kashiwayanagi, M., Nakayama, A. Hara, T., Experiments on the Turbulence Statistics and the Structure of a Reciprocating Oscillatory Flow, *Journal of Fluid Mechanics*, 206, 265-297, 1989.

[13] Spalart, P. R., Baldwin, B. S., Direct Simulation of a Turbulent Oscillating Boundary Layer, *A Technical Memorandum*, 89460, 1987.

[14] Kamphuis, J. W., Friction Factor under Oscillatory Waves, *Journal of Waterways Port, Coastal and Ocean Engineering Division*, ASCE, 101, 135-144, 1975.

[15] Kajiura, K., A Model of the Bottom Boundary layer in Water Waves, *Bulletin of the Earthquake Research Institute*, 46, Tokyo, Japan, 75-123, 1968.

[16] Fredsoe, J., Boundary Layer in Wave Current Motion, *Journal of Hydraulic Engineering*, 110, 1103-1120, 1984.

[17] Sleath, J. F. A., Turbulent Oscillatory Flow over Rough Beds, *Journal of Fluid Mechanics*, 182, 369-409, 1987.

[18] Lundgren, H., Turbulent Currents in the Presence of Waves, *Proceedings of the 13th Conference on Coastal Engineering*, Vancouver, Canada, 1, Paper 1.12, 623-634, 1972.

[19] Brevik, I., Oscillatory Rough Turbulent Boundary Layer, *Journal of the Waterway, Port, Coastal and Ocean Division, Proceedings of American Society of Civil Engineers*, 107, 175-188, 1981.

[20] Jonsson, I. G., Measurements in the Turbulent Wave Boundary Layer, *Proceedings of the 10^{th} Congress IAHR*, London, England, 1, Paper 1.12, 85-92, 1963.

[21] Jonsson, I. G., Carlsen, N., A., Experimental and Theoretical Investigations in an Oscillatory Turbulent Boundary Layer, *Journal of Hydraulic Research*, 14, No 1, Delft, Holland, 45-60, 1976.

[22] Long, C. E., *A Simple Model for Time-Dependant Stably Stratified Turbulent Boundary Layers*, Spec. Rep. No. 95, Dep. Oceanogr., Univ. Wash., Seattle, 1981.

[23] Sanford, L. P., *The Interaction of High Frequency Internal Waves and Bottom Boundary Layers on the Continental Shelf*, PhD thesis, Woods Hole Oceanographic Institute, M.I.T., Cambridge,1984.

[24] Lavelle, J. W., Mofjeld, H. O., Effects of Time-Varying Viscosity on Oscillatory Channel Flow, *Journal of Geophysical Research*, 88, No. C12, 7607-7616, 1983.

[25] Trowbridge, J., *Wave-Induced Turbulent Flow near a Rough Bed: Implications of a Time-Varying Eddy Viscosity*, Sc.D. Thesis, Woods Hole Oceanographic Institute, M.I.T., Cambridge, 1983.

[26] Grant, W. D., Madsen, O. S., Combined Wave and Current Interaction with a Rough Bottom, *Journal of Geophysical Research*, 84, 1797-1808, 1979.

[27] Smith, J. D., Modelling of Sediment Transport on Continental Shelves, *The Sea*, 6, Interscience, New York, 539-577, 1977.

[28] Bakker, W. T., Doorn, T., Near-Bottom Velocities in Wave with a Current, *Proc. Coastal Enginnering Conference*, 1394-1413, 1978.

[29] Myrhaug, D., Slaattelid, O. H., Combined Wave and Current Boundary Layer Model for Fixed Rough Seabeds, *Ocean Engineering*, 16, No. 2, 119-142, 1989.

[30] Christoffersen, J. B., Jonsson, I. G., Bed Friction and Dissipation in a Combined Current and Wave Motion, *Ocean Engineering*, 12, No. 5, 387-423, 1985.

[31] Kemp, P. H., Simons, R. R., The Interaction between Waves and a Turbulent Current: Waves Propagating with the Current, *Journal of Fluid Mechanics*, 116, 227-250, 1982.

[32] Van Doorn, T., Experimental Investigation of Near Bottom Velocities in Water Waves With and Without a Current, *TOW-Report*, 1981.

[33] Sleath, J. F. A., Bed Friction and Velocity Distributions in Combined Steady and Oscillatory Flow, *Proceedings of the 22nd International Conference Coastal Engineering*, Delft, 450-463, 1990.

[34] Vittori, G., Verzicco, R., Direct Simulation of Transition in Stokes Boundary Layers, *Journal of Fluid Mechanics*, 371, 207-232, 1998.

[35] Blondeaux, P., Sand Ripples under Sea Waves, Part 1: Ripple Formation, *Journal of Fluid Mechanics*, 264, 107-135, 1990.

[36] Akhavan, R., Kamm, R. D., Shapiro, A. H., An Investigation of Transition to Turbulence in Bounded Oscillatory Stokes Flows, Part 2: Numerical Simulations, *Journal of Fluid Mechanics*, 255, 423-444, 1991.

[37] Foster, D. L., Beach, R. A., Holman, R. A., Field Observations of the Wave Bottom Boundary Layer, *Journal of Geophysical Research*, In Press, 2000.

[38] Foster, D. L., Guenther, R., Holman, R. A., An Analytical Solution to the Wave Bottom Boundary Layer Equation, *Journal of Fluid Mechanics*, 255, 423-444, 1991.

[39] Sarpkaya, T., Coherent Structures in Oscillatory Boundary Layers, *Journal of Fluid Mechanics*, 253, 105-140, 1993.

[40] Gad-El-Hak, M., Davis, S. H., McMurray, J. T., Orszag, S. A., On the Stability of the Decelerating Laminar Boundary Layer, *Journal of Fluid Mechanics*, 138, 297-323, 1984.

[41] Piomelli, U., Balaras, E., Pascarelli, A., Turbulent Structures in Accelerating Boundary Layers, *Journal of Turbulence*, 2000.

[42] Phillips, N. A., An Example of Non-linear Computational Instabilities, *The Atmosphere and Sea in Motion, Rossby Memorial Volume*, 501-504, New York, Rockfeller

[43] Durran, D. R., Yang, M. Z., Slinn, D. N., Brown, R., Towards More Accurate Wave-Permeable Boundary conditions, *Monthly Weather Review*, 121, 604-620, 1993.

[44] Hirsh, R. S., Higher Order Accurate Difference Solutions of Fluid Mechanics Problems by a Compact Differencing Technique, *Journal of Computational Physics*, 90, 19, 1975.

[45] Adam, Y., Highly Accurate Compact Implicit Methods and Boundary Conditions, *Journal of Computational Physics*, 24, 10-22, 1977.

[46] Lele, S. K., Compact Finite Difference Schemes with Spectral-Like Resolution, *Journal of Computational Physics*, 103, 16, 1992.

[47] Vichnevestsky, R., *Mathematical Computational Simulation*, 21, 170, 1979.

[48] Tennekes, H., Lumley, J. L., *A First Course in Turbulence*, MIT Press, Cambridge, Mass, 1972.

[49] Panton, R. L., *Incompressible flow*, 2nd edition, Wiley-Interscience, 1996.

[50] Richardson, E. G., Tyler, E., *Proc. Phys. Soc.*, London, 42, 1, 1929.

[51] Panton, R. L., The Transient for Stokes's Oscillating Plate: a Solution in Terms of Tabulated Functions, *Journal of Fluid Mechanics*, 31, part 4, 819-825, 1968.

[52] Dean, R. G., Dalrymple, R. A., Water Wave Mechanics for Engineers and Scientists, *Advanced Series on Ocean Engineering*, Volume 2, World Scientific, 1991.

[53] Canuto C., Hussaini, M. Y., Quarteroni, A., Zang, T. A., *Spectral Methods in Fluid Dynamics*, Springer Verlag, New York, 557 pp., 1988.

[54] Moin, P., Mahesh, K., Direct Numerical Simulation: A Tool in Turbulence Research, *Annual Review of Fluid Mechanics*, 30, 539-578, 1998.

[55] Spalart, P., Direct Numerical Simulation of a Turbulent Boundary Layer up to $R_\theta = 1410$, *Journal of Fluid Mechanics*, 187, 61-98, 1988.

[56] Fredsoe, J., Deiggard, R., *Mechanics of Coastal Sediment Transport*, Advanced Series on Ocean Engineering, Volume 3, 1992.

[57] Hinze, J. O., *Turbulence*, McGraw Hill, New York, 1975.

[58] Schlichting, H., *Boundary Layer Theory*, 4th ed., 647

[59] Julien, P. Y., *Erosion and Sedimentation*, Cambridge University Press, 1994.

[60] Kreiss, H. O., *O. Math. Comput.*, 26, 605-624, 1972.

[61] Carslaw, H. S., Jaeger, J. C., *Conduction of Heat in Solids*, Oxford University Press, 1959.

[62] Abramowitz, B. M., Stegun, I. A., *Handbook of Mathematical Functions with Formulas, Graphs, and Mathematical Tables*, Washington, U.S. Gov. Printing Office, 1964.